DETERMINATION OF HYDROGEN-CONTAINING GASES IN AIR WITH SNO2-BASED SENSORS

Dmitry Shaposhnik

Dmitry Shaposhnik

Determination of hydrogen-containing gases in air with SnO_2-based sensors

Doctoral thesis

Supervised by Dr. Xavier Vilanova

Department of Electronic, Electrical & Automatic Control Engineering

UNIVERSITAT ROVIRA I VIRGILI

Tarragona

2015

UNIVERSITAT ROVIRA I VIRGILI
DETERMINATION OF HYDROGEN-CONTAINING GASES IN AIR WITH SNO2-BASED SENSORS
Dmitry Shaposhnik

UNIVERSITAT ROVIRA I VIRGILI
ESCOLA TÈCNICA SUPERIOR D'ENGINYERIA
DEPARTAMENT D'ENGINYERIA ELECTRONICA, ELÈCTRICA I AUTOMÀTICA

Avinguda dels Països Catalans, 26
Campus sescelades
43007 Tarragona
Tel. (977) 55 96 10
Fax (977) 55 96 05
e-mail: secelec@etse.urv.es
http://www.etse.urv.es/DEEEA/

I STATE that the present study, entitled "Determination of hydrogen-containing gases in air with SnO2-based sensors", presented by Dmitry Shaposhnik for the award of the degree of Doctor, has been carried out under my supervision at the Department of Electrical, Electronic and Automatic Control Engineering of this university.

Tarragona, June 26th 2015

Doctoral Thesis Supervisor/s

Xavier Vilanova

UNIVERSITAT ROVIRA I VIRGILI
DETERMINATION OF HYDROGEN-CONTAINING GASES IN AIR WITH SNO2-BASED SENSORS
Dmitry Shaposhnik

Acknowledgments

This thesis would not have been possible without the scholarship from the University Rovira i Virgili as well as collaboration and help of a number of people.

I am deeply grateful to my advisor Dr. Xavier Vilanova for his permanent responsiveness, keen and profound guidance, and constant help. This work couldn't be finished without his support. I am heartily obliged to him.

I express my most sincere thanks to Dr. Roman Pavelko for his key role in the present study, as well as for his suggestions and support with research and everyday life.

I am sincerely grateful to a member of the jury, Dr. Alexey Vasiliev, for his continuous valuable help during my study.

I am much obliged to Prof. Xavier Correig Blanchar for his fascinating courses, everlasting support and beatiful team-building events.

I thank head of MINOS group, Dr. Eduard Llobet Valero, for his support of my work.

I'd like to thank the staff of URV microscopy unit: Lukas Vojkuvka, Rita Marimon Picó, Mercè Moncusí Mercadé for their important and most professional aid to my work, splendid friendly atmosphere and skills they passed to me.

A special thank is for Dr. Francesc Gispert i Guirado for his persistent work and great input in the final result.

I am much obliged to Dr. Raúl Calavia Boldú for his utmost unforgettable positive and great professional support.

I sincerely thank Serena Pujol Paulí for her hard work as lab manager. Her assistance was very important for our studies.

I am grateful to Dr. Toni Stoicheva, Dr. Houda Lahlou, and Dr. Raduoane Leghrib to be splendid partners for all my study.

I also sincerely thank my supervisor in Siemens AG, Mr. Pavel Volodchenko, for his loyalty which made possible my defence.

I thank my friends from ETSEQ for the great time we spent in Tarragona.

Most of all I thank my family and congratulate them on finish of this manuscript.

Index

Introduction

Metal oxides SnO_2, ZnO, In_2O_3, WO_3, TiO_2 are wide band gap n-type semiconductors and are separated to a “transparent semiconductors” group due to an unique set of properties: electroconductivity, transparency in a wide spectra range and surface reactivity. Materials based on these oxides are applied in transparent electrodes, electrochromic coatings, optoelectronic and photovoltaic transducers, transistors, electrodes for aluminium production, and catalysts. One of the most relevant areas of metal oxides application include gas sensors – devises which transduce information about gas phase composition to an electrical signal. It is established that all semiconductors demonstrate sensing effect, but the group of semiconducting oxides SnO_2, ZnO, In_2O_3, WO_3, TiO_2 is characterized with a highest gas sensitivity. Physical principles of semiconductor sensors action are based on high sensitivity of semiconductors surface to the composition of ambient atmosphere. Chemisorption of gas phase molecules and chemical reactions on the surface lead to significant changes of band structure in narrow near-surface layer, energy barriers formation at the phase interface, what affects work function and surface conductivity values. Materials microstructure, pores and crystallites sizes influences sensing parameters; highest values of sensing signal demonstrate nanocrystalline materials with high relative surface, and, consequently, high adsorption activity.

Improvement of interaction specificity with gas phase is one of main research directions in the field of gas sensing materials. As known, metal oxides are effective catalysts of oxidation reactions due to the activity of surface states activity in band gap. The problem of control of metal oxide catalysts activity is of great interest.

Metrological characteristics of semiconductor gas sensors are determined by physicochemical properties of their sensing elements, which in turn depend on crystal structure, composition and electrophysical properties of semiconducting oxides. In order to control gas sensing properties of it is necessary to find a

relationship between material electrophysical parameters and its element composition, crystal structure and current transfer mechanisms.

Main material of modern gas sensing is tin dioxide, which is characterized by stable physicochemical properties in wide temperature range and relatively low temperatures of maximum gas sensitivity.

A new direction of gas sensing materials research is currently being formed: synthesis and investigation of catalytically active oxides mixtures in comparable concentrations in order to create new materials with high reactive and adsorptive activity. In most cases, such mixtures are prepared by sol-gel method. Systematic investigation of such mixtures is thus far.

The topic of the present work is the development of new approaches to improvement of sensing characteristics of gas sensors detecting gases containing hydrogen atoms in their molecules: H_2, H_2S, NH_3, aldehydes and ketones, – with the use of nanostructured metal oxide materials with improved surface, electric and catalytic properties.

Chapter 1 describes existing approaches to fabrication of semiconductor metal oxide gas sensors. It's possible to single out several main types of the sensors construction: thick-layer (3D), thin-layer (2D), and single-nanowire (1D) sensors. Physical and chemical properties of the metal oxides used in the work are described; main directions of the research work undertaken nowadays in order to better understand mechanisms of gas sensing and possibilities to improve sensing characteristics are observed.

Chapter 2 reports synthesis methods, the methods and the equipment used for characterization of synthesized materials and sensors fabricated with the use of these materials.

Chapter 3 describes the results of materials synthesis and characterization. Advantages of a new method of SnO_2 synthesis proposed in this work and the properties of the material obtained are discussed.

Chapters 4 to 7 present the results of hydrogen-containing gases detection using several approaches: doping of one metal oxide (SnO_2) with another (TiO_2) in different ways (mixing or co-precipitating); use of one-dimensional sensing element to determine H_2S; application of reactor which converts analite to a compound convenient for its detection; analysis of n-dimensional experimental data array with principal components method.

1. State of the art

1.1. Bulk properties of semiconducting metal oxides

1.1.1. Properties of tin dioxide

Nanocrystalline tin dioxide has found the widest practical application as a material for gas sensing layers. The uniqueness of tin dioxide is related with a number of its fundamental physical and chemical properties. First, it is a wide-gap n-type semiconductor, and its electroconductivity is very sensitive to the condition of the surface in the range of temperatures (100-500 ^{o}C), where redox reactions can take place. Second, SnO_2 surface have high adsorption properties and reactivity. The reasons of high reactivity of SnO_2 are the presence of free electrons in the conduction band and the existence of surface and bulk oxygen vacancies and active chemisorbed oxygen. Besides that, SnO_2 may be obtained in highly dispersed and stable state [1]. Tin dioxide is melted without decomposition at rather high temperature of 1630 ^{o}C.Therefore, SnO_2 based sensors have high enough thermal stability for working at temperatures in the range of 200-500 ^{o}C.

Tin dioxide has tetragonal cassiterite structure with space symmetry group P4/mnm. The basis of its structure constitute octahedrons SnO_6, coupled with their opposite edges and forming columns laying parallel to C axis and joined together with their vertexes. SnO_6 octahedrons have D2h symmetry; distance between atoms is 2.08 Å. Crystal structure of cassiterite is analogous to rutile structure. Tin dioxide is characterized by oxygen deficiency, its composition may be presented as $SnO_{2-\delta}$, where $10^{-5}<\delta< 10^{-3}$ is deviation from stoichiometry. Double ionized oxygen vacancies are the main native defects that determine electrical properties of the material: electron type of conductivity and free charge carriers concentration; $n= 2[V_O^{2+}]$. The most probablemechanism of native defects formation in SnO_2 is

Schottky reaction, according which oxygen atoms moveto the surface, completing crystal lattice; obtained vacancies diffuse into the bulk:

$$O_O = O_{surf} + V_O, \quad (1.1)$$

$$V_O = V_O^{2+} + 2e. \quad (1.2)$$

Tin dioxide is a semiconductor with band gap E_g = 3.6 eV (25 °C). Energy level of doubly ionized oxygen vacancies lays 130 meV lower than the edge of the conduction band. Concentration of oxygen vacancies may be reduced by annealing of material in oxygen atmosphere; conductivity type of tin dioxide is not changed after that.

Sensor signal nature in semiconductors is related, first of all, with the process of molecules chemisorption, which proceeds with participation of free electrons in the near-surface layer of the material. The diagram of changes in energy-band structure of SnO_2 as a result of adsorption is presented in Figure 1.1.Left part of the figure (*a*) represents the band diagram in the bulk of semiconductor. Chemisorption of oxygen molecules from the air is performedwith participation of electrons from the conduction band and can be represented with the following equation:

$$\tfrac{1}{2}(O_2)_{gas} + 2e = (O^{2-})_{surf} \quad (1.3)$$

Space charge, formed as a result of this interaction, leads to distortion of conduction band and valence band in near-surface layer (figure 1.1 c).

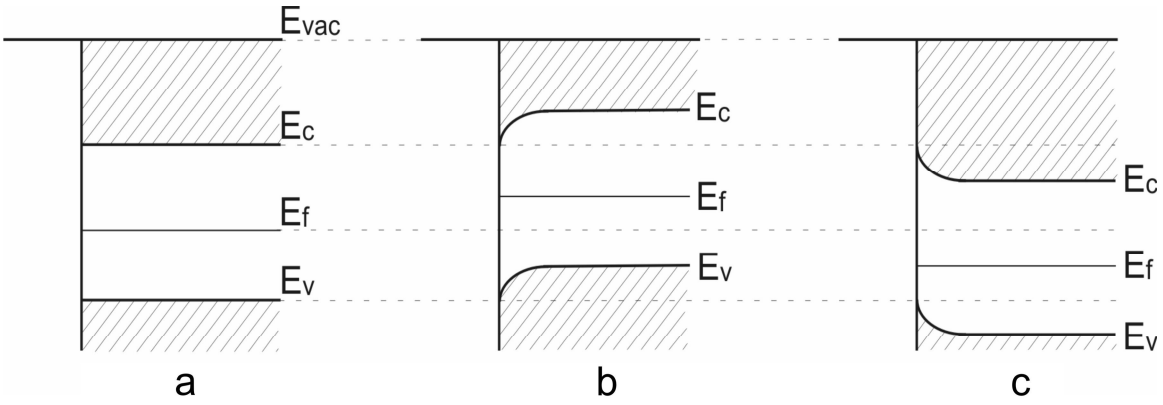

Figure 1.1. Bands bend on semiconductor surface:
a – neutral surface, b – positively charged, c – negatively charged

Concentration of surface centers $(O^{2-})_{surf}$ is controlled by the composition of gas phase, including oxygen partial pressure in the synthesis process. Fully oxidized surface is characterized with the presence of bridging oxygen atoms, coupling two tin atoms. Concentration of bridge atoms decreases proportionally to partial pressure of oxygen. Fully reduced surface almost doesn't contain bridging oxygen. In the presence of other molecules in the gas phase, the surface contains different adsorbed particles.

1.1.2. Titania bulk properties in comparison with the properties of tin dioxide

TiO_2 is an n-type semiconductor with energy gap width 3.0-3.2 eV. Titania has a wide range of applications, from sunscreen paint to food coloring.

Titanium dioxide has eight modifications – in addition to rutile, anatase, and brookite, there are three metastable phases which can be produced synthetically, and five high-pressure forms. The metastable phases, including anatase and brookite phases, convert to rutile upon heating (see paragraph 1.1.3).

Despite the band gap width of titanium dioxide is lower than that of tin dioxide, its samples have higher electrical resistance. It is related to the distribution of impurity levels, located deeper than in the case of tin dioxide. From one hand, high resistance may be considered as an advantage, since it leads to an increase of response. From the other hand, if the resistance of the sample is higher than 10^9 Ohm, signal measurement can present technical difficulties.

Titanium dioxide melting point is higher than the melting point of tin dioxide, so highly dispersed TiO_2-based samples can resist heating to 600 ^oC without significant lose of sensitivity.

Tin and titanium dioxides possess iso-structural crystalline modification – both crystallize in rutile type structure. Similarity in the crystalline structure ensures formation of solid solutions as well as decreases electron scattering on the interphases between contacting crystallites [2, 3]. In spite of structural similarity, the oxides differ remarkably in their electronic properties. N-type conductivity of both materials is mainly determined by under-stoichiometric amount of oxygen atoms in the crystalline lattice. The latter gives rise to numerous donor states within the wide band gaps. For SnO_2, the surface donor states are located at ca. 114 meV below the conduction band, while for TiO_2 – ca. 800 meV below Fermi level [4, 5]. The difference in shallow levels position explains the high resistance of TiO_2 based materials at sensor working temperatures. It also suggests that in SnO_2-TiO_2 system, electrons generated either due to temperature or surface reaction will migrate

towards TiO_2, causing electron depletion in SnO_2 phase, likewise in the case of PdO and Ag_2O[4].

Another important observation for gas sensors is thermal stability of surface and bulk composition in the dispersed SnO_2-TiO_2 system. At 1430 ^oC, the phases are known to form solid solutions in all ranges of SnO_2/TiO_2 ratio. However, upon cooling, the solid solution undergoes spinoidal decomposition if the ratio is within the miscibility gap observed between ca. 15 and 85 mol.% of TiO_2 [6, 7]. In spite of being separated, the oxide phases within the gap are rich in Ti and Sn [8]. This suggests that using either mechanically mixed phases or co-precipitated ones, an interfacial diffusion between the phases can occur slowly until the phases get saturated with respective metal ions. Such effect is especially important for long-term stability of the sensors, since diffusion in polycrystalline material leads to recrystallization and particle growth.

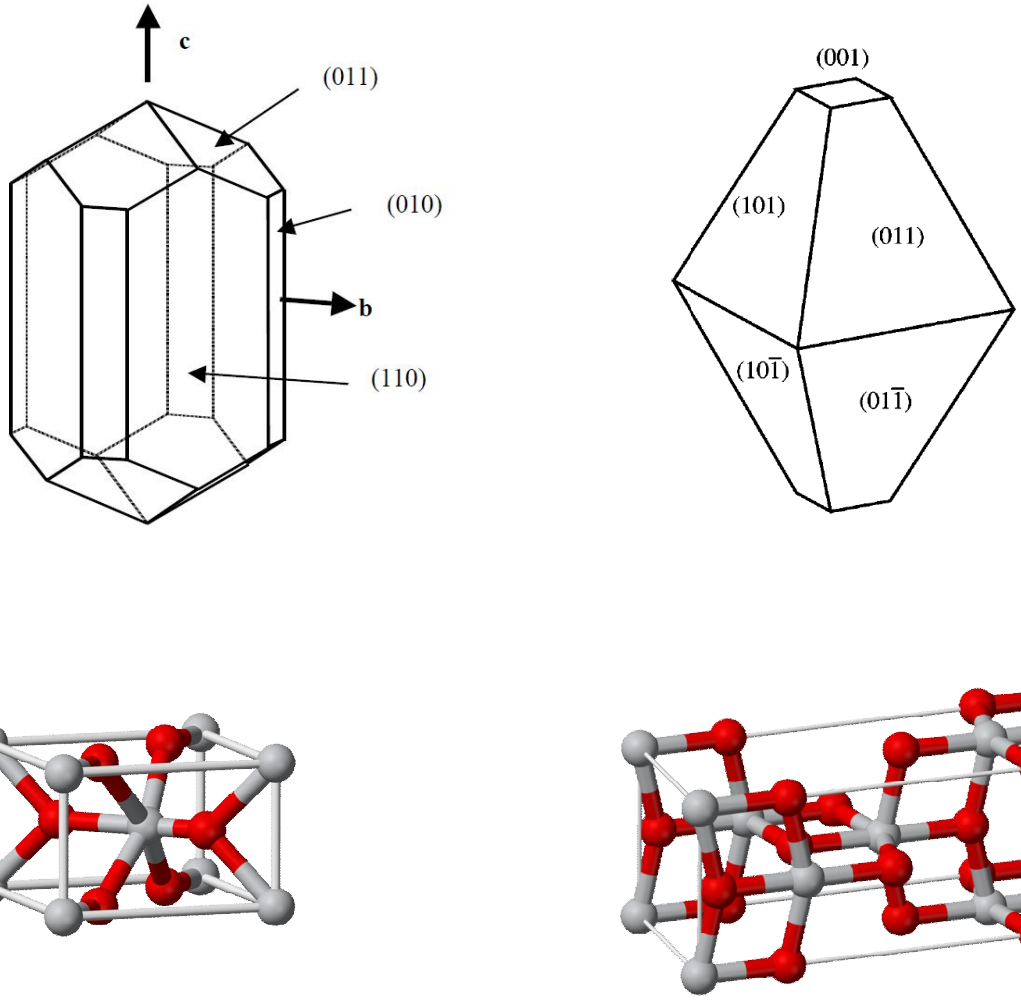

Figure 1.2. The equilibrium shapes of a TiO_2 crystal in rutile phase [8] and in anatase phase [9], their crystal structure and photo images of rutile and anatase minerals.

1.1.3. Structural stability of titania thin films

As mentioned above, there are three main types of TiO_2 structures: rutile, anatase and brookite. The particle size dependence related tothe stability of various TiO_2 phases has recently been reported [11, 12]. Rutile is the most stable phase for particles above 35 nm in size [11]. Anatase is the most stable phase for nanoparticles below 11 nm. Brookite has been found to be the most stable for nanoparticles in the 11 – 35 nm range, although the Grätzel group finds that anatase is the only phase obtained for their nanocrystalline samples [13, 14].

At temperatures above 500°C, it is observed abnormal growth of titania particles [15]. This phenomenon was investigated by means of TEM microscopy at real time [16]. The specimens were observed in-situ, at temperatures ranging from room temperature to 700°C.

The initial structure of the films [16] consisted of nanocrystalline anatase (~8 nm). Heating titania up to 500°C resulted in the formation of rutile. The larger anatase grains provided nucleation sites for the grains of the new phase to develop. Once formed, rutile grains grew fast, consuming the surrounding anatase matrix grains and transforming them at the same time, thus resulting in single-crystalline arrangements.

At higher temperatures, the rutile grains grew up to 200–300 nm in diameter. The anatase matrix grains, on the other hand, remained small, with an average size of 18 nm.

The in-situ TEM studies directly show that rutile forms first when the fine anatase particles (grains) grow to critical sizes, providing appropriate sites for the nucleation of the stable phase. After the formation of a critically-sized nucleus of anatase, the transformation to rutile appears to begin and proceed very rapidly. The requirement of a critical size nucleus for the onset of the transformation was argued in a recent work on nanocrystalline titania (sol-gel material) by Gribb and Banfield [17].

In the study [16] it was shown that rutile grain growth proceeds as long as there are un-reacted anatase (matrix) grains available to consume. Rutile growth is limited only by the presence of other, surrounding, rutile grains. It is suggested, that the abnormal grain growth observed in titania might be characteristic of such nucleation-limited, polymorphic reactions from a metastable to a stable phase.

1.2. Synthesis of sensing materials

1.2.1. Nanopowder synthesis by means of sol-gel method

Methods of preparation of nanocrystalline semiconductor oxides play key role in the formation of sensing parameters, including, besides of signal value, time of response and recovery, stability and working temperature. Furthermore, synthesis method has an impact on the cost of a sensor and defines the possibilities of a large scale production. The most perspective forms of sensing layer are thin and thick films because of their durability, low power consumption and potentially low cost [18, 19].

Methods of “soft chemistry”, related with the use of salt solutions as precursors, were successfully applied for preparation of nanocrystalline oxide powders in the last decade [20]. Among principal methods being practically applied nowadays one can single out two main groups:

1) Method of poorly soluble compounds (oxides hydrates, basic carbonates) precipitation with the use of inorganic salts hydrolysis.

2) Methods based on the application of colloid solutions as precursors (sol-gel method, kryosol-gel method).

Among the advantages of precipitation method are its simplicity (no need for complex and expensive equipment) and variety of existing methodologies that allow to obtain a wide spectra of materials with predetermined microstructure (grain size, porosity, value of specific surface area). The method also gives an opportunity to insert dopants at different synthesis stages, thus providing control of composition and relative distribution of the components. The main synthesis parameters are:

1) Composition and concentration of initial solutions;

2) Temperature of sedimentation;

3) pH of sedimentation;

4) Thermal treatment of the obtained sediment.

Let us consider main dependences of amorphous hydroxides formation from salts water solutions.

Sol–gel processing is a form of nanostructure processing and refers broadly to room temperature solution routes for preparing oxide materials [18]. The precursors used in this method provide the formation of colloidal particles. In the case of nanopowder formation (see Figure 1.3), the obtained colloidal particles are precipitated and collected.

Particles in solution carry electric charge which is dependent on the pH of the suspension and the adsorption of ions. This charge results in the formation of an

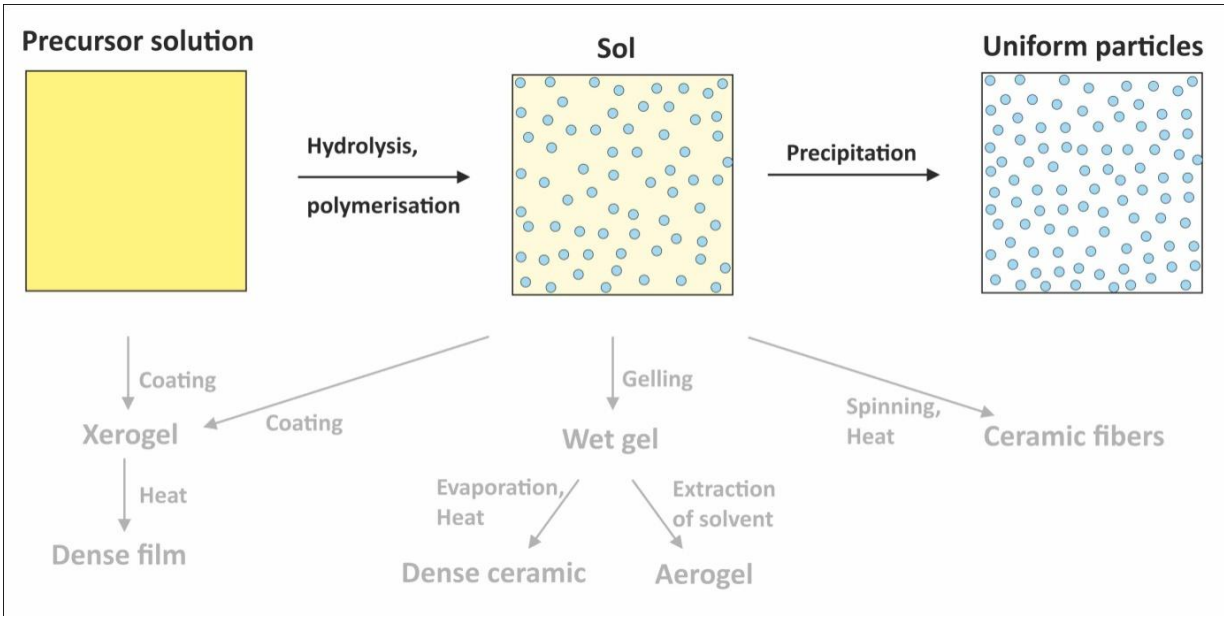

Figure 1.3. Nanomaterials fabrication by means of “wet chemistry” methods

electrical double layer around the particles and an isoelectric point may be defined at a certain pH value [18]. Thickness of the electrical double layers of the particles defines interaction between them. Particles with similar electrical double layers repel each other in the case of low ionic strength of the suspending medium. Thus, when pH is far from isoelectric point, the suspension is not structured. In contrast, there is no repulsion between the particles at the isoelectric point, so the particles get together due to van der Waals’ forces and coagulation occurs. The dependence of reaction rate on pH value can be estimated by the time required for gel

formation. The gelling time is the longest at the isoelectric point, and rapidly decreases in more acid or more basic media.

1.2.1.1. Physicochemical basis of nucleation and growth of crystallites in solution

Very large part of the atoms constituting a nanoparticle belongs to its surface. The surface of nanoparticlesis is very active [18, 21]. At nanoscale dimension the high surface energy gives materials thermodynamic instability or metastability. A system is said to be in thermodynamic equilibrium when it is at its lowest energy state, which corresponds to the minimum of Gibbs energy. The equilibrium shape of a crystal being formed in solution can be directly derived from the surface energies by the Wulff construction [31], in which the perpendicular distance h_i, from the ith face to the center of a crystal of each face is proportional to its surface energy, S_{ri}. However, in the case of the crystallites of 1–2 nm in diameter, the growth of an ordered crystallographyc structure is stopped in the beginning of the process, what leads to high surface energy of such particles.

For the formation of nanoparticles by homogeneous nucleation, a supersaturation of the growth species must be created. The overall excess energy, ΔG, between a small solid particle of a solute and the solute in solution is equal to the sum of excess surface energy, ΔG_S, and the volume excess energy, ΔG_V. $\Delta G_S$is the excess energy between the surface of the particle and the bulk of the particle and is proportional to square of the particle size (r^2). ΔG_V is the excess energy between a very large particle and the solute in the solution and is proportional to r^3. Thus we have

$$\Delta G_V = \Delta G_S + \Delta G_V = 4\pi r^2\gamma + 4\pi r^3 \Delta G_V | 3 \qquad (1.3)$$

γ is the interfacial tension between the developing crystallite surface and the supersaturated solution. Here ΔG_V is a negative quantity, and ΔG_S is a positive quantity.

The two terms on the right-hand side of Equation (1.1) have opposite signs and depend differently upon r. Therefore, the Gibbs energy of formation, ΔG, passes through a maximum, as shown in Figure1.4. This maximum value ΔG_{crit} corresponds to the critical nucleus, r_c, and for a spherical cluster can be obtained by setting

$$dG/dr = 8\pi r\gamma + 4\pi r^2 \Delta G_V = 0 \quad (1.4)$$

$$r_c = -2\gamma / \Delta G_V \quad (1.5)$$

$$\Delta G_{crit} = \frac{16\pi\gamma^3}{3(\Delta G_v)^2} = \frac{4\pi\gamma r_c^2}{3} \quad (1.6)$$

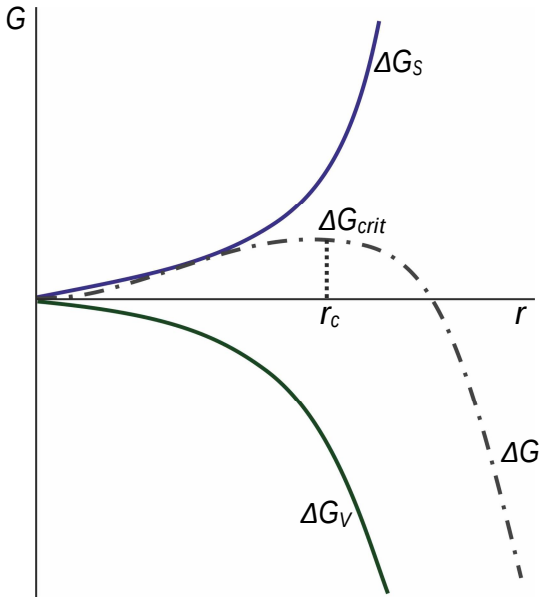

Figure 1.4. Free-energy diagram for nucleation processes

So, ΔG_{crit} is the energy barrier that a nucleation process must overcome and r_c represents the minimum size of a stable spherical nucleus. The process of enlargement of bigger particles at the expense of smaller ones is known as Ostwald ripening.

The change in the chemical potential of an atom transferring from a spherical surface of radius r_a to r_b is given by

$$\Delta\mu = 2S_r\Omega\left(\frac{1}{r_a} - \frac{1}{r_b}\right). \quad (1.7)$$

The largeparticle continue growing at the cost of the smaller particle, until the concentration of solid in thesolvent equals the equilibrium solubility of the relatively large nanoparticle. The reduction of overallsurface energy is the driving force for the surface restructuring and the formation of faceted crystals.

1.2.1.2. Influence of pH and ionic strength on the size of the nanoparticles in solution

As mentioned, the driving force of the process of nucleation and growth of nanoparticles in solution is the reduction of Gibbs free energy. When temperature of the solution changes to make it a supersaturated solution, Gibbs free energy increases [21]. Surface energy of dispersion can be expressed as γA, where γ is the interfacial tension and A is the surface area of the particles in dispersion. In the case of nanometric particles, the surface energy has significant impact on the free enthalpy of the dispersion. This means that most ultra-divided suspensions are thermodynamically unstable and spontaneously evolve in order to decrease the surface area. In other words, during initial steps of precipitation – nucleation and growth – the particles may be formed under kinetic control. In this case, free enthalpy of the system may increase by reduction the surface area during the process of dissolution of smaller particles and cristallisation of bigger ones (Ostwald ripening). This results in the growth of particles, or aggregation and coalescence [22]. However, enthalpy of the system can be lowered along with decreasing of surface area in the case of either *a)* adsorption of surfactants on the surface of the disperse phase particles or *b)* presence of charged molecules in the solution (increase of ionic strength of the solvent). In these cases, interfacial tension decreases, lowering free enthalpy of the system:

$$d\gamma = -\Sigma \Gamma_i d\mu_i \qquad (1.8)$$

where Γ_i is the density of adsorption of species i with electrochemical potential μ_i. Thus, lower interfacial tension leads to less energy of the precipitate formation,

despite of its larger surface area. Higher number of adsorption sites is formed in this case, and the concentration of adsorbable species (protons or hydroxyls ions depending on the pH of the medium) increases. Microemulsions are the best example of thermodynamically stable dispersed systems which owe their stability to very low interfacial tensions due to adsorption of tensio-active agents [23].

In the case of the synthesis of sols of metal oxides in aqueous solutions, the electrostatic surface charge of particles (as well as the composition of surface species) is dependent on pH and the ionic strength of the solution. Hydrogen ions concentration (pH) changes affect protonation–deprotonation equilibria of surface hydroxylated groups. Total concentration of ions in solution (ionic strength) carries out screening between charged groups on the surfaces, affecting electrical charge of the particle surface. Adsorption of ions presented in the solution on the surface of particles and settling of the surface electrical charge induces a decrease in the interfacial tension with respect to its value at the point of zero charge (PZC) [24].

Electrostatic screening between charged groups depends on the surface charge density, being more efficient when the surface charge density is higher. For example, ionic strength has only a very little effect on particle size for anatase (low surface charge dencity) and a higher effect for magnetite [23].

The aqueous chemistry of metal cations allows one to control crystalline structure, particle size and shape of alumina, iron and titanium oxides precipitates [22]. The main parameters which contol the properties of the precipitates are the acidity of the solution, the presence of specific anions, and the temperature. The acidity and the temperature govern hydroxylation of metal complexes leading to the solid formation [22]. Species complexing the cations play an important role in the shape and size of oxide nanoparticles [25, 26]. In the absence of such species, the acidity induces a specific dependence of the particle size as described above. Precipitating the solid at a pH far from the PZC and under a high ionic strength, i.e., under conditions where the electrostatic surface charge is high enough, it is possible to escape from the kinetic control of the process [23]. In this case, Ostwald ripening

stops, and the particle size is controlled mostly with the pH of the medium. The tight correlation between the particle size and the electrostatic surface charge density suggests that the stability of such systems results from thermodynamic rather than kinetic effects, as for microemulsions, and is associated with a lowering of the oxide–solution interfacial tension [23, 24]. Experimental arguments showing the role of thermodynamic effects in the stabilisation and tailoring of oxide nanoparticles and semi-quantitative model predicting the role of ionic strength and pH in the growth of metal oxide precipitate were brought in [24].

1.2.1.3. Influence of diffusion on the kinetics of precipitation process

According to the Einstein–Stokes theorem [27], the diffusion coefficient (D_η) of a solute of radius (r) in a solvent is in reciprocal proportion to the viscosity of the solution (η), and is given by

$$D_\eta = kT \mid 6\pi\eta r \qquad (1.9)$$

where T is the temperature of the solvent. At the formation of nanodisperse medium, nucleation compete with crystal growth. Relative velocity of these processes is partly controlled by diffusion. If the viscosity of the medium is high, the rate of diffusion lowers and particles grow larger.

The rate of nucleation is

$$J = Aexp\left[\frac{-16\pi\gamma^3 v^3}{3k_B^3 T^3 (lnN)^2}\right] \qquad (1.10)$$

where 'v' is the molar volume, and 'N' is the ratio of solution concentration to that of equilibrium saturation concentration at a given temperature, and is given by

$$lnN = \frac{2\gamma v}{k_B T r_c} \qquad (1.11)$$

Thus, temperature (T), degree of supersaturation (N), and interfacial tension (c) are the three main variables which govern the rate of nucleation. Equation (1.11) gives the critical nuclei size as

$$r_c = \frac{2V\gamma}{3k_BTln(N)} \quad (1.12)$$

At fixed *N*, all agglomerates with $r \gg r_c$ and all agglomerates with $r < r_c$ dissolve. So, the higher is the degree of supersaturation*N*, the smaller is the critical nuclei size r_c.

There is a certain concentration of precursor below which nucleation stops. Another (lower) critical concentration value corresponds to the termination of the growth of agglomerates. When the concentration of the precursor is between these two points, there is no formation of new nuclei in the solution, but the present nuclei continue growing. At this stage, smaller particles grow more rapidly than larger ones. This is because the Gibbs energy driving force is larger for smaller particles than for larger ones if the particles are slightly larger than the critical size.

Nearly monodisperse size distribution can be obtained at this stage by stopping the reaction (nucleation and growth) after the moment when all nuclei have approached to a certain size, but Ostwald ripening has not occurred yet. This is possible when smaller particles in the solution are just slightly larger than the critical sizer_c. The Gibbs energy driving force is very high for such particles.

When the concentration of the precursor lowers due to particle growth, Ostwald ripening occurs. At this new concentration, the saturation ratio *N* decreases and the corresponding critical nuclei size *r* increases. Particles smaller than this new critical size dissolve. In addition to the growth by precipitation reaction, where soluble species deposit on the solid surface, particles can grow by aggregation with other particles, and this is called secondary growth. After the particles grow to a stable size, the growth continues by combining with smaller unstable nuclei and not by collisions with other stable particles. Nanoparticles are small and are not thermodynamically stable for crystal growth kinetically. To finally produce stable nanoparticles, these nanoparticles must be arrested during the reaction either by adding surface protecting reagents, such as organic ligands or inorganic capping materials [28], or, by placing them in an inert environment such as an inorganic

matrix or polymers [29]. The nanocrystal dispersions are stable if the interaction between the capping groups and the solvent is favorable, providing an energetic barrier to counteract the van der Waals' and magnetic attractions between nanoparticles. To help arresting these nanoparticles, different solvents are also used to change the solubility or the reaction rate [30].

1.2.1.4. Chemical reactions during sol-gel synthesis of SnO_2

First mechanism describing the formation of multichargecations was proposed in coordination theory. The principal assumption of this theory is that monomeric hydroxide particles are formed in the solution, afterwards aggregating and forming colloidal solutions or amorphous sediments. In works [32-34] arose a new point of view, according which amorphous hydroxides are formed by means of continuous growth of polymeric formations until achievement of molecular weight corresponding to the weight of colloidal particles with further coagulation of these formations. Thus, at every point of time there are hydroxopolymers with different molecular weightsin solution, what makes it difficult to predict the composition, structure and properties of the forming sediments. It is supposed that condensation of individual hydrated metal ions occurs at the initial stage of hydrolysis and leads to formation of bi- and oligomerichydroxocomplexes. However, polymerization process doesn't continue until the formation of colloidal particles. For every cation there are one or several corresponding so called "*irredundant forms*" of polyhydroxocomplexes (PHC). After their formation, condensation process is usually stopped. Such "irredundant forms", that usually contain several tens of metal atoms, further combine into colloidal aggregates, and the latest form hydroxide sediment. It is possible to represent schematically the processes of hydrolytic polymerization, as follows:

monomer ↔ dimer ↔ irredundant form of PHC ↔ aggregate ↔ hydroxide sediment

At the stage of polynuclearhydroxocomplexes formation with high enough

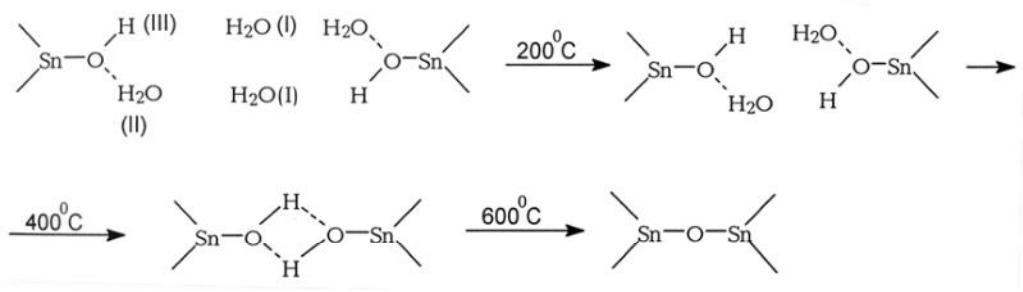

number of oxygen atoms,the equilibrium is established rather slowly. After the achievement of equilibrium, the composition of polymerization products doesn't depend on the method of addition of a base to salt solution. Therefore, the repeatability of sediments properties is determined largely not by the method of sedimentation, but by the conditions in which equilibrium distribution of PHC is achieved at the stage of initial colloid particles formation. In amorphous sediments it is remained short range order of atoms, which is typical for PHC "irredundant forms". The composition and structure of irredundant forms themselves can be directionally changed by variation of metal cations and counterionsand other parameters. Thus, handling of sedimentation conditions (temperature, reagents concentration, pH) allows to change the structure and the properties of the obtained sediment in a controlled way.

Tin (IV) hydroxide (α-stannic acid) represents agglomerates of highly dispersed particles of tin dioxide. The surface of these particles is covered with a net of hydroxyl groups, bounded with water molecules [35]. Freshly prepared α-stannic acid is x-ray amorphous. During aging it transforms into β-form [36]. Aging process can be represented by the following scheme:

From chemical point of view, β-stannic acid is more inert, because *oxolyc* bridging groups (-O-) are less active than *olyc* groups (*HO<).* Moreover, along with

oxolation, elongation of the chains and their coupling with each other takes place, what leads to enlargement of the particles.

Scheme of thermal dehydration of stannic acids was proposed in the work [37] on the basis of the study of specific surface area and materials porosity:

Adsorbed water removal (I) under $T \leq 200\ ^{o}C$ doesn't lead to aggregation and enlargement of the particles. At that, high values of specific surface area (more than 100 m^2/g) remain. Above 200 ^{o}C fast decrease of surface area is observed, because along with removal of water, bounded with tin dioxide by hydrogen bonds, takes place condensation of hydroxyl groups (III), which is accompanied by emission of structural water molecules and grows of secondary aggregated particles. At temperature higher than 500 ^{o}C value of specific surface area becomes minor (less than 30 m^2/g), what along with x-ray diffraction data indicates crystals growth and secondary particles aggregation. Besides of temperature, surface area depends on the presence of foreign ions (for example, sodium and chlorine) [37]. The value of

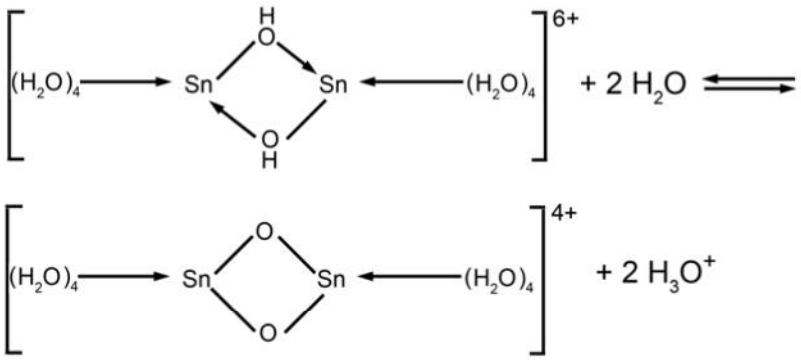

pH during sedimentation is also an important parameter. Surface area decreases with increasing of pH, independently on the nature of initial substances.

1.2.1.5. Approaches to sol-gel method application

Introduction of surface-active compounds in the synthesis process allows obtaining mesoporous tin dioxide with extremely high specific area, up to 350 m^2/g, and pore size 2-4 nm [38-43]. To date, the following synthesis variants are proposed:

S^+I^- [39], S^-I^+ [(39, 40], $S^+X^-I^+$ 41], S^0I^0 [42, 43] and $S^0X^-I^+$ [43], where S – surfactant, X – counterion, I – tin-containing precursor.

When using positively charged template ion [39, 41] like n-cetyltrimethylammonium (CTA^+), an important role in the formation of mesoporous SnO_2 play counterions: Cl^-, Br^- or OH^-, that prevent reciprocal repulsion of positively charged CTA^+ and Sn^{4+}. Introduction of alkaline to the solution, containing template ion, leads to surrounding of a large cation CTA^+ with hydroxyl groups. The latter become centers of mesostructured phase formation when interact with Sn^{4+} ions. In this case, control of introduced hydroxyl groups concentration (pH control) is necessary, because the presence of free hydroxyl groups, i.e., not bounded with CTA^+cations, lead to the formation of monomers $Sn(OH)_4$. These monomers can participate in polycondensation reaction with formation of α-stannic acid, which doesn't have mesoporous structure.

In [41-43] authors used neutral surfactants as a template: octylamine, dodecylamine, tetradecylamin, hexadecylamine, supposing that in this case mesoporous structures with increased thickness of pores walls will be formed and thermal stability will be increased. However, in contrast to mesoporous silicon oxide, which keeps pores structure in the conditions of thermal treatment up to 600°C, the mesoporous structure of tin dioxide is destroyed at T = 400°C in one hour and at T = 300°C in 24 hours [44]. The most stable mesoporous SnO_2 was obtained with the use of n-celyltrimethylammonium bromide (CTAB) in the conditions of hydrothermal treatment [38]. Mesoporous structure was saved stable for 2 hours during treatment at T = 500°C.

Thus, method of chemical sedimentation from inorganic salts solutions allows obtaining nanocrystalline oxides with predefined microstructure (cryllites size, surface specific area value, pores diameter). Oxide properties are defined in the synthesis process by the control of sedimentation pH, presence of admixture ions, choice of precipitator, presence of surfactant and choice of gel crystallization temperature.

Synthesis of nanocrystalline SnO_2 may be carried out in different ways, for example, by sedimentation of α-stannic acid gel with ammonia solution, with hydrazine hydrate, or with ammonia solution in the presence of surfactant like celyltrimethylammonium bromide [44].

Precipitation of α-stannic acid gel is carried out from $SnCl_4 \cdot 5H_2O$ solution during ammonia hydrate addition until pH reaches value 7.0 ÷ 7.5, under continuous stirring, at 0°C:

$$SnCl_4 \cdot 5H_2O + 4NH_3 \cdot H_2O \rightarrow SnO_2 \cdot xH_2O + 4NH_4Cl + (5-x)H_2O \quad (1.13)$$

The sediment was removed by centrifugation, than it was washed out with deionised water to remove chloride ions until the disappearance of reaction to $AgNO_3$, and after that, it was dried at 100°C during 24 hours [44]. The obtained product was grinded at an agate mortar and annealed in air.

In order to obtain material with high specific surface area and stable against thermal impact, the synthesis was carried out by the method described by authors in [45]. Water solution of $SnCl_4 \cdot 5H_2O$ was added dropwise to hydrazine hydrate solution under stirring and at room temperature. An equation for this process was proposed [45]:

$$SnCl_4 \cdot 5H_2O + 2N_2H_4 \cdot H_2O \rightarrow SnO_2 \cdot xH_2O + 4HCl + 2N_2 + 4H_2 + (5-x)H_2O \quad (1.14)$$

The obtained suspension was boiled in a retort with reflux condenser during 10 days. Sediment was separated with centrifugation, carefully washed out to remove chloride ions until the disappearance of reaction to $AgNO_3$, and after that it was dried at 100°C during 24 hours. The obtained product was grinded at an agate mortar and annealed in air at temperatures of 300, 500, 700 or 1000°C during 24 hours.

Synthesis was carried out with the use of a cationic surfactant n-cetyl-trimethylammoniumbromide [46]. Initially, the surfactant was introduced to ammonia water solution and stirred until the formation of a homogenous solution. After that water solution of $SnCl_4 \cdot 5H_2O$ was added dropwise to the obtained

solution, than the obtained suspension was stirred for 5 hours and aged at room temperature for 72 hours. The obtained gel was separated by centrifugation, carefully washed out to remove chloride ions until the disappearance of reaction to $AgNO_3$, and after that it was dried at 100°C during 24 hours. The obtained product was grinded at an agate mortar and annealed in air at temperature of 300, 500, 700 or 1000°C during 24 hours.

The advantage of the methods based on the use of $SnCl_4 \cdot 5H_2O$ is the accessibility of this type of precursor. However, this group of methods has some disadvantages. One of them is the use chloride ions, negatively affecting sensing characteristics. Washing these ions is a long, labor-consuming process.

The method based on the use of tin (II) sulfide[47] as a precursor is similar to the ones described above. Salt water solution is treated with ammonia. However, in this case the obtained material doesn't need to be washed out of chloride-ions.

Nanosized $Ti_xSn_{1-x}O_2$have been synthesized at various Ti molar ratio [49].Sn(II)2–ethylexanoateand Ti(IV) n-butoxide have been dissolved in a hydroalcoholic solution under stirring and maintaining temperature equal to 50 ◦C and totalcation concentration 0.1 M. HNO_3 (pH ∼ 1) was slowly added to the Ti^{4+}/Sn^{4+} solution to slightly modify the hydrolysis rate of Sn–OR bonds with the aim to achieve the simultaneous formation of Ti OH and Sn OH inorganic functions and their further "one-pot" cross-condensation. The resulting colloids were filtrated, washed with diethyl ether and dried in air at 100 ◦C for 15 h. The resulting white powders were calcined at 550 ◦C for 2 h.

1.2.2. Nanowires synthesis methods

This paragraph describes the state-of-the-art strategies for engineering one-dimensional functional semiconductors (1.2.2.3). In the beginning, the influence of the dimensions on the properties of the materials and their related applications are highlighted (1.2.2.1). The use of bottom-up and top-down approaches is discussed (1.2.2.2).

1.2.2.1. Properties and applications of nanowires

Inorganic structures confined in several dimensions within the nanometer range, exhibit peculiar and unique properties superior to their bulk counterparts [50]. These unique properties can be attributed to the limited motion of electrons in the confined dimensions of the nanomaterial (quantum effects) [50, 51]. Size-dependent physical properties observed in 1D nanomaterials include photon absorption and emission, such as nanoscale avalanche photodiodes [52], metal-to-insulator transition in a material [53] and quantized or ballistic transport characteristics [54].

Nanowires have been defined as wires with at least one spatial dimension in the range of 1–100 nm [55–61]. Size-dependent physical properties of nanowires are widely used in sensing technology [62–67]. In comparison with traditional types of sensors based on semiconducting films, the devices utilizing nanowires as sensing elements have some peculiarities.

Due to the tiny size of nanowires, it is enough only few molecules to change their electrical properties, what can result in a very high sensitivity of nanowire-based sensor devices. The negligible volume of a nanowire ensures faster response in comparison with other types of the sensors. Polymeric single nanowires were used as sensing elements for optical sensors. During humidity sensing, the response time was 30 ms, and NO_2 and NH_3 gases were detected at sub-ppm level [68].

Ethanol sensor utilizing indium-doped tin oxide nanowire as a sensing element demonstrated response and recovery time less than 2 s [69].

Compactness and low power consumption of nanowires give promising opportunities to use them as components of sensor arrays. Single nanowire sensor array become a powerful alternative for a set of bulk traditional sensors and seems to be a good candidate to be a sensing element in a single device that integrates the sensing and signal processing functions in one chip [57-64]. Single-nanowire array consisting of four different materials from three categories, which are metal (palladium), conducting polymer (polypyrrole and polyaniline), and semiconductor (zinc oxide) was used for a real-time detection and identification of multiple gases including hydrogen, methanol, carbon monoxide, and nitrogen dioxide [70]. Sub-ppm detection limit was achieved; each single nanowire showed excellent sensitivity at room temperature.

Low power consumption enables better possibilities for the production of wireless detached devices [71, 72]. The use of wireless devices integrated in a sensor network with wireless (e.g., wi-fi) signal output is a promising technology for the gas sensing market [103-105]. Since very small amounts of gas can change the electrical characteristics of nanowires, the sensors can work at lower-operating temperatures. Some single nanowire sensing devices show extremely low power consumption levels of 15–30 microwatts, being at the same time selective to the target gas [73].

1.2.2.2. Top-down versus bottom-up synthesis techniques

A great number of publications were devoted to the description of new methods of nanowires synthesis last years, however, generic methodologies are limited. They are commonly classified into two categories [74–76], the bottom-up and top-down approaches.

The initial materials in top-down approach are large scale patterns being reduced in lateral dimensions to the nanoscale. In silicon technology, one of typical top-down approach methods involvers optical and X-ray lithography, e-beam and ion-beam lithography, printing and imprinting, scanning probe lithography, etc. One of the main advantages of the top-down approach is that the nanomaterials are both patterned and built in the same place, so there is no need in an assembly step [78], neither a (self-)ordering step. Another advantage is high homogeneity of the dimensions of obtained structures [79].

A shortcoming of the top-down approach is that it can be difficultly implemented for the fabrication of nanoscale objects [76]. Furthermore, this approach is based on the use of planar techniques, deposition and etching of patterned layers, what limitates the forms of possible three-dimensional objects. And probably one of the most pronounced shortcomings of the top-down approach is high cost of the product, particularly when fabricating high-resolution structures [75].

The initial materials of the bottom-up approach are the compounds in the form of molecules and atoms; the nanostructures are built up with the use of chemical reactions or self-assembly [75, 77, 80]. The synthesis techniques based on bottom-up approach include such methods as vapor-liquid-solid (VLS) growth, chemical vapour deposition (CVD), sol-gel synthesis, plasma or flame spraying synthesis, laser pyrolysis, atomic or molecular condensation, layer-by-layer self assembly, molecular self assembly, coating and growth, direct assembly, etc [55].

From the point of view of lab synthesis, bottom up techniques are the most used due to the high purity and small dimensions achievable [93].

From the point of view of commercializing of the nanowire fabrication processes, the advantage of bottom-up approach is the possibility of scaling the production to the industrial scale in a cost-effective way.

Nanowire synthesis by the means of bottom-up approach methods can be carried out directly on a substrate; furthermore, this can be any substrate, including flexible plastic chips [82-84]. The dimensions of the nanoscaled objects obtained with such techniques range from angstroms to hundreds of nanometers [75–78, 80, 85]. However, despite of significant advantages of the bottom-up approach, it is difficult to construct complicated hierarchic structures by bottom-up self-assembling processes. Positioning of assembled patterns on specific locations is particularly difficult in fabricating the required structures in practical applications [55, 81, 86].

It is possible to consider a new nanofabrication technique [78], based on iterative size reduction, to produce ordered, indefinitely long nanowire and nanotube arrays, as a coupling of these two approaches. Well-ordered, globally oriented, indefinitely long nanowire and nanotube arrays with different materials were fabricated using a new top-down approach method, iterative thermal size reduction [28]. A macroscopic multimaterial rod was reduced to ordered arrays of nanowires in a protective polymer matrix. Millions of kilometer-long semiconducting, piezoelectric and polymer nanowires with sub-10 nm diameter and an aspect ratio of 10^{11} were produced.

Both approaches are used for the fabrication of sensing devices based on nanowires [77, 80]. Top-down methods are used for making connections, and bottom-up techniques are used for assembly and establishing short-range order at nanoscale dimensions. The combination of top-down and bottom-up methods enables the progress in the production of cost-effective nanostructures and development of advanced technologies [75, 81, 87 – 90]. Using the combination of CVD, VLS, printing and photolithography techniques, highly ordered and parallel

arrays of optically active CdSe nanowires and high-mobility Ge/Si nanowires were deterministically positioned on substrates, and configured as photodiodes and transistors, respectively [91]. Large-scale integration of nanowires for heterogeneous, multifunctional circuitry was achieved in this work, what demonstrated great potential of systems based on printed NW arrays. Later works demonstrated that this method is applicable for the fabrication of numerous devices with high uniformity [92].

1.2.2.3. State-of-the-art strategies for engineering one-dimensional functional semiconductors

One of the first techniques developed for preparing micro- and nano- structures, was vapor phase growth. It consists in the evaporation of source material in a tubular furnace. The evaporated source material is transported by a gas carrier toward a colder region, where it condensates and nucleates on growth sites [102].

Condensation on the target could happen according to two different mechanism: vapor–liquid–solid (VLS) or vapor–solid (VS). VLS mechanism [106-108] is named after the three different phases involved: the vapor phase source material, the liquid catalyst droplet (consisting of the preliminarily deposited on the substrate colloidal particle of a noble metal) and the solid crystalline produced nanostructure.

Vapor-solid mechanism consists of a direct condensation from the vapor phase without the use ofcatalyst. Source material is vaporized under high temperature, and then is directly condensed on the target substrate placed in the low temperature region. The initially condensed molecules form seed crystals serving as the nucleation sites [102].

1.2.2.3.1. Non-metal seeded gas-phase growth / vapour–solid (VS) or self-catalytic growth mechanism

In the absence of metal catalysts, the growth front plays a crucial role in the adsorption of phase-forming atoms or species [50]. At that, the roughness of the front is of great importance, since the presence of defects, such as screw-dislocations, is mandatory to continuously provide atomic steps, where the diffusing species can bond.

Pure vapor transport synthesis is the process of resublimation of evaporated precursor onto the substrate. The morphology of the obtained nanostructure is greatly affected by such parameters as substrate temperature, composition and pressure of the gas phase. Nucleation can be induced by defects located on the growth front. Another possible mechanism of nucleation is self-catalytic or metal induced growth [98]. Metal particles are present in the nanostructure during the synthesis due to the reduction of the oxide [99]. Thus, nanostructure growth is promoted by both self-catalysis and defect induced growth which runs by means of, accordingly, resublimation or carbothermal transport. The control of growth kinetics during the synthesis by the method using vapour-solid (self-catalitic) mechanism allows obtaining complex nanobelt-based 1D structures like rings and helices [100].

1.2.2.3.2. Metal-promoted vapour growth

The methods attributed to metal-promoted vapour growth include thermal and pulsed laser induced evaporation, chemical vapour deposition (CVD) and molecular beam epitaxy (MBE).

Thermal evaporation is used for the fabrication of the nanostrucutres from initial materials with high melting point. The material is transferred to the vapor phase by means of the heating to high temperature.

In the case of pulsed laser deposition, solid phase material is evaporated through high energy laser pulses.

In molecular beam epitaxy method, the phase-forming material is evaporated under high vacuum. After that, the components of the phase-forming material react on a substrate surface forming the desired structure.

The group of CVD methods allows the widest variation of deposition parameters. Precursor-to-material conversion process can include thermolysis, hydrolysis, oxidation, reduction, disproportionation, nitration and carboration. Depending on the polarity of the gaseous species in comparison with the surface of the substrate, they can either adsorb directly on the surface or on the catalyst particle. The following growth of the nanostructure depends on such parameters as diffusion rate and relative concentration of the precursor (achievement of supersaturation state).

A common technique for creating a nanowire is vapor-liquid-solid (VLS) synthesis. It uses either laser ablated particles or a feed gas such as silane as a source material. VLS synthesis requires a catalyst. For nanowires, the best catalysts are liquid metal (such as gold) nanoclusters, which can either be self-assembled from a thin film by dewetting, or purchased in colloidal form and deposited on a substrate.

VLS mechanism was discovered in the early 1960s by Wagner and Ellis [101]. The whiskers they obtained had hemispherical tips. The mutual solubility of gold and silicon let make a supposition that gold clusters act as a nucleation site for Si crystals.

During the synthesis by means vapor-liquid-solid mechanism, the precursor being adsorbed from the gas phase on the surface of the substrate preferentially decomposes on the liquefied alloy droplet. The droplet becomes supersaturated and the material is transferred to the interface between liquid alloy droplet and the solid body of the nanostructure.

Metal particles have several main functions in the vapour-liquid-solid mechanism: metal particle absorb the precursor, catalyzes precursor decomposition reaction, and finally localizes precipitation of the material.

Absorption of precursor species from vapor phase or substrate surfaces is driven by lowering the chemical potentials of the sources.

Metal droplet acts as a catalyst for the precursor decomposition reaction. However, in many cases metal particle does not lower the activation energy for the decomposition of the precursor species, so the metal particle catalitic activity is not the only driving force of the VLS process. For example, in the case of molecular beam epitaxy, metal promoted nanowire formation cannot be attributed to the catalytic activity of the metal particle.

Finally, alloy droplet localizes the precipitation of the source material on the interphase boundary, between the droplet and the body of the nanostructure, what results in the nanowire formation.

In conclusion, it is possible to call the droplet of the metal a “catalyst” since it enables the formation of the nanowire and is not consumed itself. But the catalitical activity of the metal against the chemical reaction of precursor decomposition is not the only way the droplet enables the nanowire growth. Selective absorbtion of the precursor from the ambient onto the droplet and precipitation of the source material on the interphase boundary (physical process) can be the driving force of the nanowire growth even without catalytic activity of the metal.

1.2.2.3.3. Other approaches to 1D nanostructure synthesis

Crystal structure governed nucleation in solution is based on the natural property of some materials demonstrating preferential growth directions under appropriate experimental conditions such as nucleus formation, concentration, pH and ionic strength [94]. However, only few materials such as Se and Te can form high aspect ratio (>200) nanostructures [95, 96] during the growth in solution. Most of other materials need special conditions to form 1-D materials, like, for example, addition of surfactants to the growth solution which leads to site-specific adsorption [97].

Metal-assisted growth in liquids is a technique, in general, similar to the growth of nanowires on surfaces from a vapor phase. Two mechanisms are commonly distinguished, depending on the synthesis conditions: solution–liquid–solid (SLS), in the case of standard pressure [109-111], or a supercritical-fluid–liquid–solid (SFLS) mechanism under high pressures [110]. In the SLS process, the solvent requirements generally include a high boiling point liquid, which is stable up to 400 ^{o}C, and a low melting point metal growth seed (Bi, Sn, In, Bi/Au, etc.) [50]. First step of the process is the creation of metal colloid, which plays the role of particle–solid interface, where the metalorganic species decompose and form single crystalline wires [111].

The main differences of SFLS growth process from SLS mechanism are higher temperature (<550 ^{o}C), high pressures in the range of 200–300 bar and simple solvents, such as hydrocarbons (hexane and toluene) and CO_2 [50].

Metal-assisted growth in liquids allows fabrication of small diameter 1D nanowires (4–10 nm) with narrow size distribution and with high yield. Catalytic particles should be chosen according to the precursors and conditions used.

Template synthesis of 1D nanostructures is based on filling or covering template structure with its following removal. Typical templates are anodic aluminium oxide and polycarbonate membranes. These templates can be filled or covered with a thin layer of the desired material from metalorganic precursor solutions and subsequent thermolysis [112], by electrolysis [113-116] or by ALD (atomic layer deposition) techniques [117]. In addition, high pressure injection [118] and supercritical fluid inclusion methods [119] or capillary force [120] are appropriate techniques to fill the pores with inorganic materials. In addition, metal-assisted growth techniques may be used in combination with template synthesis methods in order to localize the starting point of the nanowire growth form aligned nanowire arrays by CVD [121,122] or supercritical fluid synthesis [123]. Positive replication, which means coating the outermost surface of 1D materials, such as carbon nanotubes or oxides, is also a prosperous technique [124]. In this approach the

templating material can act as a removable skeleton, hybrid structure or second reagent for solid phase reactions [125].

The drawback of template-assisted growth method is the predominantly polycrystalline nature of the obtained material.

Soft templates method is based on the use mesophasic structures built with the use of surfactants, in order to achieve self-assembly of target compound micelles. The solution where self-assembly take place is a water–oil–surfactant system. The shapes and aspect ratio of the formed structures depend on the presence of specific anions in the solution [126]. Therefore, selective ion adsorption on facets is an important factor for the crystal growth [127, 128].

Electrospinning method uses an electrical charge to draw very fine (typically on the micro or nano scale) fibers from a liquid. The method was traditionally used for polymeric fiber production. A high voltage is applied to a capillary through which a polymer/solvent mixture is guided and a metallic plate acts as counter-electrode and collector. Fluid string between the electrodes forms the fibers on the metallic counter-electrode via evaporation of the solvent [50]. The solution applied in this technique consists of solvent, polymer and precursor and either includes metalorganic monomers or pre-formed particles [129]. The fibersobtained by this method are generally organic–inorganic hybrids, which are either used as obtained [130] or transferred in a purely inorganic material by calcination.

Top-down approach methods most widely applied for the fabrication of 1D nanostructures are chemical and ion beam etching [131]. Due to facet dependent etching rates, pre-defined shapes can be produced from preliminary masked areas [50], which have been demonstrated for compound semiconductors such as InP and GaAs [132]. The techniques used enable lift-off of the wires and their transfer to the desired surface [133]. Another advantage of top-down techniques is the preorientation of the obtained structures, what makes postalignmentunnecessary. A critical step for the etching of nanostructures is the accurate transfer of mask features to the surfaces, which becomes complicated for high density arrays and

very small feature sizes and will limit the progress in this area using conventional approaches [50].

1.2.2.4. Tin dioxide nanowire synthesis

Tin (IV) oxide applications include gas sensing, heating elements and solar cells. Alkoxide-based gold-catalyzed CVD growth methods allow obtaining SnO_2 NWs with well controlled diameter and orientation [134, 135].

Tin vapor oxidation in oxygen containing ambient is a valid approach for the fabrication of 1D SnO_2 nanostructures [136, 137]. The oxidation takes place at temperatures between 900 and 950 ^oC; the substrates may be coated with gold or remain uncoated.

Pulsed flow mode during vapor-solid synthesis of tin dioxide nanowires from SnO leads to the formation of kinked wires [138].

Low oxygen partial pressure during the synthesis of nanowires [139] and nanobelts [140] results in the formation of the orthorhombic form instead of the common rutile crystal structure SnO_2.

Carrier gas flow supported thermal evaporation of SnO or SnO_2 powders enables nanobelts fabrication in high quantity [141].

Tin oxide nanowires were formed by means of laser ablation of pure tin in an oxidizingAr/O_2 atmosphere [142]. The same process with the use of a SnO_2 target at low pressures leads to single crystalline nanobelts [143].

Single crystalline SnO_2 nanowires were obtained by the means of carbothermal synthesis. Self-catalyzed growth mechanism was described [144].Pd, Ag, Al, Cr, Fe, Co, Ni, Cu and Au were investigated as seeds for carbothermal synthesis of SnO_2 nanowires [145].

Another approach to tin oxide nanowires fabrication is electrodepositionof metallic tin wires within AAO template membranes with the following oxidation [146,147].

Polycrystalline SnO_2 nanowires can be prepared by electrospinning of mixtures of polymer solutions (poly(ethylene oxide) or poly(vinyl alcohol)) and tin sources, such as tin dioxide sol [148], dimethyldineodecanoate tin [149] or stannic chloride pentahydrate [150].

Pure, polycrystalline tin dioxide fibers can be liberated from the carbon backbone and converted to crystalline SnO_2 by calcination in oxygen containing environments [50].

1.3. Gas sensing properties of different materials

1.3.1. Comparison of sensors based on thin layers and nanowires with sensors based on thick layers

Synthesis by means of thin-layer technology enables to miniaturize sensing devices, to create sensor arrays based on different materials on a single substrate; low thickness of sensing layer assures low power consumption. Thin layers may be fabricated by physical and chemical methods [151]. It is possible to refer to physical methods all ways of fabrication where the transfer of the substance to gas phase is realized by either thermal evaporation, or by means of high energy beams like laser ablation, magnetron sputtering, electronic or ionic beams. Metal oxide films may be obtained by the evaporation of both oxides and corresponding metals with the following thermal oxidation or with oxidation during growth process. A common disadvantage of these methods is the necessity of the use of high vacuum, what increases technology cost.

The methods referred to chemical ways of thin layers synthesis are chemical precipitation from gas phase (CVD) and synthesis with the use of solutions: pyrolysis of aerosols, ion layering method, as well as sol-gel method with different ways of sol deposition onto substrate. Metal simple salts, as well as complex and organometallic compounds, may be used as initial materials.

The most common thin layer deposition method is magnetron sputtering – catodic spraying of a target at plasma of magnetron discharge, i.e., diode discharge in crossed fields. There are different spraying methods. In one case, metal is sprayed in inert atmosphere or in vacuum and oxidized by oxygen after the sputtering process. In another case, small amount of oxygen is contained during sputtering. In all cases, the obtained gas sensing layer needs quite long final oxidation at high temperature.

Magnetron sputtering is well compatible with silicon technology and present promising prospects for the creation of chips that combine low power consumption sensor with electronic unit which control the work of the sensor and register its response. Nevertheless, such chips are not created yet.

One more type of thin layer technology is laser ablation – partial target evaporation under exposure to powerful enough laser impulses and following vapors condensation onto dielectric substrate.

Main advantages of thick layer technology are low cost, possibilities to choose various initial compounds, to increase the scale of production together with integration with other microelectronic technologies. The deposition of thick layers is realized by screen printing method, which includes following main stages [152]: synthesis of active compound powder with predetermined properties, paste preparation with the use of organic solvent with necessary viscosity, paste deposition onto the substrate, paste drying at low temperature, following annealing to remove spacer and to form durable layer. Thickness of the obtained layers varies from units to hundreds of microns. Functional properties of thick layers are determined by both properties of active component and layer structure.

Semiconductor sensor action is based as a rule on heterogeneous catalysis of chemical processes, therefore the surface to volume ratio of gas sensing materials is an important characteristic determining sensitivity. Traditionally, quasi-0-dimentional (i.e., spherical) nanoobjects were usedin order to create highly dispersive materials. Their agglomeration at temperature close to the melting point leads to the formation of a material with high surface to volume ratio. In such methods as magnetron sputtering, laser ablation and spraying, layer-by-layer nanoparticles deposition is used with their subsequent adhesion to the substrate and to the previously formed material. Sol-gel process supposes synthesis of nanopowder which consists of spherical nanoparticles, preparation of the paste from this powder and its deposition and annealing.

The development of sol-gel synthesis of highly dispersive semiconductor materials is slightly retarded recently, because the researchers have now approached to the scopes of this method. In this connection, the interest to the development of the devices based on nanowires, i.e., quasi-1-dimentional objects, have increased. Their surface to volume ratio is as high as in the case of nanopowders, obtained on the basis of spherical nanoparticles.

Nanowires were first synthesized at 1960s, but their wide application started only in the beginning of 21st century, when the technology advancement required the creation of a wide range of nanomaterials, and new methods of these materials treatment appeared. The basic method of nanowire synthesis was developed in details in classical work of R. Wagner and W. Ellis [153]. Recently, with the help of this method, SnO_2, In_2O_3, WO_3, ZnO and other oxides nanowires are obtained [154-158]. Liquid phase synthesis methods are also widely implemented [159-162].

The use of metal oxide nanowires as sensing elements of gas sensors continues in two directions. First direction supposes the use of a large quantity of nanowires. For example, nanowires can be grown on the surface of metal electrodes deposited on a dielectric substrate, wherein random electrical contact between wires located on different electrodes takes place. The contact of each pair of nanowires is not stable, but considering their large number, completely stable electrical contact is formed. Sensors based on such systems show high sensitivity [163-170]. Hierarchical structures with SnO_2 nanowires covered with additional nanoscale objects can be used for the improvement of electrical contact [164,169,170].

Second direction of nanowire sensors development is manufacturing of electrical contacts for individual nanowires. These contacts can be made by the means of photolithography, but more often focused ion beam (FIB) is used for this purpose. This approach has a number of advantages. First, a reliable electrical contact between nanowires and electrodes is secured. Second, the possibility for manufacturing of devices with ultralow energy consumption opens up.

In the case of the use of an individual nanowire, two pairs of electrodes are deposited onto the nanowire. Outer pair is used for the applying of heating electric potential, and inner pair is used for the measurement of electrical resistance. In spite of large number of works dedicated to the use of nanowires as conductometric gas sensors, they were not compared in details with classical semiconductor sensors manufactured by the means of sol-gel method.

1.3.2. Sensing layers obtained from nanopowder / sol materials

1.3.2.1. Influence of layer microstructure on the sensing performance

Metal oxide sensing films are divided into dense and porous [171, 172]. In dense films, the gas interaction takes place only at the surface of the film since the analyte cannot penetrate into the sensing film. In porous films, the gas can penetrate into the film and interact with the inner grains.

According to the definition of the International Union of Pure and Applied Chemistry (IUPAC) [172, 173], microporous materials have pore diameters of less than 2 nm, macroporous materials have pore diameter of greater than 50 nm; the mesoporous category thus lies in the middle. Mesoporous oxides with well-aligned pore structures can be prepared via many methods such as template synthesis [174–177], hydrothermal/solvothermal approaches [178–180], self-assembly reaction [181–185], the Kirkendall effect [186–188], Ostwald ripening [189, 190], the method of MWCNT templates [191]. Thick layers obtained by deposition of metal oxide nanopowders by drop-coating don't have well-aligned pore structures, but can be considered as mesoporous layers as well [192].

Xu et al. revealed that the sensor response to reducing gases (H_2 and CO) begins to increase sharply as the grain size of SnO_2 decreases to be smaller than a critical value (6 nm), which corresponds to twice the thickness of space charge layer (grain size effect) [193]. On the other hand, the effect of microstructure has been recognized [194–196]. Target gas diffuses into the sensing layer while it reacts with the surface oxygen of SnO_2 grains. If the rate of diffusion is too small compared with the rate of reaction, target gas cannot access the SnO_2 grains located in the inner region of the sensing body, leading to a loss in sensor response. Theory of gas-diffusion controlled sensitivity for thin film semiconductor gas sensor points out how to elaborate the sensing body to have microstructure favorable for gas diffusion and to improve the sensor response [194].

The grain size of SnO_2 in gas sensors usually ranges from a few nanometers to several tens of nanometersin mean diameter, so that the sensing body includes pores so called meso-pores (2–50 nm in radius) beside macro- and micro-pores. The gas transport through meso-pores is known to take place by Knudsen diffusion, the diffusion coefficient of which is given by

$$D_k = \frac{4r}{3}\sqrt{\frac{2RT}{\pi M}} \quad (1.15)$$

where D_k is gas diffusion constant, T is temperature, r pore radius, M is molecular weight of the diffusion gas, R is gas constant.

Gas molecules should interact with oxide grains, but at the same time they should diffuse inward through pores to access grains located inside. It is obvious that if the interaction is too strong, the molecules cannot reach the deep inside. This phenomenon has been analyzed for a thin film device well defined in grain size (D), pore radius (r) and film thickness (L) [197]. Sensor response of SnO_2 thin film devices to H_2S was enhanced by decreasing film thickness and by increasing SnO_2 grain size up to 16 nm.

The sols dispersing SnO_2 grains (crystallites) of an average size controlled in the range of 6–16 nm were prepared by hydrothermal method [192]. The SnO_2 grains remained monodispersed unless the time of hydrothermal treatment was prolonged too much. The magnitude of sensor response to H_2 in air tended to increase as the grain size of SnO_2 in the sols increased, suggesting the contribution by an increase in mesopore size. This phenomenon was considered [197] as consistent with a gas diffusion-reaction theory for semiconductor gas sensors [194, 198].

The gas diffusion rate is limited by the microstructure of the sensing layer and the size of the target gas molecules, while the surface reaction rate is dependent on the catalytic activity of the sensing layer and operating temperature [199]. Importantly, the rate leading to the steady state, where the diffusion and surface reaction are balanced, determines the response speed of gas sensors. Therefore, the gas diffusion and surface reaction are crucial parameters for semiconductor gas

sensors. Matsunaga et al. have simulated the sensitivity and response speed of resistive gas sensors by solving the following diffusion-reaction equation [200,201]:

$$\frac{\partial C(x,t)}{\partial t} = D\frac{\partial^2 C(x,t)}{\partial x^2} - kC(x,t) \quad (1.16)$$

where *C(x, t)* is the concentration of a target gas, *t* is the time, *x* is the distance (depth from the surface), *D* is the diffusion coefficient, and *k* is the rate constant. It was assumed that the diffusion and surface reaction follow the Knudsen mechanism and first-order kinetics, respectively. The simulated results showed that the response time of the sensors with 1 μm layer thickness SnO_2 to 1000 ppm H_2 should be as fast as 1 μs.

Real response and recovery properties of semiconductor gas sensors for H_2 and CO detection were studied using a high-speed gas-switching system, a low-dead volume chamber and a high-speed gas-switching valve [199]. Screen-printed SnO_2 layer had thickness 10 μm and was characterized with a mean pore size 37 nm; H_2 and CO concentration was 1000 ppm, operating temperature – 250 or 350^o C. Response time at 350 C was less than 0,5 s, while recovery time was more than 20 s. This incomplete recovery was attributed to the slow desorption of H_2O and CO_2 formed on SnO_2 by the surface reaction of H_2 and CO, respectively.

1.3.2.2. The role of contaminations of sensing material in gas sensing properties of metal oxide sensors

Selectivity and stability of MOX gas sensors are traditionally considered as main limitations for the use of gas sensors [202].

An approach consisting in synthesizing a very pure tin dioxide material with extremely low level of sodium, chlorine, and sulfur contamination was applied for improvement of long-term stability of the SnO_2-based gas sensors [203]. The influence of the impurities on crystallite growth rate during isothermal annealing at 700^{o}C, as well as the catalytic activity and surface composition of SnO_2 materials were investigated by means of comparison of extremely pure home-made SnO_2 and a commercial material. Intensive formation of Sn–OH groups on the surface of synthesized SnO2 particles was mentioned, what was explained by high density of surface defects due to low particle size of the material. Formation of numerous oxygen species in the range of 280–400 ◦C on material surface conditioned its high catalytic activity and caused high sensor signal values. Appearance of a new phase on the surface of commercial SnO_2 particles as a result of the thermal migration of impurities (Na and Cl ions) was discovered. It was found that crystallite growth causes signal decrease to propane by 1% during 590 h of operation for pure material and increase by 25% after 590 h in the case of high impurity concentration material. High drift value was explained by inhibition of propane oxidation process as a result of surface oxidation taking place with the participation of impurities.

The role of contamination with chlorides has been studied in the field of catalysis. For example, it is known that chlorine can replace OH groups on oxides' surface and upon calcination it causes dramatic grain growth, sintering and loss of porosity [204,205]. Chlorine has been reported many times as severe poison in oxidation of hydrocarbons [206–209] and CO [209,210]. Its inhibiting effect is related to formation of stable and less active oxychloride species ($Met_xO_yCl_z$) which

block the active surface sites and may produce chlorinated products competing with the reactants [206,207].

Water isotope (H_2O/D_2O) exchange in the presence of CO on two undoped tin dioxides in the presence of CO has been studied using modulation excitation diffuse reflectance infrared Fourier transform spectroscopy (DRIFTS) and resistance measurements [212]. Traces of Cl in SnO_2 materials with concentration of around 0.15 wt % induced dramatic changes in water adsorption kinetics and CO sensing mechanism. The material synthesized from Cl-free precursor manifested more basic surface hydroxyls with higher desorption rate of water. The material synthesized from tin tetrachloride (SnO_2Cl) manifested higher affinity to chemisorbed water than that made from tin hydroxide acetate (SnO_2Ac). Water desorption kinetics was found to be slower for SnO_2Cl by ca. 30% with respect to SnO_2Ac. High affinity to water as well as low sensor signals to CO in humid air reported for SnO_2Cl were proposed to originate from traces of Cl ions (about 0.15 wt % for SnO_2Cl and 0.03 wt % for SnO_2Ac) and not microstructure, which has been confirmed to be similar for both materials.

Influence of impurity level in SnO_2 materials on their CO and H_2 gas sensing properties was farther investigated [213] by comparison of SnO_2 materials synthesized by means of the same method from three different precursors. It was shown that the amount and nature of impurities, being rather technological, than fundamental issue, exert much more changes in the gas sensing properties than structural features of the sensing materials. The latter assumed high cross-sensitivity toward water vapor, which resulted in the lowest responses to CO and H_2 in humid air. Poor sensor performance is assumed to be due to slightly higher impurity level of the samples, analyzed by several standard methods. It was demonstrated that 300 ppmw Cl, K and Ca cause a dramatic increase of water vapor effects inundoped SnO_2 materials.

1.3.2.3. Mixed oxide materials sensing properties

Metal oxide nanodispersed materials doped with noble metals were studied in comparison with blank materials and with two-component nanodispersed oxide systems [214-217].

The effect of Pd doping on crystallite growth kinetics of highly pure nanocrystalline SnO_2 during isothermal annealing was studied [214]. Blank material demonstrated very low crystallite growth rate, while Pd doping resulted in remarkable increase of crystallite growth rate together with an increase in the activation energy. Simultaneous rise of activation energy and growth rate for doped materials demonstrated that the migration of energy barrier was notably lower for SnO_2–PdO system (resulting in high growth rate) and energy required for defect formation is much higher than that for blank SnO_2 (which explained increase of activation energy). In further study, crystallite growth and strain evolution during isothermal annealing of pure and Pd-doped SnO_2 has been compared and discussed regarding possible growth mechanisms; size and strain contributions to the peak broadening of in situ X-ray diffractograms were separated [215].

Sensing properties for two-component nanodispersed oxide systems: SnO_2–$MetO_x$ (Met = Ti, Zr, Hf, Y and La) and SnO_2–noble metals (Pd, Pt, Rh and their binary mixtures) were compared [216]. Cross-sensitivity tests towards H_2 in the presence of H_2O and towards H_2O in the presence of H_2 were performed. Doping with noble metals dramatically decreased SnO_2 selectivity towards H_2 in the presence of water vapors. SnO_2–Pd, SnO_2–Rh, SnO_2–Pd/Pt, SnO_2–Pd/Rh and SnO_2–Pt/Rh not only similarly interacted with H_2 and water in the same temperature range, but also manifested identical behavior during cross-sensitivity tests: “H_2 in water” and “water in H_2”. This fact was explained by interaction of H_2 and H_2O with the same surface species (such as surface oxygen). Blank SnO_2 and SnO_2–$MetO_x$ (especially SnO_2–TiO_2) demonstrated better selectivity. Doping with IIIB and IVB metal oxides led to remarkable change in hydroxylation degree of the materials (studied by FTIR

and TGA) and in the chemical activity of OH groups. Since surface hydroxyls are supposed to be inactive for direct water chemisorption, doping SnO_2 with IIIB and IVB metal oxides can be considered as a possible way for improvement of SnO_2-based sensors performance.

Wide-gap semiconductor oxides have been extensively investigated because of their wide range of technological applications, such as heterogeneous catalysis, photocatalysis, piezoelectricity, optoelectronics, photovoltaic conversion and gas sensing [217–223]. Novel electrical, mechanical, chemical and optical properties were obtained for nanodispersed wide-gap semiconductor oxides [224-228].

The interest to the wide-gap semiconductor oxides in gas sensing began after Seiyama et al. [228] evidenced their property of modifying electrical behaviour when interacting with ambient gases. Their detection properties are enhanced due to large specific surface offered and the influence in reducing the surface charge density [229–231]. When the particle dimensions scale down below a critical value, the phenomenon of the unpinning of Fermi level occurs [232]. The gas sensor performance is determined by the reception and transduction function [233] as well as by the fabrication procedure.

Mixed metal oxides and solid solutions demonstrate superior performance in comparison with single oxides [234–238]. Two oxides in $Ti_xSn_{1-x}O_2$ system show several similarities in structural as well as in electronic properties [239], so that they can easily form a solid solution. Moreover, they are wide-gap n-type semiconductors due to stoichiometric defects, mainly oxygen vacancies acting as electronic donor levels, although with energy positions more deep inside the band gap for TiO_2. In spite of similarity in their structural and electronic properties, they exhibit some peculiar differences, such as electrical transport properties and gas sensing behavior [223].

TiO_2–SnO_2 system has been widely investigated to determine the crystallographic properties, the phase diagram and to study the spinodal decomposition [240–243]. Conventionally, the solid solution $Ti_xSn_{1-x}O_2$ is obtained

from SnO_2 and TiO_2 via solid-state reaction, calcined at temperatures up to 1600 ºC, or high energy ball milling [244,245]. Recently, with the aim to use the TiO_2–SnO_2 as photocatalyst or as functional material in gas sensing, synthesis methods suitable to produce the functional material at nanometric scale (e.g. co-precipitation, molten salt method, sol–gel or thin film) have been adopted [246–250].

One of the properties of TiO_2–SnO_2 system widely tunable by varying the stoichiometry ($0 \leq x \leq 1$) of the synthesized powders is grain size dimension [251,252]. In [251] it was shown that $Ti_xSn_{1-x}O_2$ sensing films split into two broad behaviour tendencies: pure SnO_2 and a few solid solutions with a low *x* exhibit a SnO_2-like behaviour, while for $0.3 \leq x \leq 1$, a TiO_2-like one, the drastic change appearing in correspondence to x = 0.2, a borderline material between SnO_2 and TiO_2. Several measurements show this type of feature: among the electrical measurements, the shape of the Arrhenius plots, the conductance values, the shape of the energy barriers and the CO responses vs. temperature. However, the spectroscopic measurements especially highlight some differences between the two types of materials. This can be viewed for UV–Vis measurements [223] and for IR spectroscopy in [251].

Possible correlations between electrical and spectroscopical measurements were pointed out [223]. Nanosized $Ti_xSn_{1-x}O_2$ have been synthesized at various Ti:Sn molar ratio. Merging process of the two single oxides formed new compounds with improved gas responses compared to pure TiO_2 and also to pure SnO_2. Arrhenius plots for pure SnO_2 for mixed SnO_2-TiO_2 oxides in dry air and in 500 ppm of CO in dry air were reported. Two main observations were made: (i) in dry air, the conductance decreases increasing the titanium content in the solid solution up to three orders of magnitude; (ii) the shape of the Arrhenius plots changes as a minimum content of titanium is added to tin dioxide. Moreover, starting from 30% concentration of TiO_2 in SnO_2, shape and conductivity are identical for all the other compositions ($0.3 \leq x \leq 1$).

1.4. Mechanisms of gas sensing

1.4.1. Mechanisms of gas sensing with blank metal oxide materials

1.4.1.1. Adsorption on the surface of semiconductor

In traditional electroresistive type gas sensors the mechanism of gas sensitivity includes surface chemisorption processes, accompanied by the change of carrier concentration in semiconductor bulk. Sensor signal is formed as a result of the bulk change of electroconductivity of polycrystalline material. At the same time, the condition of intergrain contacts contributes substantively to the value of electroconductivity [254].

Adsorption of acceptor particles, i.e., having high electron affinity, for example, molecules (F_2, Cl_2, O_3, O_2, NO_x and other strong oxidizers), radicals (methyl, ethyl, etc.) atoms O, Cl etc. leads to outflow of electrons from the bulk of semiconductor, decreases n-type electroconductivity and increases electron work function. Response of a sensor detecting such particles is called acceptor response. Adsorption of acceptor particles on p-type semiconductor oxides increases their electroconductivity.

Concerning donor particles like hydrogen atoms, metal atoms, H_2 molecules, CO and other reducing agents, their adsorption at moderate and low temperatures (when notable diffusion of these atom inside the crystal is absent, and, consequently, there is no formation of substitutional atoms) is always accompanied by electroconductivity increase and decrease of work function for n-type semiconductor adsorbent and opposite action in the case of p-type semiconductor.

As a rule, oxides ofhighest valences are inclined to partial reduction, what leads to the appearance of oxygen vacancies in crystal lattice, forming n-type semiconductivity. Such are oxides TiO_2, V_2O_5, WO_3, SnO_2. Oxygen vacancies form donor levels in their case. Oxides of lowest oxidation states are inclined to partial

oxidation, appearance of over-stehiometric oxygen excess, formation of acceptor levels and p-type semiconductivity formation. Such are NiO, MnO, CoO, Cu_2O. Some oxides like Cr_2O_3, ZrO_2[255] and even ZnO [256] may show p- or n-type semiconductivity depending on the synthesis method and presence of additives.

Information about mechanisms of heterogeneous reactions is very important for the understanding of the nature of sensing action. By first half of 20^{th} century became apparent the necessity of the use of quantum-chemical conceptions for the solution of a number of the tasks of chemical physics, appearing during exploration of heterogeneous processes. Theoretical development of these ideas gained at the works of Volkenstein and Haufe [258].

The main idea of electronic adsorption theory is that a chemisorbed particle and a solid body represent an unite quantum-mechanical system. During analysis of such system, it is necessary to take into account the changes of electronic states of both adsorbent and adsorbate. According to this theory, there are three possible types of the bond between adsorbed particle and adsorbate surface: 1) “weak” bond, 2) “strong” acceptor bond, 3) “strong” donor bond. In the first case, an electron of the chemisorbed particle is attracted to a cation of the lattice, or an electron of a lattice anion is attracted to the chemisorbed particle, which stays electrically neutral. In the second case, an electron of a particle, adsorbed on a cation, interacts with a free electron of the semiconductor, realizing in that way chemical bond with the lattice. In the third case, an atom (or a molecule) adsorbs on a lattice anion and interacts with a free hole of the semiconductor.

Chemisorbed molecule forms new local energy levels in the band gap of the semiconductor. The formation of a “strong” acceptor bond corresponds to an electron transition to an acceptor level. The formation of a “strong” donor bond corresponds to an electron removal from donor level, i.e. hole transition to the donor level. So, due to particles adsorption, an excess of electrons or holes (i.e. surface charge) appears on the surface. The latter is compensated by appearance of a bulk charge in near-surface layer of the semiconductor, which is equal to the surface charge in value and opposite in sign. As a result, energy bands beside the surface are bended (figure 1.1). The calculation is usually made starting from vacuum energy (E_{vac}), being E_c the conduction-band bottom, E_v the valence band top (both are hatched) and between them, there are band gap and Fermi level (E_f).

It is supposed that in the absence of chemisorption, the surface is neutral (figure

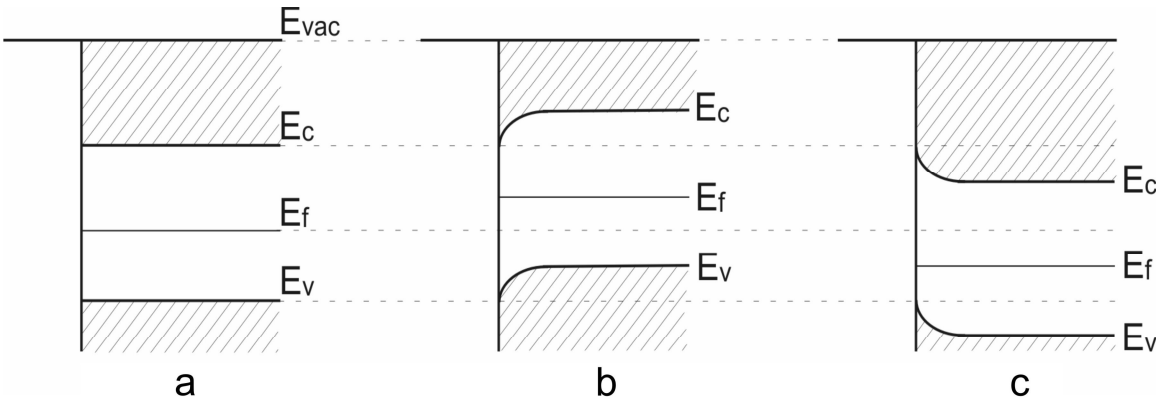

Figure 1.1. Bands bend on semiconductor surface:
a – neutral surface, b – positively charged, c – negatively charged

1.1. a). However, this supposition is not completely valid in the view of the presence of so-called “biographic” states on the surface, formed in consequence of surface atomsbonds cutting (Tamm levels). During chemisorption of donor particles, electrons pass into the bulk of the semiconductor, causing the surface to be charged positively (figure 1.1 b). During chemisorption of acceptor particles, the surface is charged negatively (figure 1.1. c). Near-surface layer thickness is characterized by Debye screening length. This layer is called space-charge region (SCR) [257].

The conclusion of electronic theory about the existence of both charged and neutral forms of chemisorption resolved the contradiction between observed rather high values of adsorption and the existence of “Weitz limit” which is evidence of existence of a very low (~1%) limit of surface filling by charged chemisorbed particles.

Chemisorption kinetics and surface charging kinetics might not coincide, what is related with recharge of biographic slow surface states, derived from chemisorption equilibrium [258].

As a rule, practical tasks of ambient monitoring are related with particles detection not in vacuum, but in air. Therefore it is necessary to take into account that the surface of semiconductor sensor contains significant amount of chemisorbed oxygen in these conditions.

Character of metal oxides interaction with oxygen is determined by temperature conditions. At temperatures from –200 to 100 ^{o}C takes place physisorption, while from 0 to 450 ^{o}C various types of chemisorption can be observed. At higher temperatures, chemical interaction with semiconductor material may take place and lead to the appearance of surface (400-600 ^{o}C) and bulk (1200-1500 ^{o}C) defects [253].

There are various forms of chemisorbed oxygen. At the temperature range of 80-150 ^{o}C, the molecule is reduced to molecular anion O_2^-. At temperature ranges of 150-260 ^{o}C, further reduction leads to appearance of oxygen anions O^-, and at the temperature ranges of 260-460 ^{o}C appear anions O^{2-}. Thus, chemical interaction of reducing molecules (CO, H_2, CH_4) with chemisorbed oxygen is more probable than their independent adsorption on the surface of semiconductor.

1.4.1.2. Debye length and grain size influence on SMOX material conductance

Electroconductivity in semiconductor films is determined by ratio between film crystallites size (diameter W), contact region (diameter of contacting regions – bridges d_b) and space-charge region size X_d. As a result of oxygen chemisorption in the film, depleted surface layer (X_d) is formed on the borders of the crystallites, by electrical charge, captured on the surface of the crystallite. Potential barrier is formed in the place of the contact of two crystallites. Potential barrier which is characterized by height ϕ_b and depleted region size X_d, is related with Debye screening length L_d:

$$\varphi_b = \frac{q \cdot N_{ss}^2}{8\varepsilon\varepsilon_0 \cdot n_0}, \quad (1.17)$$

$$L_d = \sqrt{\frac{\varepsilon\varepsilon_0 \cdot kT}{q^2 \cdot n_0}}, \quad (1.18)$$

$$X_d = L_d \sqrt{\frac{2q \cdot |\varphi_b|}{kT}}, \quad (1.19)$$

where N_{ss} is density of charged surface states on the border of crystallite, calculated in accordance with Fermi-Dirac distribution, n_0 is electrons concentration in non-depleted region, q is electron charge, T – temperature, ε_0, ε – dielectric permittivity of vacuum and the semiconductor.

Depending on the ratio of W, d_b and X_d, there are three possible models of film electroconductivity [1, 193].

1.4.1.3. Models of electroconductivity in metal oxide sensing layers

1.4.1.3.1. "Thin neck" or "open bridges" model ($2X_d<d_b$)

Thickness of space-charge regions (grey color on figures 1.5-1.7) is smaller than the diameter of the contact between crystallites (figure 1.5). Since SCR resistance is much higher that semiconductor bulk resistance, all the current passing through the bridge is concentrated in its central, electrically neutral part. Change of surface states charge on the border of the crystal due to adsorption leads to the change of SCR size (X_d) and, consequently, to the change of effective cross-section of the bridge. Bridge resistance change leads, accordingly, to the film resistance change.

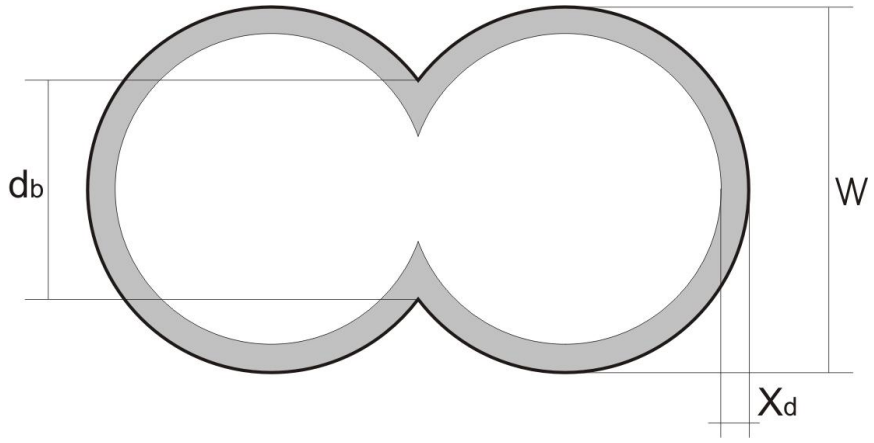

Fig. 1.5. "Thin neck" model

1.4.1.3.2. "Grain-boundary", or "closed bridges" model ($d_b<2X_d<W$).

In this model (figure 1.6) the thickness of space-charge regions are smaller than the diameter of crystallite, but greater than the diameter of the bridges between

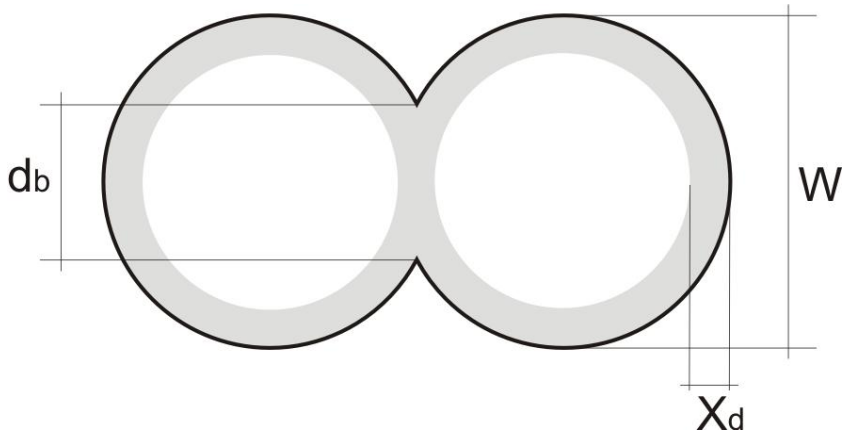

Figure 1.6. "Grain-boundary" model

crystallites [193]. In this case, space-charge regions cover all the volume of the bridges, what leads to the formation of a potential barrier for electrons in the regions of crystallite contacts. Therefore, only electrons with the energy sufficient to overcome the barrier participate in conductivity current. The decrease of the surface charge due to the adsorption of donor particles leads to the lowering of this barrier and, consequently, to the increase of the number of electrons that are able to overpass the barrier. This process causes the changes in conductivity of the film.

Energetical model of interface between crystallites in the absence of potential difference is presented in figure 1.7 a, while in the figure 1.7. b is presented the

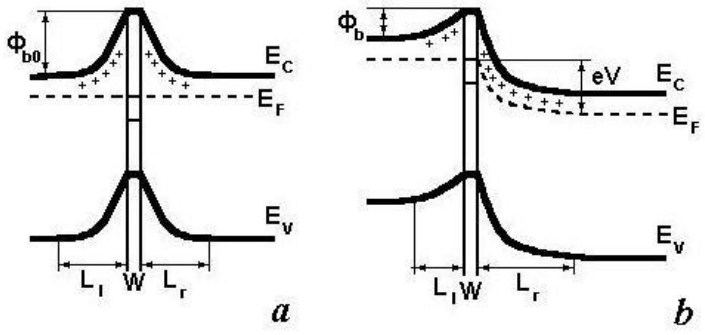

Figure 1.7.Energetical model of interface between crystallites

model when a bias – potential difference V is introduced. The height of potential barriers φ_{b0} and the thickness of depleted regions L_i and L_r between crystallites in this case is determined by the concentration of electrons in crystallites and by the charge of the traps located in the intercrystallite region.

It is possible to point out three basic mechanisms of electrons passing through barriers: thermal electron emission, tunneling and the recombination on traps. Predominance of one mechanism or another is determined by the height of the potential barrier and the thickness of the corresponding region. As it can be seen from Figure 1.7.b, the applied bias changes the density of charged traps, and consequently, also changes the height of the barriers, what is reflected in the nonlinearity of current-voltage characteristic.

1.4.1.3.3. Model of full modulation of the resistance of crystallite bulk (X_d>W).

According to this model (Figure 1.8), space-charge region covers all the crystallite volume [256]. Charge modulation on the border of crystallite changes the position of Fermi level due to adsorption and leads to the modulation of electrones inside the crystallite, what causes the change of sensor conductivity.

This model corresponds to the films with very high dispersivity, for example, obtained by reactive sputtering. It is possible to represent the structure of such films as a net with individual crystallites located in its knots. Conductivity of the knots has two states: conducting and nonconducting. A charge change on a crystal border (for

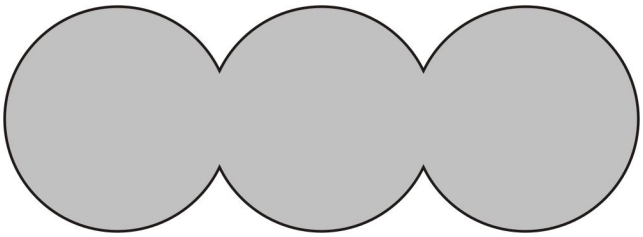

Figure 1.8. Model of full modulation of crystallite bulk resistance

examole, due to the injection of a reducing gas) leads to switching of some crystallytes from nonconducting to conducting state. Thus, the chains of conducting crystallites are formed. When a bias is applied to this structure, current passes by the chains connecting electrical contacts. Adsorption processes changes heights of potential barriers on crystallite borders, what may lead to the change of the current path. This effect is determined in literature with the term of percollation.

In real films, depending on the method of their production, temperature and gas ambient, different mechanisms of electroconductivity might be realized in different parts of the film.

1.4.2. Models of gas sensing with metal doped MOx films

1.4.2.1. Electron theory of gas sensing

According to the electron theory, it is supposed that catalytic activity of a semiconductor is determined by surface concentration of charged chemisorbed particles, which, in its turn, is determined by Fermi level. Thus, displacing Fermi levels, (for example, adding special dopants in semiconductor), it is possible to change its catalytic activity. As ascertained in subsequent, in addition to Fermi level, significant impact on catalytic activity and chemisorption makes the spectra of biographic states, what particularly affects samples with developed surface [260].

Interaction of an adsorbate with surface of a semiconductor sensor doped with metals (Pt, Pd and others), may run by two different mechanisms. First of them (electron sensitizing) includes gas adsorption on a metal particle, where also takes place interaction of the particle with oxygen and desorption of products of their interaction (figure 1.9 a). There is electron exchange between metal particle and semiconductor bulk.

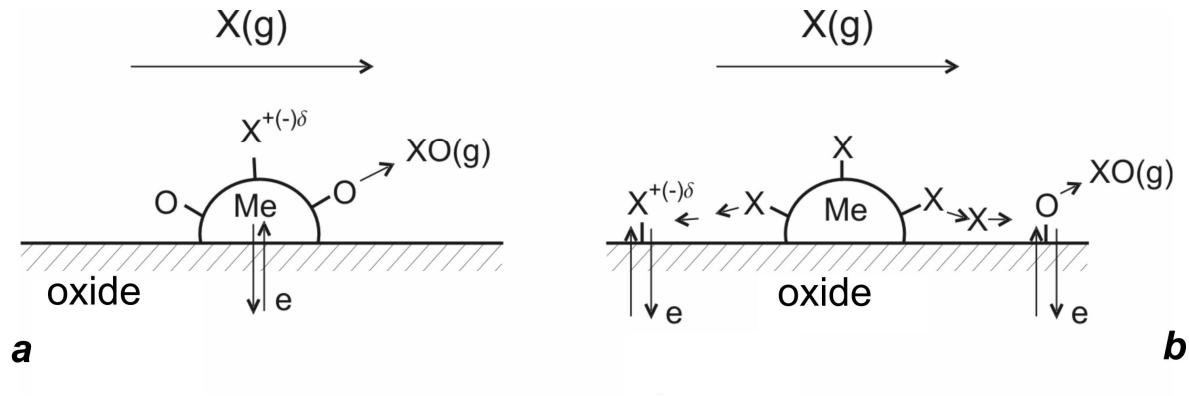

Figure 1.9. Possible mechanisms of metal particles influence on adsorption change of electrophysical characteristics of adsorbent:
a – electron sensitizing: the role of dopants is to be acceptors or donors of electrones, depending on the ambient;
b – chemical sensitizing: the role of dopants is activation and spillover of reactants.

Second mechanism (chemical sensitizing) includes dissociative adsorption of molecular gases (like hydrogen and oxygen) on the surface of metallic catalysts like palladium and platinum, and flow (spillover) of dissociation products on the surface of the semiconductor (figure 1.9. b). Following chemisorption of the products in charged form, or their participation in reactions with other chemisorbed particles and electrically active surface defects, caused by high chemical activity of the products, leads to sharper change of electroconductivity in comparison with the changes caused by adsorption of corresponding molecular gases. Electron exchange between metal particle and semiconductor bulk takes place [261-264].

1.4.2.2. H_2 sensing mechanism in MOx semiconductor nanofilm doped with noble metal

Gas sensing mechanism in different forms of metal oxide such as thin film, thick film, and powder form have been studied using a wide variety of techniques [268-276].

In [268] it was used conduction-AFM method which can simultaneously provide information onboth local electrical properties and surface morphology. Hydrogen gas response mechanism of Pd nanoparticles decorated TiO_2 nanofilm was observed. It was shown that there are two gas sensing mechanisms taking place when hydrogen interacts with sensing material in air atmosphere: chemical and electronic sensitization of the nanofilm. Initial electrical conduction change takes place without any structural modification (chemical sensitization), thereafter the sensing happens due to formation of Pd hydride (electronic sensitization) evidenced by the structural change of Pd nanoparticles.

Chemical sensitization due to the Pd nanoparticles results in hydrogen gas molecules dissociation into active hydrogen species (such as H*, H+, and other forms) [278]. These hydrogen species diffuse to the TiO_2 film and react with the chemisorbed oxygen to form volatile water molecules, or/and remove the oxygen

adsorbents chemisorbed on Pd [279]. Both of these reactions return the space-charge layer electrons (i.e., trapped electrons) to the bulk and lead to an increase in the electrical conduction. However, electrical conduction can increase even without having the role from oxygen adsorbents. The nanofilm film placed in an inert ambient responds with increasing conduction upon exposure to 1000 ppm of hydrogen gas. This suggests that hydrogen must contribute more to conduction increase in addition to reacting with chemisorbed oxygen.

Electronic sensitization (lowering of nano-Schottky barrier height). Hydrogen can dissolve in Pd. This results into a decreased Pd work function and, in turn, can further lower the nano-Schottky potential barrier height [280]. During the N_2 /H_2 cycling, this electronic sensitizationwas demonstrated to be the major mechanism leading to electrical conduction change. Since there are no prior oxygen adsorbents, single slope response kinetics is observed, suggesting that only the electronic sensitization mechanism plays the major role in the depletion of the space-charge layer [268]. In contrast, the presence of oxygen adsorbents can give a dual slope hydrogen response kinetics, with initial slope region corresponding to chemical sensitization and latter one to the electronic sensitization [281].

Both sensing layer local conductivity and topography change in “live” regime were observed using C-AFM technique [268]. At the very beginning of hydrogen input it was observed a sharp change of conductivity from non-conductive state to conductive. Starting from the third minute to minute 10 it was observed the increase of Pd particles mean size form ~8.5 to ~13 nm. The effect of Pd particles increase due to Pd hydride formation is known and used in Pdmesowire based hydrogen gas sensors [283, 284].

1.4.2.3. Bulk doping influence on the response of conductometric SnO_2 gas sensors

At present, while considering gas sensing properties of metal oxides, the cluster model is used predominantly [285]. In the frame of this model, catalytically active additives present on the metal oxide surface are in the cluster state. However, the presence of clusters, which could be well observable during a scanning electron microscopy (SEM) and a transmission electron microscopy (TEM), does not mean yet that clusters determine sensors operation [285].

The degree of crystallinity is important for gas sensing performance of metal oxides since its influence on the stability of material structure and its temporal and thermal sensing characteristics. Small amounts (0.1–0.2 wt%) of Pd and Pt promote the improvement of crystal structure of the material unlike higher concentrations of the dopants. Furthermore, such doping can decrease the concentration of defect centers, because the presence of Pt and Pd stimulates oxygen dissociation, what may lead to an improvement of stoichiometry of the SnO_2 grains [286-288].

In the case of higher concentrations of Pd and Pd dopants in SnO_2 materials, sensor sensitivity drops as a result of an increase of the concentration of structural defects. High level of the SnO_2 structure disordering, caused by doping, may be the reason of the increase of surface statesconcentration, pinning the surface Fermi level and limiting the Fermi level shift during interaction with gas surrounding [289, 290]. The presence of correlation between doping and the surface state density was experimentally confirmed in [288, 295, 296].

The appearance of structurally disturbed surface layer in the grains of heavily doped SnO_2 also corresponds to the assumption about decrease of SnO_2 lattice stability due to its doping with high metal concentrations. High resolution transmission electron microscopy (HRTEM) images of the SnO_2:Pd (8 wt%) grains presented in [297] show that highly doped SnO_2 grains consist of a well-crystallized core covered with an amorphous layer of tin oxide.

Current transport across an intergrain interface, which is mainly affected by the barrier heights, can also be strongly modified in the presence of defect states in the band gap not only by modifying the potential distribution [294], but also by adding additional transport paths across potential barrier [298,299]. The increase of structural defects concentration at the interface can strongly decrease the role of potential barrier changing, caused by the surface reactions, in modulation of current transport in metal oxide-based gas sensors.

According to [300] and [301], sensor response maximum for undoped $SnO_2$is being achieved after annealing at $T_{an}\sim$ 650–800^oC. An increase in calcination temperature higher than 400–500 ^oC results in improvement of the SnO_2 crystallinity and disappearance of the lattice distortion. The increase of sensor response of undoped SnO_2 after annealing in temperature range from 400 to 650–800◦C, coinciding with the improvement of the SnO_2 crystallinity, takes place despite of the grain size increase.

At bulk doping the sensitivity drop is being observed already at temperatures, exceeding 400◦C, as for instance for SnO_2:Pd, while sensitivity maximum for a surface modified samples was observed at the same temperatures (800◦C), as for undoped samples [303]. This means that bulk doping and associated defect formation are determinative factors in this process. It was shown [304] that during bulk doping takes place incorporation of dopants into the SnO_2 lattice at the place of tin. According to [305], $(Pd, Pt)^{4+}$ concentrations can be interpreted as concentrations of noble metals incorporated in the tin dioxide lattice, because only ions of Pd and Pt such as $(Pd, Pt)^{4+}$ have sizes, allowing incorporation in the SnO_2 lattice instead of tin.

The exceeding annealing temperature of 450–500◦C, which correspond to achieving maximum sensor response, leads to the appearance of metallic Pd and Pt and forming Pd and Pt clusters.

Authors [285] conclude from the results of [296, 306, 307] that the increase of the sensor response is consistent with the Pt and Pd incorporation in the SnO_2

lattice, while the drop of sensor response coincides with the appearance of the Pd and Pt inclusions in the matrix of SnO_2, i.e. clusters. So, the optimal concentration of doping additives should be close to a limiting solubility of noble metals in SnO_2. At concentration lower than limiting solubility concentration of surface atoms of noble metals which form active surface sites is insufficiently high. At bigger concentration, besides appearance of metal clusters, structural disordering of a surface area of the metal oxide grains is being sharply increased. The appearance of metal clusters takes place in the samples with high concentration of doping additives (3 wt%). At the same time in the samples with low concentration (0.2 wt%), which are characterized by maximum sensor response, palladium, presented in an oxidized state, is finely dispersed and doesn't form any clusters [307]. This means that the role of noble metals such as Pt and Pd in gas sensing effect is more complex than anticipated according to the cluster model of metal doping.

References Chapter 1

[1] J. Maier, Physical Chemistry of Ionic Materials, Wiley, 2004, 526 p.

[2] K. Zakrzewska, Mixed oxides as gas sensors, Thin Solid Films, 391 (2001) 229-238.

[3] Y. Yoshida, S. Tokashiki, K. Kubota, R. Shiratuchi, Y. Yamaguchi, M. Kono, S. Hayase, Increase in photovoltaic performances of dye-sensitized solar cells—Modification of interface between TiO_2 nano-porous layers and F-doped SnO_2 layers, Solar Energy Materials and Solar Cells, 92 (2008) 646-650.

[4] M. Batzill, U. Diebold, The surface and materials science of tin oxide, Progress in Surface Science, 79 (2005) 47-154.

[5] U. Diebold, The surface science of titanium dioxide, Surface Science Reports, 48 (2003) 53-229.

[6] M. Park, T.E. Mitchell, A.H. Heuer, Subsolidus Equilibria in the TiO_2-SnO_2 System, Journal of the American Ceramic Society, 58 (1975) 43-47.

[7] P.R. Bueno, E.R. Leite, L.O.S. Bulhões, E. Longo, C.O. Paiva-Santos, Sintering and mass transport features of (Sn,Ti)O_2 polycrystalline ceramics, Journal of the European Ceramic Society, 23 (2003) 887-896.

[8] R.G. Palgrave, A. Bourlange, D.J. Payne, J. S. Foord, R.G. Egdell, Interfacial Diffusion during Growth of SnO_2 (110) on TiO_2 (110) by Oxygen Plasma Assisted Molecular Beam Epitaxy, Crystal Growth & Design, 9 (2009) 1793-1797.

[9] M. Ramamoorthy, D. Vanderbilt, and R. King-Smith, Phys. Rev. B 49 (1994) 16721

[10] M. Lazzeri, A. Vittadini, A. Selloni. Structure and energetics of stoichiometric TiO_2 anatase surfaces Phys. Rev. B 63, 155409 (2001)

[11] H. Zhang, J.F. Banfield, J. Phys. Chem. B 104 (2000) 3481 - 3487.

[12] M.R. Ranade, A. Navrotsky, H.Z. Zhang, J.F. Banfield, S.H. Elder, A. Zaban, P.H. Borse, S.K. Kulkarni, G.S. Doran, H.J. Whitfield, Proc. Nat. Acad. Sciences 99 (2002) 6476 - 6481.

[13] V. Shklover, M.K. Nazeeruddin, S.M. Zakeeruddin, C. Barbe, A. Kay, T. Haibach, W. Steurer, R. Hermann, H.U. Nissen, M. Grätzel, Chem. Mater. 9 (1997) 430 - 439.

[14] S.D. Burnside, V. Shklover, C. Barbe, P. Comte, F. Arendse, K. Brooks, M. Grätzel, Chem. Mater. 10 (1998) 2419 – 2425

[15] S.B. Jenkins. Nanoporous materials: types, properties, and uses. Nova Science Publishers, 2010.

[16] P.I. Gouma, P.K. Dutta and M.J. Mills. Structural stability of titania thin films. NanoStructured Materials, Vol. 11, No. 8, pp. 1231–1237, 1999

[17] A. A. Gribb, J. F. Banfield. Particle size effects on transformation kinetics and phase stability in nanocrystalline TiO_2. Am. Mineral. 82, 717 (1997).

[18] Soumen Das, V. Jayaraman. SnO_2: A comprehensive review on structures and gas sensors. Progress in Materials Science 66 (2014) 112–255.

[19] Eranna G., Joshi B.C., Runthala D.P., Gupta R.P. Oxide materials for development of integrated gas sensors – A comprehensive review. // Crit. Rev. Solid State Mater. Sci., 2004, v. 29, p. 111-188.

[20] Yoshimura M., Livage J. Soft Processing for Advanced Inorganic Materials. // MRS Bulletin, 2000, v. 25, N9, p. 12-13.

[21] Cao G, Wang Y. Nanostructures materials, synthesis, properties and applications, 2nd ed., vol. 2. New Jersey, USA: World Scientific Publishing Co. Pte. Ltd.; 2011.

[22] J. P. Jolivet, Metal Oxide Chemistry and Synthesis: From Solution to Solid State, J. Wiley and Sons, Chichester, 2000.

[23] A. Pottier, S. Cassaignon, C. Chaneac, F. Villain, E. Tronc, J.-P. Jolivet. Size tailoring of TiO_2 anatase nanoparticles in aqueous medium and synthesis of nanocomposites. Characterization by Raman spectroscopy. J. Mater. Chem., 2003, 13, 877–882.

[24] J.-P. Jolivet, C. Froidefond, A. Pottier, C. Chaneac, S. Cassaignon, E. Tronc, P. Euzen. Size tailoring of oxide nanoparticles by precipitation in aqueous medium. A semi-quantitative modeling. J. Mater. Chem., 2004 , 14 , 3281 – 3288.

[25] E. Matijevic, Langmuir, 1986, 2, 12.

[26] A. Pottier, C. Chaneac, E. Tronc, L. Mazerolles and J. P. Jolivet, J. Mater. Chem., 2001, 11, 1116.

[27] Berge P, Dubois M. Experimental confirmation of the Kawasaki-Einstein-Stokes formula; measurement of small correlation lengths. Phys Rev Lett 1971; 27:1125.

[28] Murray CB, Kagan CR, Bawendi MG. Synthesis and characterization of monodisperse nanocrystals and close-packed nanocrystal assemblies. Annu Rev Mater Sci 2000;30:545.

[29] Jiang Y. Forced hydrolysis and chemical co-precipitation in hand-book of nanophase and nanostructured materials. New York: Kluwer Academic; 2003.

[30] Peng X., Wickham J., Alivisatos A.P. Kinetics of II-VI and III-V colloidal semiconductor nanocrystal growth: focusing of size distributions. J Am Chem Soc 1998;120:5343.

[31] Wulff G. On the question of the rate of growth and dissolution of crystal surfaces. Z Kristallogr Mineral 1901; 34:449.

[32] Whitehead T.H. The complex compound theory of colloidal oxides. // Chem. Rev., 1937, v. 21, p. 113-128.

[33] Rollinson C.L. Olation and related chemical properties. / In The Chemistry of Coordination Compounds. New York: Reinhold Publ. Co., 1956, p. 448-471.

[34] Scott E.S., Andrieth L.F. Inorganic Polymerization Reactions. // J. Chem. Educ., 1954, v. 31, p. 168-175.

[35] Burmistrov V. A. *Gidratirovannye oksidy IV i V grupp*. Moscow, Nauka, 1986 160 pp.

[36] Dubinin V. N. Kordyuk S. L. Lisichenko V. I. *Issledovanie kinetiki olovyannyh kislot s pomoshhyu effekta Messbauera*. Teoreticheskaya i eksperimentalnaya himiya, 1966, vol. 2, pp. 130-131.

[37] Dzisko V. A. Karnauhov A. P. Tarasova D. V. *Fiziko-himicheskie osnovy sinteza okisnyh katalizatorov*. Novosibirsk, Nauka, 1978, 384 pp.

[38] Chen F.L., Liu M.L. Preparation of mesoporous tin oxide for electrochemical applications. // Chem. Commun., 1999, N 18, p. 1829-1830.

[39] Vlagappan N., Rao C.N.R. Mesoporous phases based on SnO_2 and TiO_2. // Chem. Commun., 1996, N 14, p. 1685-1686.

[40] Qi L., Ma J., Cheng M., Zhao Z. Synthesis and Characterization of Mesostructured Tin Oxide with Crystalline Walls. // Langmuir, 1998, v. 14, p. 2579-2581.

[41] Severin K.G., Abdel-Fattah T.M. Pinnavaia T.J. Supramolecular assembly of mesostructured tin oxide. // Chem. Commun., 1998, N 14, p. 1471-1472.

[42] Yang P.D., Zhao D.Y., Margolese D.I., Chmelka B.F, Stucky G.D. Block Copolymer Templating Syntheses of Mesoporous Metal Oxides with Large Ordering Lengths and Semicrystalline Framework. // Chem. Mater., 1999, v. 11, p. 2813-2826.

[43] Zhou S., Lu S., Ke Ya., Li J. Synthesis of mesostructured tin oxide with neutral surfactant as a template in aqueous media. // Mater. Lett., 2003, v. 57, p. 2679–2681.

[44] Rumyantseva M.N., Gaskov A.M., Rosman N., Pagnier T., Morante J.R. Raman surface vibration modes in nanocrystalline SnO_2 prepared by wet chemical methods: correlations with the gas sensors performances. // Chem. Mater., 2005, v. 17, p. 893-901.

[45] Sergent N., Gelin P., Perier-Camby L., Praliaud H., Thomas G. Preparation and characterisation of high surface area stannic oxides: structural, textural and semiconducting properties. // Sens. Actuators B, 2002, v. 84, p. 176-188.

[46] Wang Yu.D., Ma Ch.L., Sun X.D., Li H.D. Synthesis of mesostructured SnO_2 with CTAB and hydrous tin chloride. // Mater. Lett., 2001, v. 51, p. 285-288.

[47] Kim J.H., Sung J.S., Son J.S., Vasiliev A.A., Malyshev V.V., Koltypin E.A., Eryshkin A.V., Godovski D.Yu., Pisliakov A.V., Yakimov S.S.// Sensors and Actuators.2007.B 44.P.452.

[48] Wang Y.D., Ma C.L., Sun X.D., Li H.D. Synthesis of mesostructured SnO_2 with CTAB and hydrous tin chloride. // Mater. Lett., 2001, v. 51, p. 285-288.

[49] M.C. Carotta, A. Fioravanti, S. Gherardi, C. Malagù, M. Sacerdoti, G. Ghiotti, S. Morandi. (Ti,Sn) solid solutions as functional materials for gas sensing. Sens. Actuat. B 194 (2014) 195– 205.

[50] S. Barth, F. Hernandez-Ramirez, J. D. Holmes, A. Romano-Rodriguez. Synthesis and applications of one-dimensional semiconductors. Pr. Mat Sc 55 (2010) 563–627.

[51] Weisbuch C, Vinter B. Quantum semiconductor structures: fundamentals and applications. Boston: Academic Press; 1991.

[52] Hayden, O., R. Agarwal, and C. M. Lieber, "Nanoscale avalanche photodiodes for highly sensitive and spatially resolved photon detection," Nat. Mater., Vol. 5, 352-356, 2006.

[53] Z. Zhang, J. Y. Ying, M. S. Dresselhaus, Bismtuh quantum-wire arrays fabricated by a vacuum melting and pressure injection process. J. Mater. Res. 13 1998 1745–1748 .

[54] Ohnishi,H.; Kondo,Y; Takayanagi,K. Quantized conductance through individual rows of suspended gold atoms, Nature,395,6704,1998,780-7833.

[55] Xianping Chena, Cell K.Y. Wong, Cadmus A. Yuanc, Guoqi Zhang. Nanowire-based gas sensors. Sensors and Actuators B 177 (2013) 178– 195.

[56] Y. Cui, C.M. Lieber, Functional nanoscale electronic devices assembled using silicon nanowire building blocks, Science 291 (2001) 851.

[57] M.S. Gudiksen, L.J. Lauhon, J. Wang, D.C. Smith, C.M. Lieber, Growth of nanowire superlattice structures for nanoscale photonics and electronics, Nature 415 (2002) 617–620.

[58] Y. Huang, X. Duan, Y. Cui, L.J. Lauhon, K.H. Kim, C.M. Lieber, Logic gates and computation from assembled nanowire building blocks, Science 294 (2001) 1313.

[59] S. Jin, D. Whang, M.C. McAlpine, R.S. Friedman, Y. Wu, C.M. Lieber, Scalable interconnection and integration of nanowire devices without registration, Nano Letters 4 (2004) 915–919.

[60] A.M. Morales, C.M. Lieber, A laser ablation method for the synthesis of crystalline semiconductor nanowires, Science 279 (1998) 208.

[61] Z. Zhong, D. Wang, Y. Cui, M.W. Bockrath, C.M. Lieber, Nanowire crossbar arrays as address decoders for integrated nanosystems, Science 302 (2003) 1377.

[62] S. Banerjee, A. Dan, D. Chakravorty, Review synthesis of conducting nanowires, Journal of Materials Science 37 (2002) 4261–4271.

[63] M.T. Björk, C. Thelander, A.E. Hansen, L.E. Jensen, M.W. Larsson, L.R. Wallenberg, L. Samuelson, Few-electron quantum dots in nanowires, Nano Letters 4 (2004) 1621–1625.

[64] Y. Cui, Q. Wei, H. Park, C.M. Lieber, Nanowire nanosensors for highly sensitive and selective detection of biological and chemical species, Science 293 (2001) 1289.

[65] A.B. Greytak, L.J. Lauhon, M.S. Gudiksen, C.M. Lieber, Growth and transport properties of complementary germanium nanowire field-effect transistors, Applied Physics Letters 84 (2004) 4176.

[66] F. Patolsky, C.M. Lieber, Nanowire nanosensors, Materials Today 8 (2005) 20–28.

[67] Y. Wu, J. Xiang, C. Yang, W. Lu, C.M. Lieber, Single-crystal metallic nanowires and metal/semiconductor nanowire heterostructures, Nature 430 (2004) 61–65.

[68] F. Gu, L. Zhang, X. Yin, L. Tong, Polymer single-nanowire optical sensors, Nano Letters 8 (2008) 2757–2761.

[69] X. Xue, Y. Chen, Y. Liu, S. Shi, Y. Wang, T. Wang, Synthesis and ethanol sensing properties of indium-doped tin oxide nanowires, Applied Physics Letters 88 (2006) 201907.

[70] Yushi Hu, Hyunjoong Lee, Suhwan Kim, Minhee Yun. A highly selective chemical sensor array based on nanowire/nanostructure for gas identification. Sensors and Actuators B: Chemical Volume 181, May 2013, Pages 424–431

[71] D. Reefman, E. Cantatore, Power management options for AMI applications, in: S. Mukherjee, E. Arts, R. Roovers, F. Widdershoven, M. Ouwerkerk (Eds.), AmIware Hardware Technology Drivers of Ambient Intelligence, Springer, Dordrecht, 2006, pp. 285–313.

[72] S. Xu, Y. Qin, C. Xu, Y. Wei, R. Yang, Z.L. Wang, Self-powered nanowire devices, Nature Nanotechnology 5 (2010) 366–373.

[73] L. Tien, H. Wang, B. Kang, F. Ren, P. Sadik, D. Norton, S. Pearton, J. Lin, Room-temperature hydrogen-selective sensing using single Pt-coated ZnO nanowires at microwatt power levels, Electrochemical and Solid-State Letters 8 (2005) G230.

[74] Y. Dan, S. Evoy, A. Johnson, Chemical Gas Sensors Based on Nanowires, 2008, Arxiv preprint: arXiv:0804.4828.

[75] D. Mijatovic, J. Eijkel, A. Van Den Berg, Technologies for nanofluidic systems: top-down vs. bottom-up—a review, Lab on a Chip 5 (2005) 492–500.

[76] G. Shen, P.C. Chen, K. Ryu, C. Zhou, Devices and chemical sensing applications of metal oxide nanowires, Journal of Materials Chemistry 19 (2009) 828–839.

[77] P. Yang, R. Yan, M. Fardy, Semiconductor nanowire: what's next? Nano Letters 10 (2010) 1529–1536.

[78] M. Yaman, T. Khudiyev, E. Ozgur, M. Kanik, O. Aktas, E.O. Ozgur, H. Deniz, E. Korkut, M. Bayindir, Arrays of indefinitely long uniform nanowires and nanotubes, Nature Materials 10 (2011) 494–501.

[79] J. Osuwa, P. Anusionwu, Some advances and prospects in nanotechnology: a review, Asian Journal of Information Technology 10 (2011) 96–100.

[80] A. Wolfsteller, N. Geyer, T.K. Nguyen-Duc, P. Das Kanungo, N. Zakharov, M. Reiche, W. Erfurth, H. Blumtritt, S. Kalem, P. Werner, Comparison of the top-down and bottom-up approach to fabricate nanowire-based silicon/germanium heterostructures, Thin Solid Films 518 (2010) 2555–2561.

[81] J.H. Kim, M. Seo, S.Y. Kim, Lithographically patterned breath figure of photoresponsive small molecules: dual-patterned honeycomb lines from a combination of bottom-up and top-down lithography, Advanced Materials 21 (2009) 4130–4133.

[82] A. Javey, S.W. Nam, R.S. Friedman, H. Yan, C.M. Lieber, Layer-by-layer assembly of nanowires for three-dimensional, multifunctional electronics, Nano Letters 7 (2007) 773–777.

[83] M.C. McAlpine, R.S. Friedman, S. Jin, K. Lin, W.U. Wang, C.M. Lieber, High-performance nanowire electronics and photonics on glass and plastic substrates, Nano Letters 3 (2003) 1531–1535.

[84] B.P. Timko, T. Cohen-Karni, G. Yu, Q. Qing, B. Tian, C.M. Lieber, Electrical recording from hearts with flexible nanowire device arrays, Nano Letters 9 (2009) 914–918.

[85] C.G. Levins, C.E. Schafmeister, The synthesis of curved and linear structures from a minimal set of monomers, The Journal of Organic Chemistry 70 (2005) 9002–9008.

[86] K. Ariga, J.P. Hill, M.V. Lee, A. Vinu, R. Charvet, S. Acharya, Challenges and breakthroughs in recent research on self-assembly, Science and Technology of Advanced Materials 9 (2008) 014109.

[87] K.H. Smith, E. Tejeda-Montes, M. Poch, A. Mata, Integrating top-down and self-assembly in the fabrication of peptide and protein-based biomedical materials, Chemical Society Reviews 40 (2011) 4563–4577.

[88] P.A. Maury, D.N. Reinhoudt, J. Huskens, Assembly of nanoparticles on patterned surfaces by noncovalent interactions, Current Opinion in Colloids & Interface Science 13 (2008) 74–80.

[89] Y. Cui, M.T. Björk, J.A. Liddle, C. Sönnichsen, B. Boussert, A.P. Alivisatos, Integration of colloidal nanocrystals into lithographically patterned devices, Nano Letters 4 (2004) 1093–1098.

[90] J. Huskens, Patterned 2D and 3D assemblies of nanoparticles on molecular print boards, Advances in Science and Technology 51 (2006) 105–114.

[91] Z. Fan, J.C. Ho, Z.A. Jacobson, H. Razavi, A. Javey, Large-scale, heterogeneous integration of nanowire arrays for image sensor circuitry, Proceedings of the National Academy of Sciences of the United States of America 105 (2008) 11066.

[92] L. Cao, J.S. White, J.S. Park, J.A. Schuller, B.M. Clemens, M.L. Brongersma, Engineering light absorption in semiconductor nanowire devices, Nature Materials 8 (2009) 643–647.

[93] E. Comini. Metal oxide nanowires chemical sensor: present status and future challenges. Transducers 2013, Barcelona, SPAIN, 16-20 June 2013.

[94] Lionel Vayssieres, Niclas Beermann, Sten-Eric Lindquist, and Anders Hagfeldt. Controlled Aqueous Chemical Growth of Oriented Three-Dimensional Crystalline Nanorod Arrays: Application to Iron(III) Oxides. Chem Mater 2001;13:233–5.

[95] B. Gates, B. Mayers, B. Cattle and Y. Xia. Synthesis and Characterization of Uniform Nanowires of Trigonal Selenium.

[96] B. Gates, B. Mayers, A. Grossman and Y. Xia. A Sonochemical Approach to the Synthesis of Crystalline Selenium Nanowires in Solutions and on Solid Supports. Adv Mater 2002;14:1749–52.

[97] Victor F. Puntes, Kannan M. Krishnan, and A. Paul Alivisatos. Colloidal Nanocrystal Shape and Size Control: The Case of Cobalt. Science 16 March 2001: 2115-2117.

[98] Z.R. Dai, Z.W. Pan and Z.L. Wang. Novel Nanostructures of Functional Oxides Synthesized by Thermal Evaporation. 2003; 13:1, 9–24.

[99] Z. L. Wang, X. Y. Kong, and J. M. Zuo. Induced Growth of Asymmetric Nanocantilever Arrays on Polar Surfaces. Phys. Rev. Lett. 91, 185502 (2003) – Published 30 October 2003.

[100] William L. Hughes and Zhong L. Wang . Formation of Piezoelectric Single-Crystal Nanorings and Nanobows. Am Chem Soc 2004;126:6703–9.

[101] R. S. Wagner and W. C. Ellis. Vapor-liquid-solid mechanism of single crystal growth. Appl. Phys. Lett. 4, 89 (1964).

[102] E. Comini , C. Baratto , I. Concina , G. Faglia , M. Falasconi , M. Ferroni , V. Galstyan, E. Gobbi, A. Ponzoni, A. Vomiero, D. Zappa, V. Sberveglieri, G. Sberveglieri. Metal oxide nanoscience and nanotechnology for chemical sensors. Sensors and Actuators B 179 (2013) 3–20.

[103] Javier Bonal. Strategy and activities of the Microsystems and Nanosystems Unit. Common Strategic Framework for EU research and innovation funding. Eurosensors XXV. Athens, Greece, 2011.

[104] D. Briand, F. Molina-Lopez, A. V. Quintero, C. Ataman, J. Courbat, N. F. de Rooij. Why Going Towards Plastic and Flexible Sensors? Eurosensors XXV. Procedia Engineering, Volume 25, 2011, Pages 8–15.

[105] G. Müller, S. Beer, S. Paul, A. Helwig. Novel Chemical Sensor Applications in Commercial Aircraft. Eurosensors XXV. Procedia Engineering. Volume 25, 2011, Pages 16–22.

[106] S.M. Roper, S.H. Davis, S.A. Norris, A.A. Golovin, P.W. Voorhees, M. Weiss, Steady growth of nanowires via the vapor–liquid–solid method, Journal of Applied Physics 102 (2007) 034304.

[107] K.W. Kolasinski, Catalytic growth of nanowires: vapor–liquid–solid, vapor–solid–solid, solution–liquid–solid and solid–liquid–solid growth, Current Opinion in Solid State and Materials Science 10 (2006) 182–191.

[108] E. Givargizov, Fundamental aspects of VLS growth, Journal of Crystal Growth 31 (1975) 20–30.

[109] Trentler TJ, Hickman KM, Goel SC, Viano AM, Gibbons PC, Buhro WE. Science 1995;270:1791–17914.

[110] Holmes JD, Johnston KP, Doty RC, Korgel BA. Science 2000;207:1471–3.

[111] Sun JW, Buhro WE. Angew Chem Int Ed 2008;47:3215–8.

[112] Zhao LL, Yosef M, Steinhart M, Goring P, Hofmeister H, Gosele U, et al. Angew Chem Int Ed 2006;45:311–5.

[113] Brumlik CJ, Martin CR. J Am Chem Soc 1991;113:3174–5.

[114] Zheng MJ, Zhang LD, Li GH, Shen WZ. Chem Phys Lett 2002;363:123–8.

[115] Martin CR, Nishizawa M, Jirage K, Kang M. J Phys Chem B 2001;105:1925–34.

[116] Yu SF, Li NC, Wharton J, Martin CR. Nano Lett 2003;3:815–8.

[117] Bachmann J, Jing J, Knez M, Barth S, Shen H, Mathur S, et al. J Am Chem Soc 2007;129:9554–5.

[118] Zhang Z, Gekhtman D, Dresselhaus MS, Ying JY. Chem Mater 1999;11:1659–65.

[119] Erts D, Polyakov B, Daly B, Morris MA, Ellingboe S, Boland J, et al. J Phys Chem B 2006;110:820–6.

[120] Redmond G, Bein T, Morris MA, Holmes JD. Chem Phys Chem 2007;8:235–40.

[121] Lew KK, Redwing JM. J Cryst Growth 2003;254:14–22.

[122] Bogart TE, Dey S, Lew KK, Mohney SE, Redwing JM. Adv Mater 2005;17:114–7.

[123] Petkov N, Birjukovs P, Phelan R, Morris MA, Erts D, Holmes JD. Chem Mater 2008;20:1902–8.

[124] Zhang Y, Dai HJ. Appl Phys Lett 2000;77:3015–7.

[125] Fan HJ, Knez M, Scholz R, Nielsch K, Pippel E, Hesse D, et al. Nat Mater 200;5:627–31.

[126] Filankembo A, Pileni MP. J Phys Chem B 2000;104:5865–8.

[127] Tanori J, Pileni MP. Adv Mater 1995;7:862–4.

[128] Pileni MP. Nat Mater 2003;2:145–50.

[129] Li D, Xia YN. Nano Lett 2003;3:555–60.

[130] Bashouti M, Salalha W, Brumer M, Zussman E, Lifshitz E. Chem Phys Chem 2006;7:102–6.

[131] Edelstein AS, Cammarata RC. Nanomaterials: synthesis, properties and applications. 2nd ed. Institute of Physics Publishing; 1998.

[132] Sun YG, Khang DY, Hua F, Hurley K, Nuzzo RG, Rogers JA. Adv Funct Mater 2005;15:30–40.

[133] Sun Y, Rogers JA. Nano Lett 2004;4:1953–9.

[134] Mathur S, Barth S, Shen H, Pyun JC, Werner U. Small 2005;1:713–7.

[135] Mathur S, Barth S. Small 2007;3:2070–5.

[136] Ma YJ, Zhou F, Lu L, Zhang Z. Solid State Commun 2004;130:313–6.

[137] Lou SH, Fan JY, Liu WL, Zhang M, Song ZT, Lin CL, et al. Nanotechnology 2006;17:1695–9.

[138] Lilach Y, Zhang JP, Moskovits M, Kolmakov A. Nano Lett 2005;5:2019–22.

[139] Arbiol J, Comini E, Faglia G, Sbeveglieri G, Morante JR. J Cryst Growth 2008;310:253–60.

[140] Dai ZR, Gole JL, Stout JD, Wang ZL. J Phys Chem B 2002;106:1274–9.

[141] Calestani D, Zha M, Zappettini A, Lazzarini L, Salviati G, Zanotti L, et al. Mater Sci Eng C 2005;25:625–30.

[142] Liu ZQ, Zhang DH, Han S, Li C, Tang T, Jin W, et al. Adv Mater 2003;15:1754–7.

[143] Hu JQ, Bando Y, Liu QL, Golberg D. Adv Funct Mater 2003;13:493–6.

[144] Wang B, Yang YH, Wang CX, Yang GW. J Appl Phys 2005;98:073520.

[145] Nguyen P, Ng HT, Kong J, Cassel AM, Quinn R, Li J, et al. Nano Lett 2003;3:925–8.

[146] Zheng MJ, Li GH, Zhang XY, Huang SY, Lei Y, Zhang LD. Chem Mater 2001;13:3859–61.

[147] Kolmakov A, Zhang Y, Cheng G, Moskovits M. Adv Mater 2003;15:997–1000.

[148] Wang Y, Aponte M, Leon N, Ramos I, Furlan R, Pinto N, et al. J Am Ceram Soc 2005;88:2059–63.

[149] Wang Y, Aponte M, Leon N, Ramos I, Furlan R, Evoy S, et al. J Semicond Sci Technol 2004;19:1057–60.

[150] Zhang Y, He X, Li J, Miao Z, Huang F. Sens Actuators B 2008;132:67–73.

[151] Eranna G., Joshi B.C., Runthala D.P., Gupta R.P. Oxide materials for development of integrated gas sensors – A comprehensive review. // Crit. Rev. Solid State Mater. Sci., 2004, v. 29, p. 111-188.

[152] Martinelli G., Carotta M.C., Traversa E., Ghiotti G. Thick-film gas sensors based on nano-sized semiconducting oxide powders. // Mater. Res. Soc. Bull., 1999, v. 24, N6, p. 30-36.

[153] R.S. Wagner, W.C. Ellis, Vapor–liquid–solid mechanism of single crystal growth, Applied Physics Letters 4 (1964) 89–90.

[154] G. Sberveglieri, G. Faglia, S. Groppelli, P. Nelli, A. Camanzi, A new technique for growing large surface-area SnO2 thin-film (RGTO technique), Semiconductor Science And Technology 5 (1990) 1231–1233.

[155] G. Faglia, E. Comini, A. Cristalli, G. Sberveglieri, L. Dori, Very low power consumption micromachined CO sensors, Sensors and Actuators B 55 (1999) 140–146.

[156] C. Garzella, E. Comini, E. Bontempi, L.E. Depero, C. Frigeri, G. Sberveglieri, Sol–gel TiO2 and W/TiO2 nanostructured thin films for control of drunken driving, Sensors and Actuators B 83 (2002) 230–237.

[157] E. Comini, G. Sberveglieri, V. Guidi, Ti–W–O sputtered thin film as n or p type gas sensors, Sensors and Actuators B 70 (2000) 108–114.

[158] E. Comini, G. Faglia, G. Sberveglieri, CO and NO2 response of tin oxide silicon doped thin films, Sensors and Actuators B 76 (2001) 270–274.

[159] N. Yamazoe, New approaches for improving semiconductor gas sensors, Sensors and Actuators B 5 (1991) 7.

[160] C.E. Morosanu, in: G. Siddall (Ed.), Thin Films by Chemical Vapour Deposition, vol. 7, Elsevier, Amsterdam/Oxford/New York/Tokyo, 1990, p. 373 (Chapter 12).

[161] R.F. Bunshah, in: R.F. Bunshah (Ed.), Deposition Technologies for Films and Coatings, Noyes Publications, Park Ridge, 1982, p. 1 (Chapter 1).

[162] D.M. Mattox, Handbook of Physical Vapor Deposition (PVD) Processing, Noyes Publications, Westwood, 1998, p. 444 (Chapter 9).

[163] L.C. Klein, in: L.C. Klein (Ed.), Sol–Gel Technology for Thin Films, Fibres, Performs, Electronics and Specialty Shapes, Noyes Publications, Park Ridge, 1988, p. 50 (Chapter 2).

[164] E. Comini, L. Ottini, G. Faglia, G. Sberveglieri, SnO2 RGTO UV activation for CO monitoring, IEEE Sensors Journal 4 (2004) 17–20.

[165] E. Comini, G. Faglia, G. Sberveglieri, Z.W. Pan, Z.L. Wang, Stable and highly sensitive gas sensors based on semiconducting oxide nanobelts, Applied Physics Letters 81 (2002) 1869–1871.

[166] Z.L. Wang, Characterizing the structure and properties of individual wire-like nanoentities, Advanced Materials 12 (2000) 1295.

[167] J.D. Prades, R. Jimenez-Diaz, F. Hernandez-Ramirez, S. Barth, A. Cirera, A. Romano-Rodriguez, S. Mathur, J.R. Morante, Ultralow power consumption gas sensors based on self-heated individual nanowires, Applied Physics Letters 93 (2008) 12.

[168] A. Kolmakov, Some recent trends in the fabrication, functionalisation and characterisation of metal oxide nanowire gas sensors, International Journal of Nanotechnology 5 (2008) 450–474.

[169] A.M. Haghiri-Gosnet, C. Vieu, G. Simon, M. Mejıas, F. Carcenac, H. Launois, Nanofabrication at a 10 nm length scale: limits of lift-off and electroplating transfer processes, Journal of Physics IV (9 (Pr 2)) (1999) 133–141.

[170] C.R.K Marrian, D.M. Tennant, Nanofabrication, Journal of Vacuum Science and Technology A 21 (2003) S207–S215.

[171] Barsan, N.; Weimar, U. Conduction model of metal oxide gas sensors. J. Electroceram. 2001, 7, 143-167.

[172] Yu-Feng Sun, Shao-Bo Liu, Fan-Li Meng, Jin-Yun Liu, Zhen Jin, Ling-Tao Kong, Jin-Huai Liu. Metal Oxide Nanostructures and Their Gas Sensing Properties: A Review. Sensors 2012, 12, 2610-2631

[173] Rouquerol, J.; Avnir, D.; Fairbridge, C.W.; Everett, D.H.; Haynes, J.H.; Pernicone, N.; Ramsay, J.D.F.; Sing, K.S.W.; Unger, K.K. Recommendations for the characterization of porous solids. Pure Appl. Chem. 1994, 66, 1739-1758.

[174] Antochshuk, V.; Jaroniec, M.; Joo, S.H.; Ryoo, R. Mesoporous materials for heavy metal ion adsorption synthesized by displacement of polymeric template. Stud. Surf. Sci. Catal. 2002, 141, 607-614.

[175] Ma, Z.J.; Zhu, Y.M.; Li, Y.J.; Fang, X. Research on preparation of mesoporous zeolite by template method. Adv. Mater. Res. Switz. 2011, 158, 204-210.

[176] Luo, L.T.; Wang, J.X.; Zhao, X. Template synthesis and characterization of mesoporous CeO2 and Ru-loaded mesoporous CeO2. Indian J. Chem. A 2009, 48, 327-332.

[177] Kim, H.; Cho, J. Hard templating synthesis of mesoporous and nanowire SnO2 lithium battery anode materials. J. Mater. Chem. 2008, 18, 771-775.

[178] Liu, S.Y.; Meng, X.J.; Xiao, F.S. Hydrothermal synthesis of ordered mesoporous materials with high stability at high temperatures. Acta Phys. Chim. Sin. 2010, 26, 1852-1859.

[179] Hu, H.M.; Deng, C.H.; Sun, M.; Zhang, K.H.; Yang, M.D. Solvothermal preparation and characterization of sheet-like CuInSe2 with hierarchically mesoporous structures. Mater. Lett. 2011, 65, 617-620.

[180] Fujihara, S.; Maeda, T.; Ohgi, H.; Hosono, E.; Imai, H.; Kim, S.H. Hydrothermal routes to prepare nanocrystalline mesoporous SnO2 having high thermal stability. Langmuir 2004, 20, 6476-6481.

[181] Hyodo, T.; Nishida, N.; Shimizu, Y.; Egashira, M. Preparation and gas-sensing properties of thermally stable mesoporous SnO2. Sens. Actuat. B 2002, 83, 209-215.

[182] Luca, V.; Hook, J.M. Study of the structure and mechanism of formation through self-assembly of mesostructured vanadium oxide. Chem. Mater. 1997, 9, 2731-2744.

[183] Mitra, A.; Bhaumik, A.; Paul, B.K. Synthesis and characterization of mesoporous titanium dioxide using self-assembly of sodium dodecyl sulfate and benzyl alcohol systems as templates. Micropor. Mesopor. Mater. 2008, 109, 66-72.

[184] Yin, J.S.; Wang, Z.L. Template-assisted self-assembly and cobalt doping of ordered mesoporous titania nanostructures. Adv. Mater. 1999, 11, 469-472.

[185] Hyodo, T.; Abe, S.; Shimizu, Y.; Egashira, M. Gas-sensing properties of ordered mesoporous SnO2 and effects of coatings thereof. Sens. Actuat. B 2003, 93, 590-600.

[186] Yin, Y.D.; Rioux, R.M.; Erdonmez, C.K.; Hughes, S.; Somorjai, G.A.; Alivisatos, A.P. Formation of hollow nanocrystals through the nanoscale Kirkendall Effect. Science 2004, 304, 711-714.

[187] Fan, H.J.; Gosele, U.; Zacharias, M. Formation of nanotubes and hollow nanoparticles based on Kirkendall and diffusion processes: A review. Small 2007, 3, 1660-1671.

[188] Liu, B.; Zeng, H.C. Fabrication of ZnO “dandelions” via a modified kirkendall process. J. Am. Chem. Soc. 2004, 126, 16744-16746.

[189] Yang, H.G.; Zeng, H.C. Preparation of hollow anatase TiO2 nanospheres via Ostwald ripening. J. Phys. Chem. B 2004, 108, 3492-3495.

[190] Jia, B.P.; Gao, L. Morphological transformation of Fe3O4 spherical aggregates from solid to hollow and their self-assembly under an external magnetic field. J. Phys. Chem. C 2008, 112, 666-671.

[191] Li, H.H.; Meng, F.L.; Sun, Y.F.; Liu, J.Y.; Wan, Y.T.; Sun, B; Liu, J.H. Mesoporous SnO_2 sensor prepared by carbon nanotubes as template and its sensing properties to indoor air pollutants. Procedia Eng. 2010, 7, 172-178.

[192] D. D. Vuong, G. Sakai, K. Shimanoe, N. Yamazoe. Preparation of grain size-controlled tin oxide sols by hydrothermal treatment for thin film sensor application. Sens. Actuat. B 103 (2004) 386–391.

[193] C. Xu, J. Tamaki, N. Miura, N. Yamazoe, Grain size effects on gas sensitivity of porous SnO_2-based elements, Sens. Actuators B 3 (1991) 147–155.

[194] G. Sakai, N. Matsunaga, K. Shimanoe, N. Yamazoe, Theory of gas-diffusion controlled sensitivity for thin film semiconductor gas sensor, Sens. Actuators B 80 (2001) 125–131.

[195] A. Dieguez, A. Romano-Rodriguez, J.R. Morante, U. Weimar, M. Schweizer-Berberich, W. Göpel, Morphological analysis of nanocrystalline SnO_2 for gas sensor applications, Sens. Actuators B 31 (1996) 1–8.

[196] T. Maekawa, K. Suzuki, T. Takada, T. Kobayashi, M. Egashira, Odor identification using a SnO_2-based sensor array, Sens. Actuators B 80 (2001) 51–58.

[197] Vuong, D.D.; Sakai, G.; Shimanoe, K.; Yamazoe, N. Hydrogen sulfide gas sensing properties of thin films derived from SnO2 sols different in grain size. Sens. Actuat. B 2005, 105, 437-442.

[198] Matsunaga, N.; Sakai, G.; Shimanoe, K.; Yamazoe, N. Formulation of gas diffusion dynamics for thin film semiconductor gas sensor based on simple reaction-diffusion equation. Sens. Actuat. B 2003, 96, 226-233.

[199] T. Kida, T. Kuroiwa, M. Yuasa, K. Shimanoe, N. Yamazoe. Study on the response and recovery properties of semiconductor gas sensors using a high-speed gas-switching system. Sens. Actuat. B 134 (2008) 928–933.

[200] N. Matsunaga, G. Sakai, K. Shimanoe, N. Yamazoe, Formulation of gas diffusion dynamics for thin film semiconductor gas sensor based on simple reaction–diffusion equation, Sens. Actuators B: Chem. 96 (2003) 226– 233.

[201] N. Matsunaga, G. Sakai, K. Shimanoe, N. Yamazoe, Diffusion equation-based study of thin film semiconductor gas sensor-response transient, Sens. Actuators B: Chem. 83 (2002) 216–221.

[202] C. Pijolat, B. Riviere, M. Kamionka, J. P. Viricelle, P. Breuil. Tin dioxide gas sensor as a tool for atmospheric pollution monitoring: Problems and possibilities for improvements. J. Mater. Sci. 38 (2003) 4333 – 4346.

[203] R.G. Pavelko, A.A. Vasiliev, E. Llobet, X. Vilanova, N. Barrabés, F. Medinab, V.G. Sevastyanov. Comparative study of nanocrystalline SnO_2 materials for gas sensor application: Thermal stability and catalytic activity. Sens. Actuat. B 137 (2009) 637–643

[204] A.G. Shastri, A. Datye, J. Schwank, Influence of chlorine on the surface area and morphology of TiO2, Appl. Catal. 14 (1985) 119–131.

[205] A. Khaleel, M. Nawaz, B. Hindawi, Sol–gel derived Cr(III) and Cu(II)/γ-Al2O3doped solids: Effect of the dopant precursor nature on the structural, textural and morphological properties, Mater. Res. Bull. 48 (2013) 1709–1715.

[206] D.O. Simone, T. Kennelly, Reversible poisoning of palladium catalysts formethane oxidation, Appl. Catal. 70 (1991) 87–100.

[207] P. Gélin, M. Primet, Complete oxidation of methane at low temperature overnoble metal based catalysts: a review, Appl. Catal. B: Environ. 39 (2002) 1–37.

[208] N.W. Cant, D.E. Angove, M.J. Patterson, The effects of residual chlorine on thebehaviour of platinum group metals for oxidation of different hydrocarbons,Catal. Today 44 (1998) 93–99.

[209] W. Lin, Y. Zhu, N. Wu, Y. Xie, I. Murwani, E. Kemnitz, Total oxidation of methane at low temperature over Pd/TiO2/Al2O3: effects of the support and residual chlorine ions, Appl. Catal. B: Environ. 50 (2004) 59–66.

[210] D.I. Kondarides, X.E. Verykios, Effect of chlorine on the chemisorptive properties of Rh/CeO_2 catalysts studied by XPS and temperature programmed desorption techniques, J. Catal. 174 (1998) 52–64.

[211] J.M. Soares, M. Hall, M. Cristofolini, M. Bowker, The role of impurities on thelow temperature CO oxidation on Au/TiO2, Catal. Lett. 109 (2006) 103–108.

[212] R.G. Pavelko, J.-K. Choi, A. Urakawa, M. Yuasa, T. Kida, K. Shimanoe, H2O/D2O exchange on SnO_2 materials in the presence of CO: operando spectroscopic and electric resistance measurements, J. Phys. Chem. C 118 (2014) 2554–2563.

[213] R.G. Pavelko, M. Yuasa, T. Kida, K. Shimanoe, N. Yamazoe. Impurity level in SnO2 materials and its impact on gas sensing properties. Sens. Actuat. B 210 (2015) 719–725

[214] R.G. Pavelko, A.A. Vasiliev, F. Gispert-Guirado, N. Barrabes, J. Llorca, E. Llobet, V.G. Sevastyanov. Crystallite growth kinetics of highly pure nanocrystalline tin dioxide: The effect of palladium doping. Materials Chemistry and Physics 121 (2010) 267–273.

[215] R.G. Pavelko, F. Gispert-Guirado, E. Llobet. Parametric line profile analysis for in situ XRD of SnO2 materials: Separation of size and strain contributions. Solid State Ionics 255 (2014) 21–29.

[216] R.G. Pavelko, A.A. Vasiliev, E. Llobet, V.G. Sevastyanov, N.T. Kuznetsov. Selectivity problem of SnO_2 based materials in the presence of water vapors. Sens. Actuat. B 170 (2012) 51– 59.

[217] G. Martinelli, M.C. Carotta, E. Traversa, G. Ghiotti, Thick-film gas sensors based on nano-sized semiconducting oxide powders, MRS Bull. 24 (6) (1999) 30–36.

[218] M. Batzill, U. Diebold, Surface studies of gas sensing metal oxides, Phys. Chem. Chem. Phys. 9 (2007) 2307–2318.

[219] S. Rehman, R. Ullah, A.M. Butt, N.D. Gohar, Strategies of making TiO2 and ZnO visible light active, J. Hazard. Mater. 170 (2009) 560–569.

[220] M. Law, L.E. Greene, J.C. Johnson, R. Saykally, P. Yang, Nanowire dye-sensitized solar cells, Nat. Mater. 4 (2005) 455–459.

[221] A. Zecchina, D. Scarano, S. Bordiga, G. Spoto, Surface structures of oxides and halides and their relationships to catalytic properties 46 (2001) 265–397.

[222] J.G. Lu, P. Chang, Z. Fan, Quasi-one-dimensional metal oxide materials – synthesis, properties and applications, Materials Science and Engineering R 52 (2006) 49–91.

[223] M.C. Carotta, A. Fioravanti, S. Gherardi, C. Malagù, M. Sacerdoti, G. Ghiotti, S. Morandi. (Ti,Sn) solid solutions as functional materials for gas sensing. Sens. Actuat. B 194 (2014) 195– 205.

[224] J. Wang, X.W. Sun, Z. Jiao, Application of nanostructures in electrochromic materials and devices: recent progress, Materials 3 (2010) 5029–5053.

[225] F. Zaera, Nanostructured materials for applications in heterogeneous catalysis, Chem. Soc. Rev. 42 (7) (2013) 2746–2762.

[226] P. Moriarty, Nanostructured materials, Rep. Prog. Phys. 64 (2001) 297–381.

[227] G. Di Francia, B. Alfano, V. La Ferrara, Conductometric gas nanosensors, J. Sens. (2009), 659275.

[228] T. Seiyama, A. Kato, K. Fulishi, M. Nagatani, A new detector for gaseous components using semiconductive thin films, Anal. Chem. 34 (1962) 1502–1503.

[229] C. Xu, J. Tamaki, N. Miura, N. Yamazoe, Grain size effects on gas sensitivity of porous SnO2-based elements, Sens. Actuators B 3 (1991) 147–155.

[230] X.-J. Huang, Y.-K. Choi, Chemical sensors based on nanostructured materials, Sens. Actuators B 122 (2007) 659–671.

[231] K.J. Choi, H.W. Jang, One-dimensional oxide nanostructures as gas-sensing materials: review and issues, Sensors 10 (2010) 4083–4099.

[232] C. Malagù, V. Guidi, M.C. Carotta, G. Martinelli, Unpinning of Fermi level in nanocrystalline semiconductors, Appl. Phys. Lett. 84 (2004) 4158–4160.

[233] N. Yamazoe, K. Shimanoe, Receptor function and response of semiconductor gas sensor, J. Sens. (2009), 875704.

[234] V. Dusastre, D.E. Williams, Gas-sensitive resistor properties of the solid solution series Tix(Sn1−ySby)1−xO2 (0 < x < 1, y = 0, 0.01, 0.05), J. Mater. Chem. 9 (1999) 445–450.

[235] K. Zakrzewska, Mixed oxides as gas sensors, Thin Solid Films 391 (2001) 229–238.

[236] M.C. Carotta, M. Benetti, V. Guidi, S. Gherardi, C. Malagu', B. Vendemiati, G. Martinelli, Nanostructured (Sn,Ti,Nb)O2 solid solution for hydrogen sensing, Mater. Res. Soc. Symp. Proc. 915 (2006) R07–R10.

[237] M.B. Gawande, R.K. Pandeyb, R.V. Jayaram, Role of mixed metal oxides in catalysis science versatile applications in organic synthesis, Catal. Sci. Technol. 2 (2012) 1113–1125.

[238] M. Radecka, A. Kusior, A. Lacz, A. Trenczek-Zajac, B. Lyson-Sypien, K. Zakrzewska, Nanocrystalline TiO2/SnO2 composites for gas sensors, J. Therm. Anal. Calorim. 108 (2012) 1079–1084.

[239] J.R. Sambrano, L.A. Vasconcellos, J.B.L. Martins, M.R.C. Santos, E. Longoc, A. Beltran, A theoretical analysis on electronic structure of the (1 1 0) surface of TiO2–SnO2 mixed oxide, J. Mol. Struct. 629 (2003) 307–314.

[240] M. Park, T.E. Mitchell, H. Heuer, Subsolidus equilibria in the SnO2–TiO2 system, J. Am. Ceram. Soc. 58 (1) (1975) 43–47.

[241] T.C. Yuan, A.V. Virkar, Kinetics of spinodal decomposition in the TiO2–SnO2 system: the effect of aliovalent dopants, J. Am. Ceram. Soc. 71 (1) (1988) 12–21.

[242] H.P. Naidu, A.V. Virkar, Low-temperature TiO2–SnO2 phase diagram using the molten-salt method, J. Am. Ceram. Soc. 81 (1998) 2176–2180.

[243] T. Hirata, Oxygen position, octahedral distortion, and bond-valence parameter from bond lengths in Ti1−xSnxO2 (0 < x < 1), J. Am. Ceram. Soc. 83 (2000) 3205–3207.

[244] T. Hirata, K. Ishioka, M. Kitajima, H. Doi, Concentration dependence of optical phonons in the TiO2–SnO2 system, Phys. Rev. B 53 (1996) 8442–8448.

[245] P.R. Bueno, E.R. Leite, L.O.S. Bulhões, E. Longo, C.O. Paiva-Santos, Sintering and mass transport features of (Sn,Ti)O2 polycrystalline ceramics, J. Eur. Ceram. Soc. 23 (2003) 887–896.

[246] M.M. Oliveira, D.C. Schnitzler, A.J.G. Zarbin, (Ti,Sn)O2 mixed oxides nanoparticles obtained by the sol–gel route, Chem. Mater. 15 (2003) 1903–1909.

[247] M. Hirano, T. Kono, Synthesis of rutile-type TiO2–SnO2 solid solution nanoparticles by forced Co-hydrolysis under hydrothermal conditions, Mater. Sci. Eng. 18 (2011) 062015.

[248] H. Tiana, J. Ma, X. Huang, L. Xie, Z. Zhao, J. Zhou, P. Wu, J. Dai, Y. Hu, Z. Zhu, H. Wang, H. Chen, Nano-sized coupled photocatalyst (Sn0.25,Ti0.75)O2 powders synthesized by a low temperature molten salt method, Mater. Lett. 59 (2005) 3059–3061.

[249] A.Q. Wu, X.Z. Fang, X.H. Lin, H.Q. Wang, Y.X. Wang, R. Zhang, L.S. Gao, Synthesis and oxygen sensing properties of Ti1−xSnxO2 solid solutions nanoparticles, Key Eng. Mater. 575–576 (2014) 45–49.

[250] K. Zakrzewska, M. Radecka, TiO2–SnO2 system for gas sensing – photodegradation of organic contaminants, Thin Solid Films 515 (2007) 8332–8338.

[251] M.C. Carotta, S. Gherardi, V. Guidi, C. Malagù, G. Martinelli, B. Vendemiati, M. Sacerdoti, G. Ghiotti, S. Morandi, Electrical and spectroscopic properties of Ti0.2Sn0.8O2 solid solution for gas sensing, Thin Solid Films 517 (2009) 6176–6183.

[252] M.C. Carotta, A. Cervi, S. Gherardi, V. Guidi, C. Malagù, G. Martinelli, B. Vendemiati, M. Sacerdoti, G. Ghiotti, S. Morandi, S. Lettieri, P. Maddalena, A. Setaro, (Ti, Sn)O2 solid solutions for gas sensing: a systematic approach by different

techniques for different calcination temperature and molar composition, Sens. Actuators B 139 (2009) 329–339.

[253] Chemical Sensors and Biosensors, B. R. Eggins, John Wiley & Sons, 2002

[254] Chemical Sensors , R. W. Cattrall , Oxford Uni. Press, Oxford, 1997

[255] Chemical Sensor Technology, Vol. 1,2,3,4, Elsevier, Amsterdam 1988-1992

[256] N. Vorobyeva, M. Rumyantseva, E. Konstantinova, D. Grishina, A. Gaskov. Inversion of NH3 Sensor Signal and Paramagnetic Centers of Nanocrystalline ZnO (Ga). Eurosensors 2011

[257] O.V. Kiselev, O.F. Krylov. Electronic Phenomena in Adsorption Catalysis on Semiconductors and Dielectrics.

[258] Nauka, 1987. Elektronnye protsessy na poverhnosti poluprovodnikov pri hemosorbtsii. F. F. Volkenshtejn.

[259] N. Barsan. Conduction model in gas-sensing SnO2 layers: grain-size effects and ambient atmosphere influence. Sensors and Actuators. – 1994. – V. B 17. – P. 241-246.

[260] Krylov O. V. *Geterogennyj kataliz*. Moscow, Akademkniga 2004, 679 pp.

[261] N. Yamazoe, Y. Kurokawa, T. Seiyama Effects of additivies on semiconductor gas sensors. Sensors and Actuators. – 1983. – V. B4. – P. 283-289.

[262] S. Matsushima, Y. Teraoka, N. Yamazoe. Electronic interaction between metal additivies and tin dioxide in tin dioxide – based gas sensors. Japan J. Appl. Phys. – 1988. –V. 27, # 3. – P. 1798-1802.

[263] S. V. Ryabtsev, E. A. Tutov, A. N. Lukin, A. V. Shaposhnik. *Issledovanie mehanizmov sensibilizatsii dopirovannyh gazovyh sensorov*. Sensor, 2001, 1, pp. 26 - 30.

[264] S. V. Ryabtsev, E. A. Tutov, E. N. Bormontov, A. V. Shaposhnik. *Vzaimodeystvie metallicheskih nanochastits s poluprovodnikom v poverhnostno legirovannyh gazovyh sensorah*. Fizika i tehnika poluprovodnikov, 2001, Vol. 35 (7), pp. 869 - 873.

[265] X. Du and S. M. George, Sens. Actuators B 135, 152 (2008).

[266] X. Du, Y. Du, and S. M. George, J. Phys. Chem. A 112, 9211 (2008).

[267] M. K. Kumar, L. K. Tan, N. N. Gosvami, and H. Gao, J. Phys. Chem. C 113, 6381 (2009).

[268] M. K. Kumar, L. K. Tan, N. N. Gosvami, H. Gao. Conduction-atomic force microscopy study of H2 sensing mechanism in Pd nanoparticles decorated TiO2 nanofilm. J. App. Physics 106, 044308 (2009).

[269] N. Barsan, D. Koziej, and U. Weimar, Sens. Actuators B 121, 18 (2007).

[270] A. Pundt, M. Suleiman, C. Bahtz, M. T. Reetz, R. Kirchheim, and N. M.Jisrawi, Mater. Sci. Eng., B 108, 19 (2004).

[271] K. D. Schierbaum, U. Weimar, W. Gopel, and R. Kowalkowski, Sens.Actuators B 3, 205 (1991).

[272] N. S. S. Sharma, U. Kiyoshi, and J. Yusuke, Appl. Phys. Berlin 71, 2000 (1992).

[273] O. V. Safonova, T. Neisius, A. Ryzhikov, B. Chenevier, A. M. Gaskov,and M. Labeau, Chem. Commun. Cambridge 5202 (2005).

[274] J. J. Benitez, M. A. Centeno, C. L. D. Picard, O. Merdrignac, Y. Laurent,and J. A. Odriozola, Sens. Actuators B 31, 197 (1996).

[275] R. Pohle, M. Fleischer, and H. Meixner, Sens. Actuators B 78, 133 2001.17T. Pagnier, M. Boulova, A. Galerie, A. Gaskov, and G. Lucazeau, J. SolidState Chem. 143, 86 (1999).

[276] T. Pagnier, M. Boulova, A. Galerie, A. Gaskov, and G. Lucazeau, J. Solid State Chem. 143, 86 (1999).

[277] M.K. Kumar, L.K. Tan, N.D. Nitya, H. Gao, J. App. Physics, 106, 044308 (2009).

[278] U. Roland, T. Braunschweig, and F. Roessner, J. Mol. Catal. Chem. 127, 61 (1997).

[279] 95. T. B. Fryberger and S. Semancik, Sens. Actuators B 2, 305 1990.

[280] V.E. Henrich, P.A. Cox, The Surface Science of Metal Oxides, Cambridge UniversityPress, 1994, p. 263.

[281] N. Yamazoe, Sens. Actuators B 5, 7 (1991).

[282] M.K. Kumar, L.K. Tan, N.D. Nitya, H. Gao, J. App. Physics, 106, 044308 (2009).

[283] F. Favier, E. C. Walter, M. P. Zach, T. Benter, and R. M. Penner, Science 293, 2227 (2001).

[284] Y. Im, C. Lee, R. P. Vasquez, M. A. Bangar, N. V. Myung, E. J. Menke, R.M. Penner, and M. H. Yun, Small 2, 356 (2006).

[285] G. Korotcenkov, B.K. Cho. Bulk doping influence on the response of conductometric SnO2 gas sensors: Understanding through cathodoluminescence study. Sens. Actuat. B 196 (2014) 80–98

[286] N. Bârsan, M. Schweizer-Berberich, W. Göpel, Fundamental and practical aspects in the design of nanoscaled SnO2 gas sensors: a status report, Fresenius J. Anal. Chem. 365 (1999) 287– 304.

[287] D. Kohl. The role of noble metals in the chemistry of solid-state gas sensors. Sens. Actuators B 1 (1990) 158–165.

[288] G.S. Henshaw, R. Ridley, D.E. Williams. Room-temperature response of platinised tin dioxide gas-sensitive resistors. J. Chem. Soc., Faraday Trans. 92(1996) 3411–3417.

[289] V. Brynzari, G. Korotchenkov, S. Dmitriev, Theoretical study of semiconductorthin film gas sensitivity: attempt to consistent approach, J. Electron. Technol.33 (2000) 225–235.

[290] V. Brinzari, G. Korotcenkov, V. Golovanov, Factors influencing the gas sensingcharacteristics of tin dioxide films deposited by spray pyrolysis: understanding and possibilities for control, Thin Solid Films 391 (2001) 167–175.

[291] A. Klein, F. Sauberlich, B. Spath, T. Schulmeyer, D. Kraft, Non-stoichiometry and electronic properties of interfaces, J. Mater. Sci. 42 (2007) 1890–1900.

[292] R. Schafranek, A. Klein, In situ photoemission study of the contact formation of (Ba, Sr)TiO_3 with Cu and Au, Solid State Ionics 177 (2006) 1659–1664.

[293] T. Shimizu, H. Okushi, Intrinsic electrical properties of Au/$SrTiO_3$ Schottky junctions, J. Appl. Phys. 85 (1999) 7244–7251.

[294] S. Takatani, H. Miki, K. Kushida-Abdelghafar, K. Torii, Pt/$PbZr_xTi_{1-x}O_3$ interfacial reaction and Schottky barrier formation studied by X-ray photoelectron spectroscopy: effect of H_2 and O_2 annealing, J. Appl. Phys. 85 (1999)7784–7791.

[295] A. Dieguez, A. Vila, A. Cabot, A. Romano-Rodriguez, J.R. Morante, J. Kappler, N. Bârsan, U. Weimar, W. Göpel, Influence on the gas sensor performances of the metal chemical states introduced by impregnation of calcinated SnO_2 sol–gel nanocrystals, Sens. Actuators B 68 (2000) 94–99.

[296] A. Cabot, J. Arbiol, J.R. Morante, U. Weimar, N. Bârsan, W. Göpel, Analysis of the noble metal catalytic additives introduced by impregnation of as-obtained SnO_2 sol–gel nanocrystals for gas sensors, Sens. Actuators B 70 (2000) 87–100.

[297] C. Nayral, E. Viala, V. Colliere, P. Fau, F. Senocq, A. Maisonnat, B. Chaudret, Synthesis and use of a novel SnO nanomaterial for gas sensing, Appl. Surf. Sci.164 (2000) 219–226.

[298] S.J. Fonash, Solar Cell Device Physics, Academic Press, New York, 1981.

[299] K.C. Kao, W. Hwang, Electrical Transport in Solids, Pergamon Press, Oxford, 1981.

[300] B. Esfandyarpour, S. Mohajerzadeh, S. Famini, A. Khodadadi, E.A. Soleimani, High sensitivity Pt-doped SnO_2 gas sensors fabricated using sol–gel solutionon micromachined (1 0 0) Si substrates, Sens. Actuators B 100 (2004) 190–194.

[301] A.R. Phani, S. Manorama, V.J. Rao, Preparation, characterization and electricalproperties of SnO_2-based liquid petroleum gas sensor, Mater. Chem. Phys. 58(1999) 101–108.

[302] G. Korotcenkov, The role of morphology and crystallographic structure of metal oxides in response of conductometric-type gas sensors, Mater. Sci. Eng. R. 61 (2008) 1–39.

[303] I. Kocemba, J. Rynkowski, The influence of catalytic activity on the response of Pt/SnO_2 gas sensors to carbon monoxide and hydrogen, Sens. Actuators B 155 (2011) 659–666.

[304] G. Korotcenkov, B.K. Cho, M. Nazarov, D.-Y. Noh, E. Kolesnikova, Cathodoluminescence studies of undoped and (Cu, Fe, and Co)-doped SnO_2 films deposited by spray pyrolysis deposition, Curr. Appl. Phys. 10 (2010) 1123–1131.

[305] A. Cabot, A. Vila, J.R. Morante, Analysis of the catalytic activity and electrical characteristics of different modified SnO_2 layers for gas sensors, Sens. Actuators B 84 (2002) 12–20.

[306] J. Kappler, N. Bârsan, U. Weimar, A. Dieguez, J.L. Alay, A. Romano-Rodriguez, J.R. Morante, W. Göpel, Correlation between XPS, Raman and TEM measurements and the gas sensitivity of Pt and Pd doped SnO_2-based gas sensors, Fresenius J. Anal. Chem. 361 (1998) 110–114.

[307] D. Koziej, M. Hubner, N. Bârsan, U. Weimar, M. Sikoraz, J.-D. Grunwaldt, Operando X-ray absorption spectroscopy studies on Pd-SnO_2-based sensors, Phys. Chem. Chem. Phys. 11 (2009) 8620–8625.

[308] M. Hübner, D. Koziej, M. Bauer, N. Bârsan, K. Kvashnina, M.D. Rossell, U.Weimar, J.D. Grunwaldt, Catching the state of Pt in SnO_2-based sensors under working conditions, Angew. Chem. Int. Ed. 50 (12) (2011) 2841–2844.

[309] Y.B. Xue, Z.A. Tang, Density functional study of the interaction of CO with undoped and Pd doped SnO_2 (1 1 0) surface, Sens. Actuators B 138 (2009)108–112.

[310] M.A. Maki-Jaskari, T.T. Rantala, Density functional study of Pd adsorbates atSnO_2 (1 1 0) surfaces, Surf. Sci. 537 (2003) 168–178.

[311] W. Zeng, T. Liu, D.J. Liu, E.J. Han, Hydrogen sensing and mechanism of M-doped SnO_2 (M = Cr3+, Cu2+and Pd2+) nanocomposite, Sens. Actuators B 160(2011) 455–462.

[312] S.R. Morrison, Selectivity in semiconductor gas sensors, Sens. Actuators 12(1987) 425–440.

2. Methods of experiment

2.1. Synthesis of nanopowders

Two approaches for synthesizing tin dioxide nanopowders are peresented. The first one was developed to be compatible with tin and titanium oxides co-precipitation. The second one was developed to mix the obtained oxide with copper oxide and some noble metals.The procedures for obtaining Titanium oxide nanopowders, as well as tin-titanium mixed oxides powders are also presented.

2.1.1. Tin dioxide synthesis for hydrogen thick-layer sensors

Precipitation method [1] was modified and used to synthesize nanodispersed tin dioxide. Tin (IV) acetate was dissolved in glacial acetic acid. $NH_3 \cdot H_2O$ was added dropwise to cause hydrolytic precipitation of tin dioxide:

$$Sn(CH_3COO)_4 + 4NH_3 + 3H_2O \longrightarrow H_2SnO_3 \downarrow + 4CH_3COONH_4$$

The obtained colloid was precipitated by centrifugation (6000 rpm, 5 minutes), and dried for 12 hours at 100°C, 2 hours at 350°C and 30 minutes at 440°C. For used reagents details see Table 2.1; for the equipment description see Table 2.2.

We have found that the crystallite size of producing tin dioxide depends on the conditions of the synthesis: concentration of tin acetate, pH and temperature of precipitation. When the formation of $SnO_2 \cdot xH_2O$ takes place in soft conditions – low tin acetate concentration (<0.8 g/L) and low temperature (<25^{o}C), – it is possible to stop it in the very beginning of colloid phase appearance. In this case, it is possible to obtain tin dioxide with mean crystallite size 1.0 nm (measured after drying at 350°C for 2.5 hours). In these conditions, the reaction yield is quite low and the synthesis is very reagent-consuming.

In order to increase the yield of the synthesis, it is possible to use higher temperature of precipitation and higher concentration of the precursors. When

optimal (from the point of view of yield and dispersivity) tin acetate concentration (2 g/L in final solution) and the temperature of precipitation (50°C) are used, mean crystallite size of the material amounts to 1.8 – 2.0 nm (XRD), while mean particle size is about 4 nm (TEM).

The increase of precipitation and aging time to 70 hours results in increase of mean crystallite size up to 3.0 nm and mean particle size to 8 nm.

Table 2.1.Used reagents

Name in text	*Formula*	*Producer*	*CAS number*
Tin (IV) acetate	$Sn(CH_3COO)_4$	Sigma-Aldrich	2800-96-6
Acetic acid	CH_3COOH	Sigma-Aldrich	64-19-7
Ammonia water solution	$NH_3 \cdot H_2O$	Fluka	1336-21-6
Titanium (IV)isopropoxide	$Ti(O(CH_3)_2)_4$	Sigma-Aldrich	546-68-9
Ethanol	C_2H_5OH	Scharlab	64-17-5
propanediol-1,2	$CH_2(OH)CH(OH)CH_3$	Sigma-Aldrich	57-55-6

Table 2.2.Used equipment

Name in text	*Producer, model, characteristics*
Furnace	Chamber laboratory furnace Carbolite 1200° (RHF)
Centrifuge	Hettich EBA 20, 6000 rpm, 3460 RCF

2.1.2. Titanium dioxide synthesis

Titanium (IV) isopropoxide is insoluble in acetic acid. It was necessary to dissolve it first in an auxiliary solvent. The latter was prepared as follows: 9 parts of acetic acid were mixed with 10 parts of ethanol and heated up to 100°C, avoiding boiling. Appropriate volume of titanium isopropoxide (from 0.05 to 1 ml) was dissolved in 7 ml of freshly prepared solution at temperature about 60°C. Next, just-prepared solution containing titanium isopropoxide was added to acetic acid at room temperature under stirring. Under these conditions, the addition of each solution to another did not cause premature precipitation of tin dioxide.

Titanium isopropoxide is unstable even in the final solution. If the synthesis lasts too long (more than 1.5–2 hours) or ammonium hydroxide is added too fast, the solution grows turbid because of titanium dioxide formation. During the development of titania synthesis conditions attention was paid on the proper time of the appearance of colloid, because the purpose was to use this procedure later to precipitate tin oxide and titanium oxide together, at the same time, when preparing mixed oxides and avoid premature precipitation of titania.

It was found that the optimal method was to add estimated volume of ammonium hydroxide dropwise during 1.5 hours under intensive stirring and cooling.

2.1.3. Synthesis of tin-titanium oxide co-precipitate

The original aim was to synthesize mixed (double) oxides of tin and titanium. But since no experiments were made on the homogeneity of the distribution of two phases in each other, we use the term “co-precipitated materials” or “co-precipitates” instead of “mixed oxides”.

Tin-titanium oxide co-precipitated materials with wide molar fraction of titania ranging from 0 to 100% (0, 10, 20, 30, 50, 70, 100%) were synthesized.

Titanium (IV) isopropoxide, primarily dissolved in auxiliary solvent as described above, and tin (IV) acetate were dissolved in glacial acetic acid in appropriate amounts. The addition of ammonium hydroxide (1.55:1 $NH_3 \cdot H_2O$: CH_3COOH) was carried out at low temperature (6°C at the end of ammonia addition) and intensive stirring. Precipitation was caused by heating the solution to as much as 55°C in order to be sure that all tin and titanium passed into colloidal phase. The conditions of the precipitation of tin and titanium were chosen reasoning from the experiments with individual oxides precipitation. It was found that, using the chosen conditions, the synchronous and complete precipitation of both tin and titanium oxides is ensured.

Co-precipitated materials will be denoted below as cp ST XY, where "cp" means co-pecipitated material, "ST" – Sn and Ti, X and Y – molar fraction of Sn and Ti, accordingly. For example, cp ST 91 is a co-precipitated material, where molar fraction of Sn in the solution used for the synthesis was 90%. Following an analogous criteria, mixed oxides will be denoted as "mm ST XY".

2.1.4. Tin dioxide synthesis for hydrogen sulfide, acetone, and ammonia thick-layer sensors

Tin dioxide was synthesized in general in the same way as described above for TiO_2-SnO_2 sensors. The differences in synthesis approaches are described below.

Tin (+2) acetate was dissolved in glacial acetic acid to obtain 1 g/l concentration. Then, the solution was cooled down to 3 °C. After that, a molar excess of 35% hydrogen peroxide was added to the solution. In order to ensure the complete oxidation of tin, the solution was hold for 12 hours at 6 °C:

$$Sn(CH_3COO)_2 + H_2O_2 + 2CH_3COOH \longrightarrow Sn(CH_3COO)_4 + 2H_2O$$

25% ammonia solution was added to the obtained solution of tin (+4) acetate until pH reached value 4.5:

$$Sn(CH_3COO)_4 + 4NH_3 + 3H_2O \longrightarrow H_2SnO_3 \downarrow + 4CH_3COONH_4 .$$

Stannic acid was separated from the solution by centrifugation, rinsed with deionized water, and separated by centrifugation again. This process was repeated for 10 times. In order to prevent stannic acid coagulation during drying, the precipitate was rinsed by 1-propanol, whereupon H_2SnO_3 was educed again by centrifugation. Nanodisperse stannic acid first was dried for 5 hours at 65°Cand later annealed at 450°C during 10 hours:

$$H_2SnO_3 \xrightarrow{T\uparrow} SnO_2 + H_2O\uparrow$$

2.2. SnO_2 nanowires synthesis method

Gas transport method based on vapor–liquid–solid (VLS) mechanism was used for SnO_2 nanowires synthesis. Argon saturated with water vapors served as ambient. Water was used as a tender oxidant of metallic tin:

$$Sn + 2H_2O \rightarrow SnO_2 + 2H_2$$

The temperature of the metal source in a tubular furnace (figure 2.1) was 1100 ^oC.

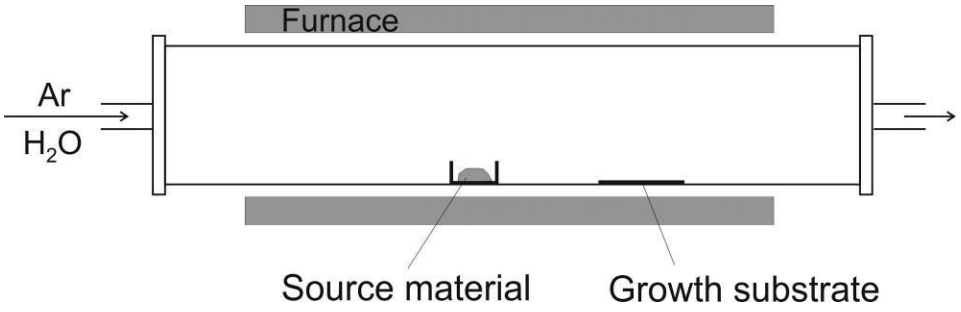

Figire 2.1. Scheme of SnO_2 nanowire synthesis

Droplets of noble metal catalyst are usually used in VLS method of nanowire growth. In the present work, no impurities were used; the nanowires were obtained onto the surface of a quartz pipe.

The key parameters of nanowire fabrication are:

- Source materials: metal / metal oxide, and their combinations
- Temperature of source material (1000-1300 ^oC)
- Ambient composition (Ar, Ar+O_2, Ar+H_2O)
- Ambient pressure
- Flow rate(1–3)·$10^{-6}m^3s^{-1}$.

- Temperature of the substrate (700-1000 ^{o}C).

Tin dioxide, formed in a liquid drop, was crystallized from the drop, gradually forming nanowire, while the process of tin condensation from gas phase to the drop continues. The formed quasi-homogeneous material represents wires with thickness 20-500 nm and with length exceeding thickness on 3-4 orders.

2.3. Paste preparation and deposition of thick sensing layers

The powders obtained by procedures described above were used to prepare pastes which were deposited onto alumina substrates by drop-coating to form sensing layers.

2.3.1. Paste preparation and deposition of sensing layers for hydrogen sensing experiment

The powders were prepared for deposition as follows. The oxides obtained by procedures described above were grindedin agate mortar (mixed in the desired proportion to obtain oxide mixtures).After preparation of the powder with required molar ratio of oxides, the material was mixed with propanediol-1,2 in the weight ratio 2:1 in the same mortar and was grinded until the formation of the paste with requiredhomogeneity and viscosity. The latter was deposited on substrates by drop deposition. The substrates with deposited ink were dried at 150°C for 40 minutes and annealed at 700°C for 5 minutes. Smoothness of the obtained layer was controlled using microscope. Substrates with deposited materials were soldered to TO-8 packages.

As-prepared sensors were stabilized at ambient air for 72 hours at 350°C.

Mixtures of individual tin and titanium oxides will be denoted below as “mechanical mixtures” with X% TiO_2 in SnO_2.

The mechanical mixtures were prepared by mixing tin and titanium oxides in a mortar prior to the deposition on the substrate.

The characterization of the sensing properties of the materials was performed on alumina microsubstrates (2.0×0.4×0.2 mm) with gap platinum electrodes and a platinum heater described in [2]. The microsubstrates were assembled in TO-8 package.

2.3.2. Paste preparation and deposition of sensing layers for detection of other gases

2.3.2.1. Materials for hydrogen sulfide and acetone thick-layer sensors

Tin oxide prepared according the procedure described in chapter 2.1.4. was mixed with copper oxide and some metals in the following concentration:SnO_2 + 3%CuO, SnO_2 + 2%CuO + 2%Au, SnO_2 + 3%Pt, SnO_2 + 3%Pd, SnO_2 + 2%Pt + 2%Pd (all proportions given in weight %) were prepared. For this purpose SnO_2nanopowder was mixed in a mortar with copper oxide. Other dopants were mixed with SnO_2 in a mortar using their water solutions: hydrogen tetrachloroaurate (aurochloric acid); tetraammineplatinum(II) nitrate; tetraamminepalladium(II) nitrate. All the used chemicals were analytical grade. After the impregnation, obtained materials were dried at 80 ^{o}C.

The materialswere depositedby drop-coating on the same alumina microsubstrateswhich were described at paragraph 2.3.1. The substrates were electrically connected to TO-8 packaging.

2.3.2.3. Manufacture of ammonia converter

In this case, the powder including tin dioxide and dopants as Pd and Pt,obtained by the procedure described in 2.1.4 and 2.3.2.1, was mixed with glycerin,usedas a filling material, in an agate mortar to obtain a paste. The paste was deposited later on a substrate (described in 2.3.1). The substrate with deposited layer was heated up to 650 ^{o}C with heating rate of 50^{o}C per minute, remaining at this temperature for 15 minutes;then the substrate was cooled down to 450 ^{o}C and kept at this temperature for 1 hour. This procedure was performed in a muffle furnace (PTK 1/2-40). During the annealing, three-dimensional tin dioxide structure wereformed. Noble metal reduction and burning of organic filler also took place.

After the formation of gas sensing layer, the substrates were soldered to TO-8 package (figure 2.3).

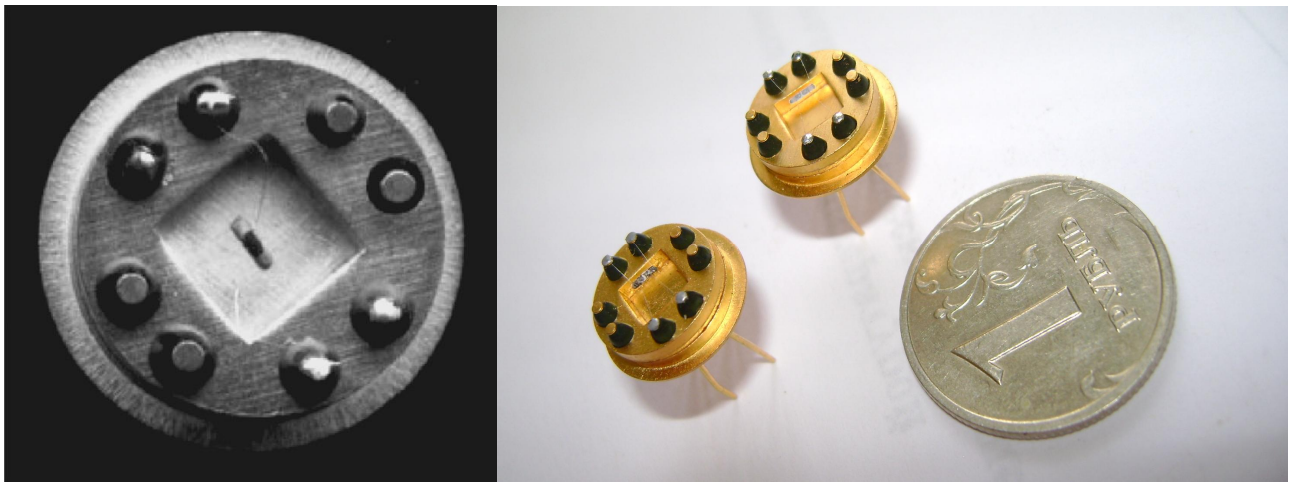

Figure 2.3. Substrate with TO-8 package

2.4. Manufacture of single nanowire devices

Individual nanowires were electrically contacted by direct Focused-Ion-Beam (FIB) platinum deposition, using a FEI Dual-Beam Strata 235 instrument combined with a metallorganic injector to deposit platinum.

Common look of the device is presented on figures 2.4 and 2.5.

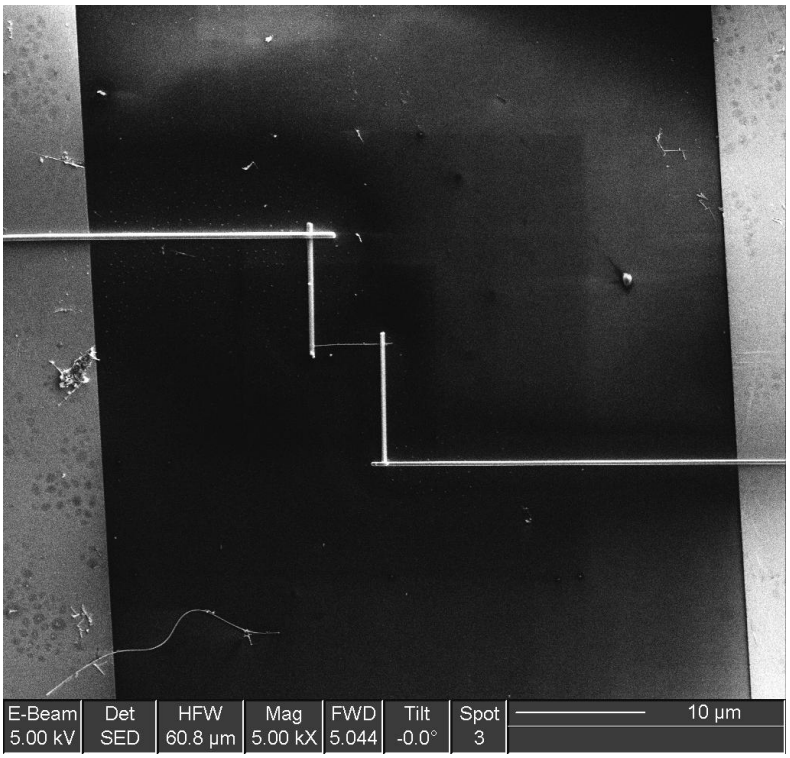

Figure 2.4. Single nanowire electrically connected to a

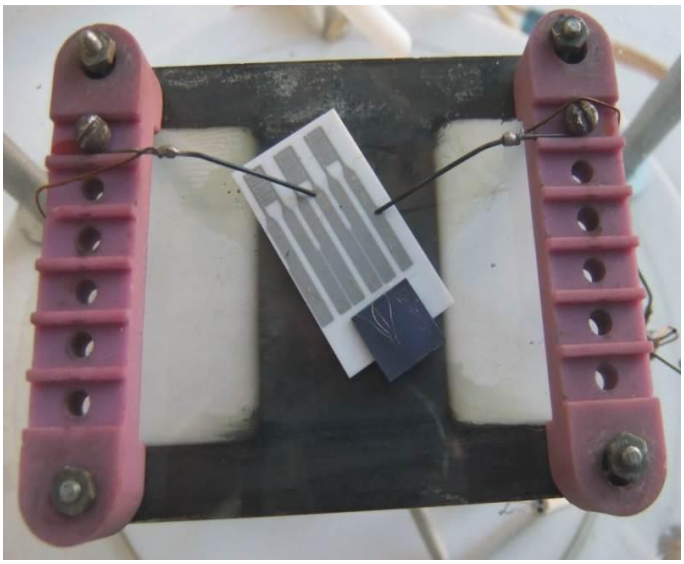

Figure 2.5. Single nanowire sensing device mounted inside the gas chamber

2.5. Methods of materials characterization

2.5.1. Transmission electron microscopy

Jeol JEM 1011 microscope operating at 100 kV (tungsten cathode) was used to estimate the particle morphology of the materials described in paragraphs 2.1.1, 2.1.2, 2.1.3. The sample preparation was as follows. A specimen of the solid was carefully grinded and dispersed in absolute ethanol (Sigma-Aldrich, p/n24194) using ultrasound bath. Then, a drop of the suspension was deposited on copper grid for TEM analysis and left for 15 min in air at 60^{o}C to evaporate the solvent. After this, the support was placed into the holder and inserted into the TEM chamber.

2.5.2. XRD study

TXRD measurements were made using a BRUKER D8 ADVANCE diffractometer equipped with parallel incident beam (Göbel mirror), vertical θ-θ goniometer, XYZ motorized stage and with a GADDS (General Area Diffraction System) and equipped with an MRI BTS-BASIC platinum ribbon heating stage. Samples were placed directly on the sample holder and the area of interest was selected with the aid of a video-laser focusing system. An X-ray collimator system allows to analyze areas of 500 μm. The X-ray diffractometer was operated at 40 kV and 40 mA to generate $Cu_{k\alpha}$ radiation. The GADDS detector was 30x30 cm with a 1024x1024 pixel CCD sensor. We collected two frames (2D XRD pattern), covering 20-80^{o} 2θ at a distance of 15 cm from the sample to the detector. The exposition time was 300 s per frame and they were chi-integrated and merged to generate the conventional 2θ vs. intensity diffraction pattern. The first diffraction pattern was collected at room temperature, the second one was collected at 700ºC with a heating rate of 0.1667º/s. The third and followings patterns were collected consecutively at the same temperature after 600 s. A total of 91 patterns were collected at the same temperature of 700^{o}C for about 32 hours. The representative time (in seconds) used for each pattern was

when it started to be collected. Static air atmosphere was used throughout the analysis. Identification of the minerals was achieved by comparison of the XRD diffractogram with the ICDD data base (release 2007) using Diffrac^{plus} Evaluation software (Bruker 2007).

The X-ray diffractograms were analyzed in a first approach by profile analysis using the program TOPAS 4.2 [3], working with local routines, that fits the observed diffractogram to a calculated one from a model. A pseudo-Voigth function was used to fit the diffracted pattern. The instrumental contribution to the peak width was obtained from a sample of LaB_6 from the NIST (SRM 676b). The LaB_6 pattern was analyzed with the same software by fitting a pseudo-Voigth function. The calculated parameters for LaB_6 were maintained constant for SnO_2 samples but only fitting the integral breadth of the diffracted peaks produced by the crystallite size of the SnO_2. Apart from that, for each pattern was fitted the zero shift, a 2 degree Chebychev polynomial as a background, cell parameters for SnO_2 (Cassiterite, $P4_2/mnm$, a=b= 4.73820 Å, c= 3.18710 Å) and TiO_2 (Anatase, $I4_1/amd$, a=b= 3.7852 Å, c= 9.5139 Å; Rutile, $P4_2/mnm$, a=b= 4.5933 Å, c= 2.9592 Å) and the intensity of each reflection.

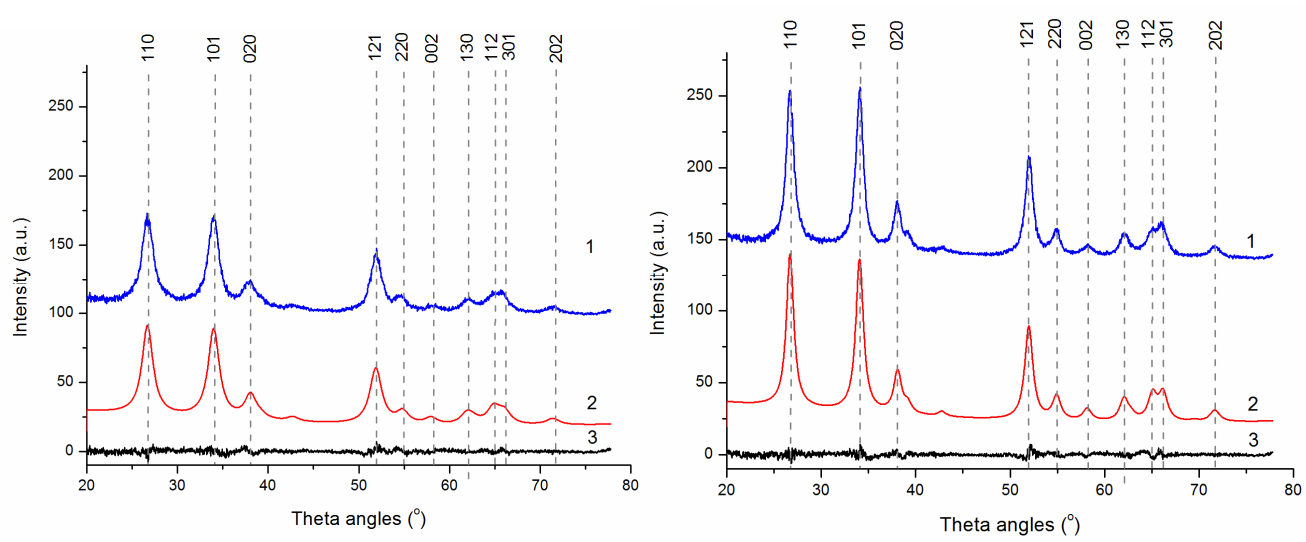

Figure 2.6. Experimental diffractograms (1), their fitting with Voigt function (2) and the difference between them (3) for sample cp ST-73at annealing time t=0 h (a) and t=31 h (b)

Figure 2.6 shows the fitted pattern taken at 700°C after 32 h for sample cp ST-73. The criteria of fit was the commonly R_{wp} value used in Rietveld analysis. We

obtained in all patterns fitted aR_{wp}value ranging from 7.0 up to 11.0 indicating a good agreement between the observed diffractogram and the calculated one.

The mean crystallite size (D), or the volume-weighted domain size in crystallographic terms, is calculated from the integral breadth of the peak, according to the modified Scherrer expression [4]:

$$\beta^S = \frac{\lambda}{D\cos\theta}$$

whereλ is the wavelength of incident radiation and ϑ is the Bragg angle. Double Voigt Approach was used to estimate crystallite size and was simplified assuming that there is no contribution to the integral breadth of the peak from the microstrain and that the Lorentz component alone determines the crystallite size.

Co-precipitated materials cp ST91, cp ST73, as well as SnO_2 and TiO_2, werecharacterized by this method.

2.5.3 FTIR spectroscopy

FTIR spectra were recorded using JASCO 680 Plus spectrometer. The sample in a quantity of 0.006(±1) g was mixed with 0.30(±2) g of KBr powder (Sigma, IR grade) and then grinded in the agate mortar for 5 min. The resulting powder was pressed into self-supporting disks and then used for the measurements. To record the background spectrum the self-supporting disk of blank KBr is used. The spectra acquisition was performed in the absorption mode with 32 scan times and resolution 2 cm^{-1}. All measurements were carried out at RT and in air.

Co-precipitated materials cp ST91, cp ST73, as well as SnO_2 and TiO_2, werecharacterized by this method.

2.5.4. SEM characterization

Images of SnO_2 nanowires were obtained using JEOL JSM-6380 LV scanning electron microscope (Voronezh State University, Russia).

2.6. Methods of gas sensing experiments

2.6.1. Hydrogen gas sensing experimental set-up

Experiments for determining hydrogen gas sensing properties of the synthesized materialswere carried out using the experimental set-up shown on figure 2.7.

The sensors were covered with caps allowing gas transfer to the sensor's surface and deposited in Teflon gas chamber with interior volume ~50 cm^3.

The pins of TO-8 package were connected to sockets and the latter were connected to digital high resistance ohmmeter/multimeterKeithley 6517A and to Agilent E3631A device used as power supply for the sensor's heater.

Environics Series 4000 gas mixing system was used for the preparation of gas mixtures. Environics Series 4000 software was used as user interface for the instrument. Stainless steel and teflon tubes were used to interconnect gas mixing system and experimental chamber.

Following initial gas mixtures were used in this study:

Dry synthetic air;

20 ppm hydrogen solution in synthetic air;

1000 ppm hydrogen solution in synthetic air.

Humidity and hydrocarbons impurity level for all initial gases were less than 3 ppm.

Humidity level was adjusted using Environics saturator with deionized water.

The experiments on gas sensing properties of the materials presented here aimed to study the dependence of gas sensors signals on hydrogen concentration, temperature and humidity.

The experiment was carried out as follows: sensors were stabilized at 350°C for 72 hours in ambient air before any measurement, and after that in the gas chamber, in atmospheres of synthetic air and 20 ppm hydrogen, switching every hour. Next, sensors were exposed to the synthetic air flow at target temperature until the stabilization of the resistance of the sensing layer. Signal values were calculated as $(R_{air}-R_{gas})/R_{gas}$, where $R_{air}$is the resistance in pure air, and $R_{gas}$is the one in the presence of the target gas.

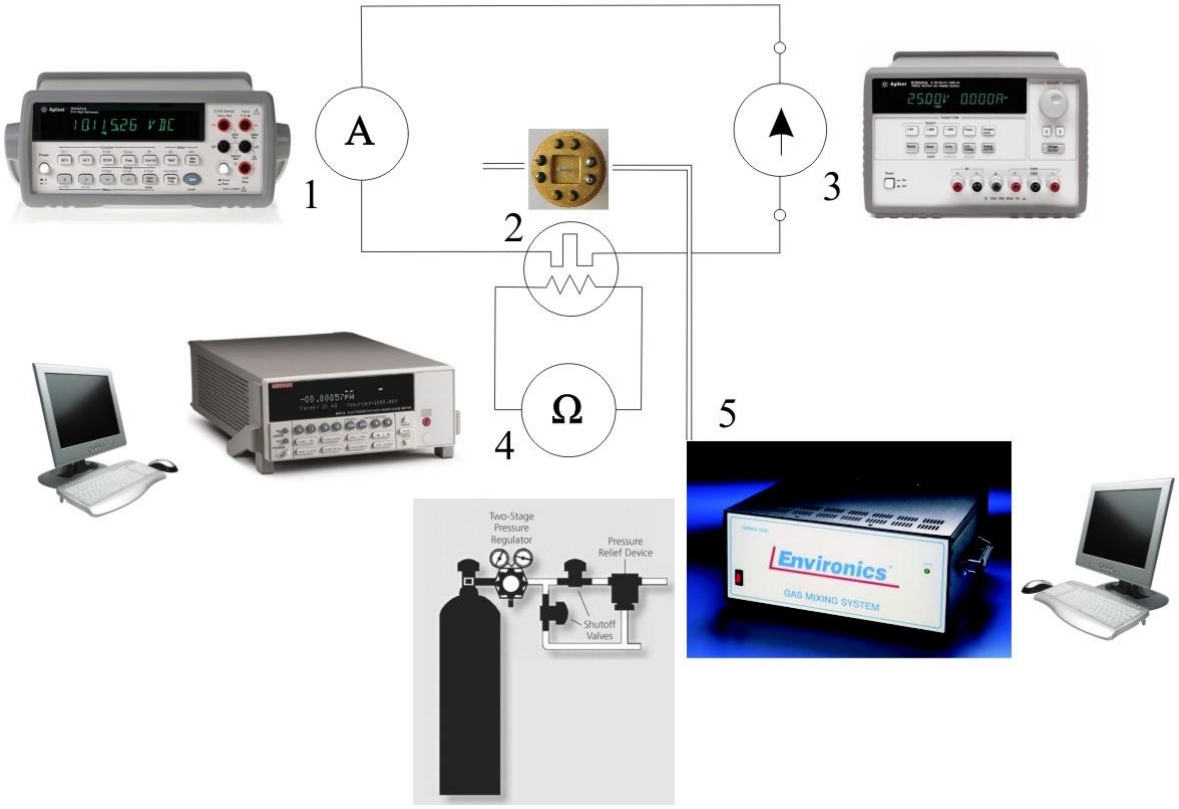

Figure 2.7. Gas sensing experiment setup: 1 –multimeter, 2 – sensor, 3 – power supply, 4 – electrometer, 5 – gas mixing system. For equipment details see table 2.

Table 2. List of equipment used in hydrogen sensing experiment

Name in text	*Model name*
Electrometer	electrometer / high resistance meter Keithley 6517A
Power supply	triple output DC power supply Agilent E3631A
Multimeter	digital multimeter Agilent 34401A
Gas mixing system	Environics Series 4000

2.6.2. Other gases sensing experimental set-up

Ammonia, hydrogen sulfide and Acetone were performed using a gas chamber, where the sensors, as well as “sensor+converter” device were located during experiments. This chamber was made of Teflon; with an interior volume of ~200 cm^3.

Characteristics of the sensors were examined in gas flow conditions. Gas mixtures were made using gas mixing system MICROGAS-F-12 and microflow source “Hydrogen sulfide”, model IM03-M-A2. According to calibration scheme for gas phase components measuring equipment (GOST 8.578-2008), this gas flow source is a working standard of 1st grade.

Gas flow rate was controlled by digital mass flow controller ELTOCHPRIBOR RRG-12 with total systematical constituent of basic reduced uncertainty equal to 1%.

The sensor signal was defined as normalized difference of sensor electroconductivity in the examined ambient (σ_x) and in reference ambient (σ_0). Reference ambient was synthetic air.

$$G = \frac{|\sigma_x - \sigma_0|}{\min(\sigma_x, \sigma_0)} = \frac{|R_x - R_0|}{\min(R_x, R_0)}$$

For the work in nonstationary temperature mode it was used an automatic device (figure 2.8) developed in Voronezh state university (Russia) by Dr. S.V. Ryabtsev. The feature of the temperature controlling device concluded in the possibility to maintain and control sensors' temperature in the conditions when the converter located in a close distance (~2 mm)to the sensor being heated and cooled influencing the sensor's temperature.

Special program complex was developed for device control. Program "SenSet"

Figure 2.8. Gas analyzer for 4 sensors working in nonstationary temperature regimes

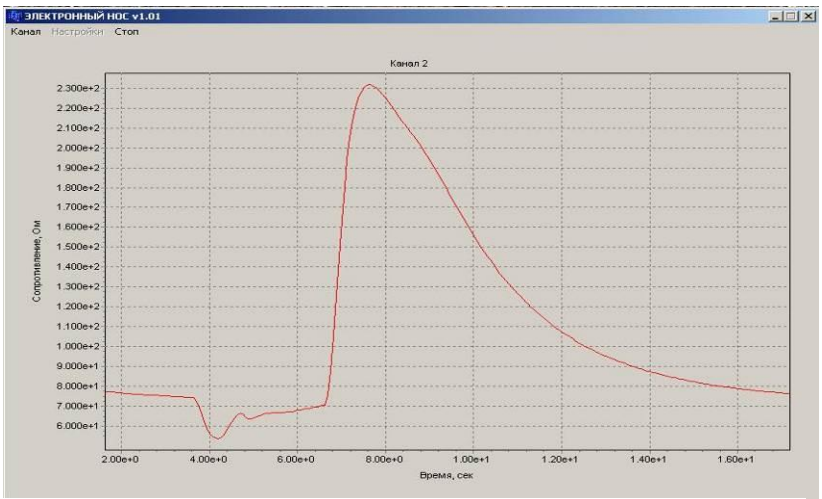

Figure 2.9.GUI of SensReader program

allows stationary, “steps” or sinusoid temperature mode setting for each of the four sensors allocated in the chamber. The program allows setting both the duration of the cycle and the range of temperature change during the work in non-stationary modes.

2.6.3. Gas sensing set-up using SnO_2 nanowire devices

Electrical measurements of SnO_2 nanowire based devices were performed using Keithley 2400 Source Meter Unit (SMU). For gas sensing experiments, the devices were placed in a chamber with an integrated heater; the gas flow (≥ 99.999% purity) was regulated by mass flow controllers.

References Chapter 2

[1] Pavelko R. G. Vasiliev A. A. Gispert-Guirado F., Barrabes, N., Llorca, J., Llobet, E., Sevastyanov, V. G. Crystallite growth kinetics of highly pure nanocrystalline tin dioxide: The effect of palladium doping. Materials Chemistry and Physics, 121: p. 267-273, 2010

[2] V.V. Malyshev, A.V. Pislyakov, Investigation of gas-sensitivity of sensor structures to carbon monoxide in a wide range of temperature, concentration and humidity of gas medium, Sensors and Actuators B-Chemical, 123 (2007) 71-81.

[3] TOPAS, in: General Profile and Structure Analysis Software for Powder Diffraction Data, V 4.2, Bruker AXS GmbH, Karlsruhe, Germany.

[4] A.R. Stokes, A.J.C. Wilson, A method of calculating the integral breadths of Debye-Scherrer lines, Proc. Camb. Phil. Soc. , 38 (1942) 313-322

3. Materials characterization

3.1. Comparative characterization of SnO_2, TiO_2 and SnO_2-TiO_2 materials

In this chapter we compare two types of SnO_2-TiO_2 materials. The first one was synthesized by co-precipitation method, described in Chapter 2.1.3, while the second one was prepared through mechanical mixing of SnO_2 and TiO_2 powders, obtained according the procedures described in 2.1.1 and 2.1.2, respectively. Each type of materials is presented with different SnO_2/TiO_2 ratios. Pure SnO_2 and TiO_2 powders were used to contrast the effect of the admixture or dopant. FTIR spectroscopy is used to qualitatively compare the amount of hydroxyl groups on the materials in question. Using in-situ XRD we examine crystallite size evolution of the synthesized materials.

Figure 3.1 shows TEM images of some synthesized materials after drying and annealing at 350°C for 150 and at 440°C for 30 minutes. Co-precipitated materials are denoted as “cp ST XY”, where “cp” means co-pecipitated material, “ST” – Sn and Ti, X and Y – molar fraction of Sn and Ti, accordingly. For example, cp ST 91 is a co-precipitated material, molar fraction of Sn in the solution used for which synthesis was 90%.

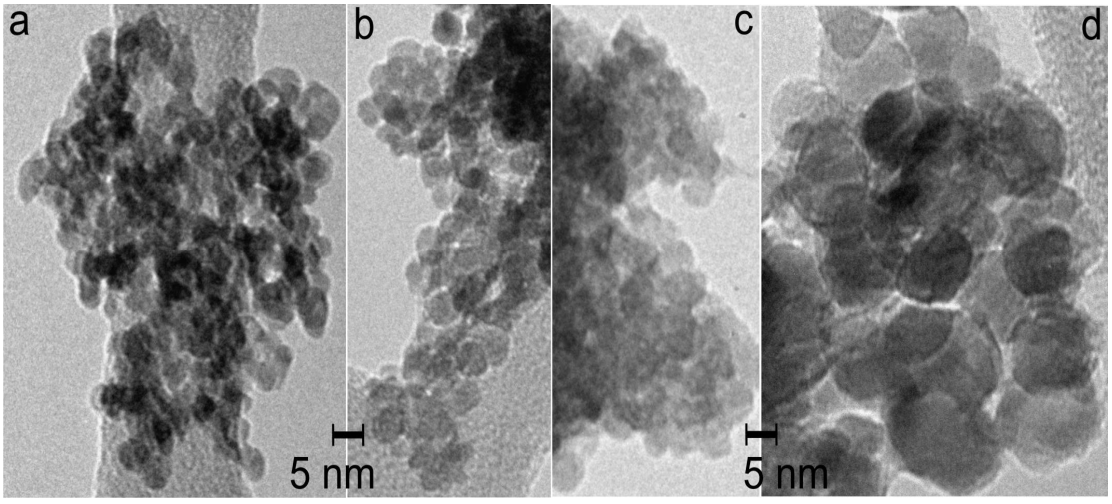

Fig. 3.1. TEM images of blank tin oxide (a), cp ST-91 (b) cp ST-73 (c) and blank TiO_2 (d).

Mixed oxides are denoted as “mm ST XY”.

Mean particle size for blank SnO_2 was found to be close to 4 nm, while mean crystallite size for this material amounts to 2 nm. Both values are lower by ca. 1.5 times compared to SnO_2 bulk doped with TiO_2. In the case of blank TiO_2 the particles are notably larger, with size between 5 and 18 nm, and mean crystallite size about 6 nm.

FT-IR spectroscopy was used to compare amount and acidity of surface hydroxyls for the co-precipitated and blank materials (Figure 3.2). The broad band centered at ca. 3420 cm^{-1} is assigned as stretching vibrations of bridge-bonded or/and hydrogen-bonded OH groups [1]. It is also known that the highest frequency between 3800-2500 cm^{-1} is assigned to the most basic hydroxyl groups with the lowest coordination number of the oxygen. Decrease in OH frequency is therefore associated with the increase of coordination number of the oxygen and possible hydrogen bonding [2].

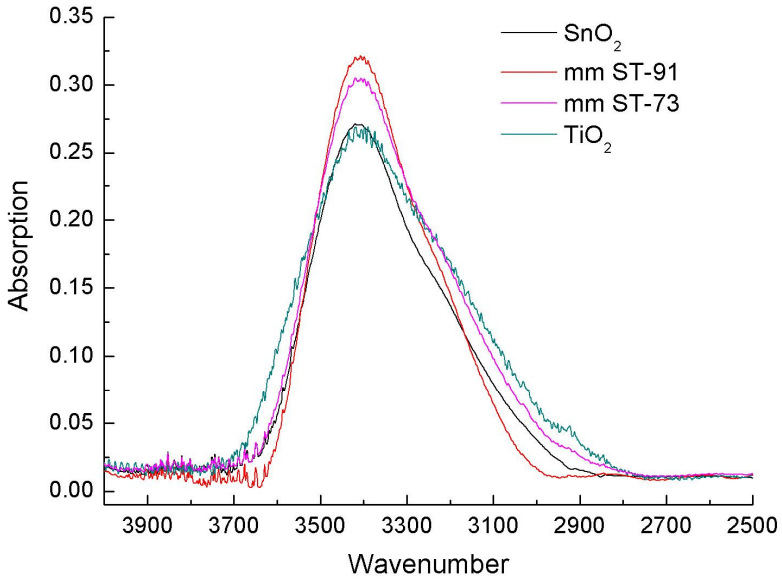

Fig. 3.2. FTIR spectra of some synthesized materials

The position of the band suggests that the dominant specie for all materials is the one vibrating at ca. 3420 cm^{-1}. This position will be taken as reference and higher or

lower acidity of OH groups will be judged in respect of this value hereinafter. The shapes of the bands indicate rather different contribution of hydroxyl groups with higher and lower acidity. Let us compare blank materials first. The band of TiO_2 is remarkably broader in both directions than that of SnO_2. The highest broadening is observed in low frequency region, implying higher amount of more acidic OH groups. The "partial" content of less acidic hydroxyls is also higher for TiO_2. Both these facts suggest that OH groups on TiO_2 surface are more heterogeneous regarding their acidity in respect with SnO_2. They are also ca. 20% more numerous judging by band integral, normalized by sample weight, and this is regardless the fact that surface of SnO_2 is higher than that of TiO_2 after annealing at 440 ^oC.

Doping with 10 w.% TiO_2 leads to increase in the dominant specie quantity, as well as slightly decreases acidic hydroxyl groups. Further doping with 30 w.% TiO_2 maintain the amount of the dominant species at high level compared to the blank SnO_2 but in this case increases acidic OH groups similarly to blank TiO_2.

The general tendency that can be derived from figure 3.2 is that the doping with TiO_2 results in higher overall amount of hydroxyl groups compared to blank SnO_2. Apart from that, OH groups become slightly more acidic in respect with the dominant specie. These results are in good agreement with the ones obtained previously for SnO_2 materials doped with IVB elements [3].

According to the conventional XRD analysis, co-precipitated materials as well as blank SnO_2 are crystallized in rutile modification: $P4_2/mnm$, a=b= 4.73820 Å, c= 3.18710 Å (Cassiterite). On the other hand, blank TiO_2 possesses anatase structure: $I4_1/amd$, a=b= 3.7852 Å, c= 9.5139 Å, which means that mechanically mixed SnO_2 and TiO_2 consist of two phases rutile (from SnO_2) and anatase (from TiO_2).

Upon isothermal annealing at 700^oC no phase transitions were observed for co-precipitated materials and blank SnO_2 (see e.g. figure 3.4). However, anatase phase of blank TiO_2 transforms under the same conditions to the rutile phase: $P4_2/mnm$, a=b= 4.5933 Å, c= 2.9592 Å (Figure 3.3). Anatase-rutile transformation (ATR) occurs already at temperatures below 700^oC, since upon reaching this

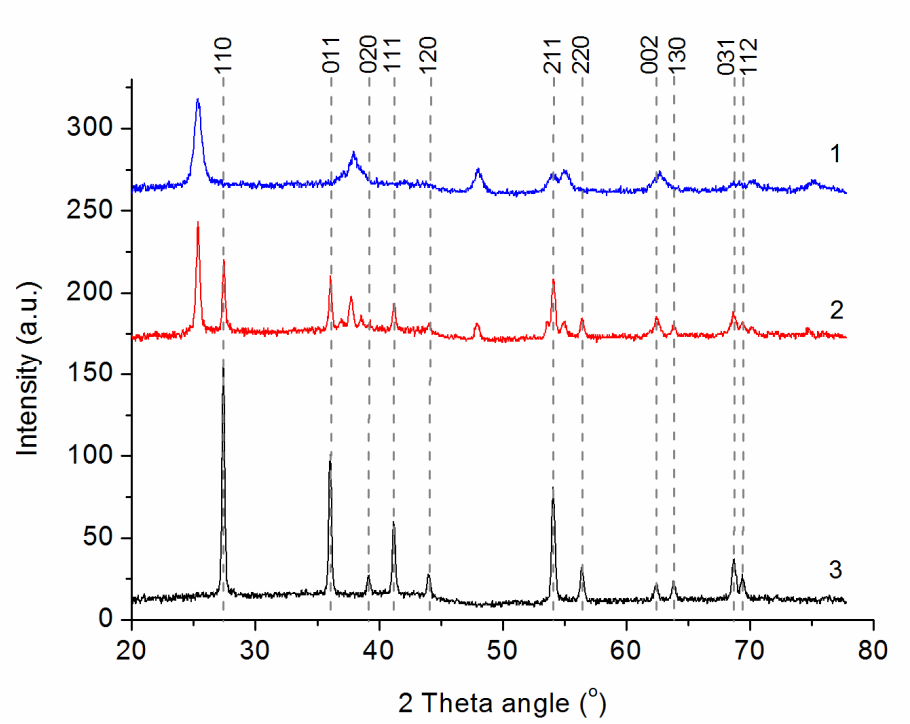

Fig. 3.3. Diffraction patterns of blank TiO_2 before annealing (1), after reaching 700°C (2) and after 31 h of annealing (3)

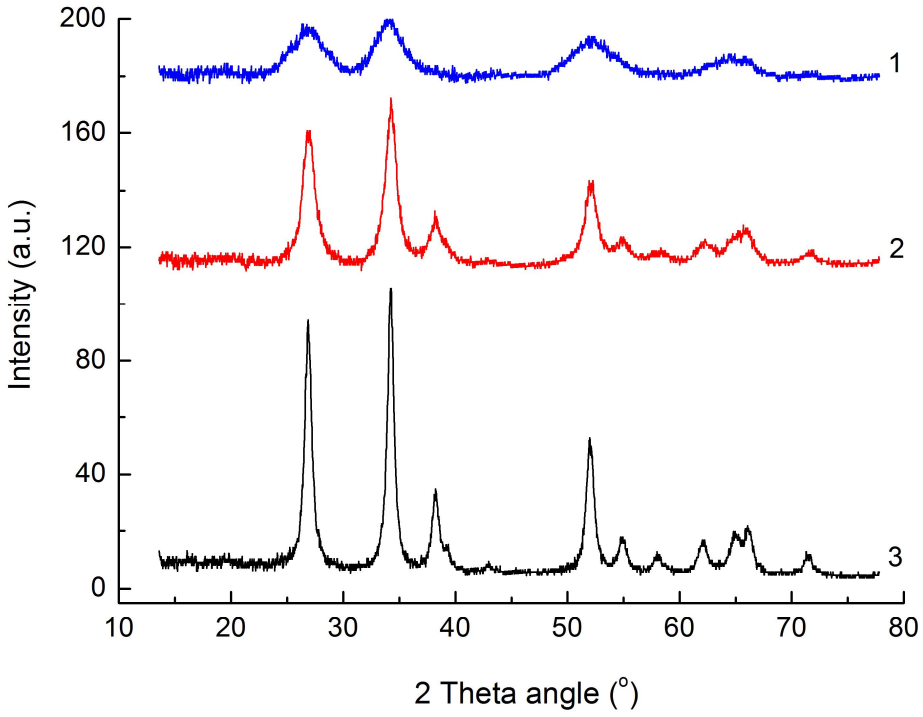

Fig. 3.4. Diffraction patterns of blank SnO_2 before annealing (1), after reaching 700°C (2) and after 31 h of annealing (3)

temperature the material already consists of two phases with ca. 1:1 weight ratio. The fact of ATR for blank TiO_2 as well as its temperature are in good agreement with the literature [4].

Apart from the phase transition in blank TiO_2, abrupt growth of crystallites occurs upon isothermal annealing. This phenomenon is well known and believed to be due to breaking of old and formation of new bonds in the crystalline lattice (so called reconstructive transformation) [4, 5]. TXRD experiment has shown that after approximately 1 hour the oxide is represented mainly by rutile modification (Figure 3.5) with crystallite size of more than 200 nm. After 5 hours of annealing no anatase phase was detected with XRD. High degree of crystallinity prevented us to estimate the kinetics of the crystallite growth for TiO_2 rutile phase. Accordingly, in Figure 3.6 the crystallite size evolution is shown only for SnO_2 phases in co-precipitated and mechanically mixed oxides.

The experimental values of crystallite sizes as a function of annealing time

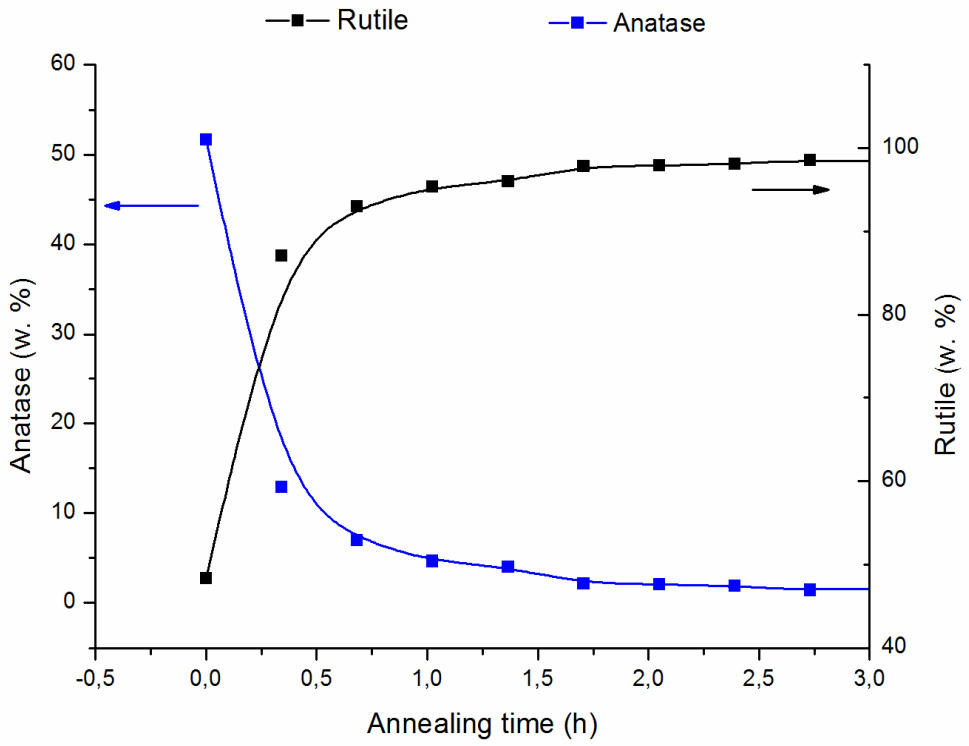

Fig. 3.5. Weight evolution of rutile and anatase phases in blank TiO_2

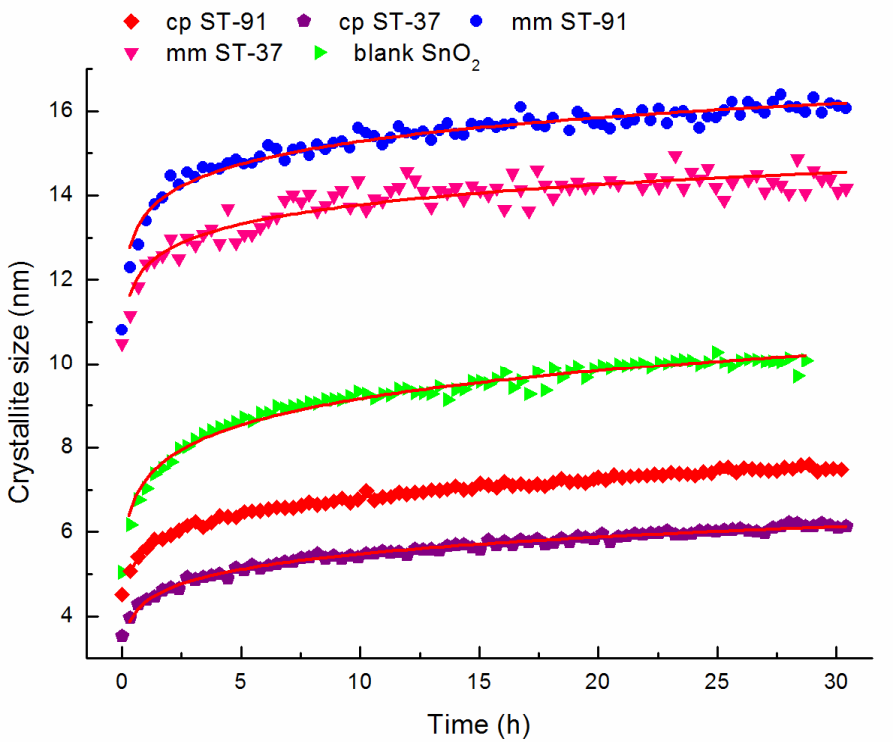

Fig. 3.6. Crystallite size evolution of SnO_2 phase during annealing at 700°C (red lines are fittings with the parabolic function

Table 3.1. Fitting parameters of the model (fitting error for the last decimal is given in parenthesis).

Material	*k*	*n*
SnO_2	7.24(4)	10.0(1)
cp ST-91	5.56(1)	11.3(1)
cp ST-73	4.35(1)	10.0(1)
mm ST-91	13.5(5)	20.0(1)
mm ST-73	12.3(8)	20.8(1)

were fitted with generalized parabolic model: $D(t)=kt^{1/n}$, where $D(t)$ is the crystallite size at time t, k is the temperature dependent constant and n is the growth exponent [6-8]. In spite of the fact that size-dependent impediment model was found to be more meaningful for nanocrystalline oxides [9-11], we used the former model because the fitting error of the latter was remarkably higher.

As it can be seen either from Figure 3.6 or from Table 2, the growth is remarkably higher in the case of mechanical mixtures. Most probably the anatase phase, which undergoes dramatic structural changes upon heating, evokes recrystallization phenomena in the rutile phase through interfacial contacts. Note, that rate constant and the mean crystallite sizes are higher for the mixture with low (10 w. %) TiO_2 content. On the other hand, the growth exponent is similar for both mechanical mixtures, indicating similar mechanisms of the crystallite growth.

Simultaneous precipitation of the oxides seems to effectively decrease growth rate of SnO_2 crystallites. The highest growth kinetics between co-precipitated materials was observed again for the system with 10 w.% TiO_2. The fact that both co-precipitated materials and blank SnO_2 manifest similar growth exponent suggests that presence of Ti^{4+} does not affect the growth mechanism in tin dioxide.

3.2. Characterization of SnO_2 nanowires in comparison with SnO_2 nanopowders

A typical SnO_2 nanowire obtained by the procedure described in 2.5.4 is presented at figure 3.7. Inserts show thickness of the nanowire, which varies from 74 to 85 nm at the presented section.

On the other hand, Figure 3.8 shows TEM image of SnO_2 nanopowder material obtained using the procedure 2.1.1. Average particle size amounts to 4-6 nm.

XRD spectra obtained by different methods (figure 3.9) show principal distinction of nanowires obtained by gas transport synthesis from precipitated nanopowder. Spectral band width at half-height characterizes the size of coherence area, which is determined by the crystallinity of the structure. Nanowires formed by vapour-liquid-solid mechanism have high and narrow peaks, testifying the monocrystalline structure. On the contrary, nanopowder has low and wide peaks, what testifies disordered structure.

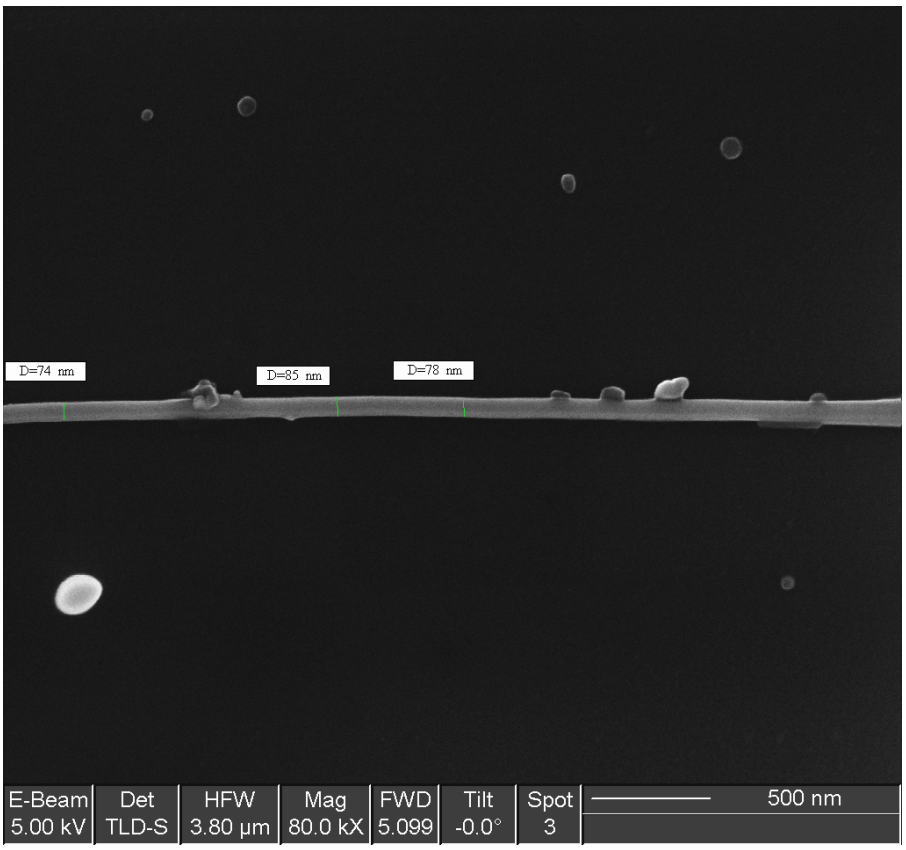

Figure 3.7. SEM image of SnO_2 nanowire after annealing

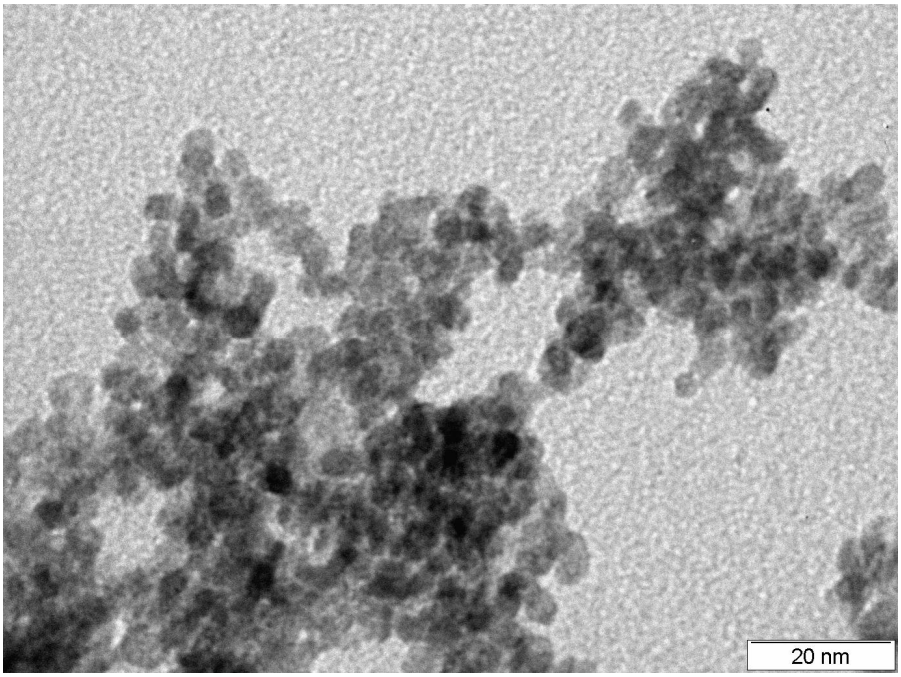

Figure 3.8. TEM image of SnO_2 nanopowder

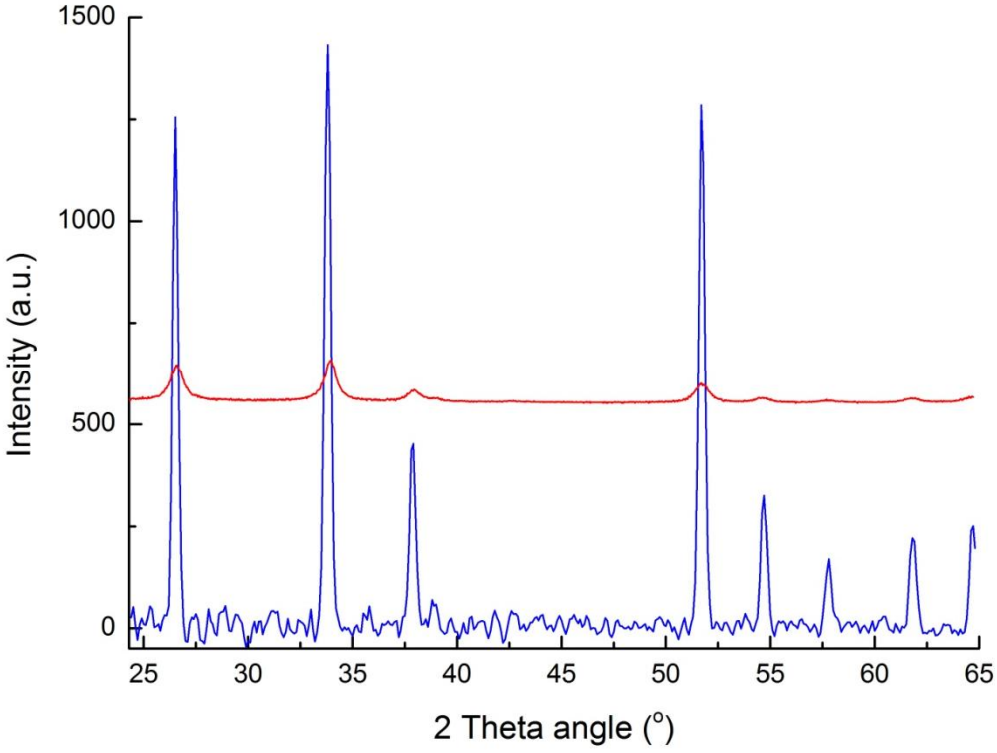

Figure 3.9. XRD spectra of SnO_2 nanopowder (red) and SnO2 nanowire (blue)

On the one hand, disordered structure of the powder should lead to the appearance of large number of adsorption centers on the surface of gas sensing material, what increases sensing response. On the other hand, monocrystallinity of the nanowires is a factor increasing the stability of the device.

References Chapter 3

[1] M.A. Henderson, The interaction of water with solid surfaces: fundamental aspects revisited, Surface Science Reports, 46 (2002) 5-308.

[2] A. Davydov, The Nature of Oxide Surface Centers, in: Molecular Spectroscopy of Oxide Catalyst Surfaces, John Wiley & Sons, Ltd, 2003, pp. 27-179.

[3] R.G. Pavelko, A.A. Vasiliev, E. Llobet, V.G. Sevastyanov, N.T. Kuznetsov, Selectivity problem of SnO_2 based materials in the presence of water vapors, Sens. Actuat. B, 170 (2012), 51–59.

[4] D. Hanaor, C. Sorrell, Review of the anatase to rutile phase transformation, Journal of Materials Science, 46 (2011) 855-874.

[5] P.I. Gouma, P.K. Dutta, M.J. Mills, Structural stability of titania thin films, Nanostructured Materials, 11 (1999) 1231-1237.

[6] C. Rock, K. Okazaki, Grain growth kinetics and thermal stability in a nanocrystalline multiphase mixture prepared by low-energy ball milling, NanoStructured Materials, 5 (1995) 657-671.

[7] G. Li, L. Li, J. Boerio-Goates, B.F. Woodfield, High Purity Anatase TiO_2 Nanocrystals: Near Room-Temperature Synthesis, Grain Growth Kinetics, and Surface Hydration Chemistry, Journal of the American Chemical Society, 127 (2005) 8659-8666.

[8] N. Audebrand, J.P. Auffredic, D. Louer, X-ray diffraction study of the early stages of the growth of nanoscale zinc oxide crystallites obtained from thermal decomposition of four precursors. General concepts on precursor-dependent microstructural properties, Chemistry of Materials, 10 (1998) 2450-2461.

[9] H. Natter, M. Schmelzer, M.S. Loffler, C.E. Krill, A. Fitch, R. Hempelmann, Grain-growth kinetics of nanocrystalline iron studied in situ by synchrotron real-time X-ray diffraction, Journal of Physical Chemistry B, 104 (2000) 2467-2476.

[10] A. Michels, C.E. Krill, H. Ehrhardt, R. Birringer, D.T. Wu, Modelling the influence of grain-size-dependent solute drag on the kinetics of grain growth in nanocrystalline materials, Acta Materialia, 47 (1999) 2143-2152.

[11] R.G. Pavelko, A.A. Vasiliev, F. Gispert-Guirado, N. Barrabes, J. Llorca, E. Llobet, V.G. Sevastyanov, Crystallite growth kinetics of highly pure nanocrystalline tin dioxide: The effect of palladium doping, Materials Chemistry and Physics, 121 (2010) 267-273.

4. Hydrogen detection with SnO_2-TiO_2 gas sensors

4.1. Hydrogen properties and application; motivation of sensors development

The properties of hydrogen gas are rather different from the properties of other combustible gases like alkanes or gasoline vapor. Its density amounts to approx. 0,09 kg/m^3 and its boiling point is 20.39 K. Moreover, hydrogen has high diffusion coefficient (0.61 cm^2/s in air) and buoyancy. Hydrogen mixes with air are flammable and combustible in the range 4–75%; they have a low minimum ignition energy (0.017 mJ) and high heat of combustion (142 kJ/g H_2), as well as a high burning velocity, detonation sensitivity and an ignition temperature of 560 ^oC. Hydrogen is also a strong reducing agent and has a high permeability through many materials.

Hydrogen is a colorless, odorless and tasteless gas and cannot be detected by human senses, therefore other means of its detection are required. Express and reliable hydrogen detection is essential to prevent the risk of explosion.

First hydrogen detectors were applied at filling stations for airships more than 100 years ago [1, 2]. However, up to now the tasks of selectivity, reliability, longevity improvement are still of current importance [3]. In chemical industry, detection of hydrogen content in gas phase is an important task. In such processes like synthesis of ammonia and methanol, hydration of hydrocarbons, desulphurization of petroleum products and production of rocket fuels there is a need in on-line precise monitoring of hydrogen concentration for maintaining the proper conditions of synthesis process. Another reason for hydrogen detection in industry is that it can act as a pollutant. For example, in metallurgical processes, during melting of aluminium, hydrogen can be formed as a result of interaction of aliminium and water [4]. After that, hydrogen remains dissolved in the melt, what leads to so-called hydrogen embrittlement. Therefore, its concentration must be monitored during welding and galvanic plating.

In nuclear industry, monitoring of hydrogen concentration is essential from the point of view of nuclear reactor safety. Hydrogen can be formed in radioactive waste tanks during plutonium reprocessing, through the radiolysis of water or via the unwanted reaction of water with high temperature reactor core and cladding materials uranium oxide, zirconium. The latter process is called zirconium-steam reaction. This is an exothermic chemical reaction between zirconium and water vapor which runs at high temperatures. During Three Mile Island accident, non-condensing gases, primary hydrogen was formed in a result of zirconium-steam reaction, accumulated inside the equipment, prevented natural circulation of the coolant, what finally determined the severe consequences of the accident. Zirconium-steam reaction with the formation of big amounts of hydrogen also took place during Fukushima Daiichi nuclear disaster. Explosions of hydrogen lead to releasing substantial amounts of radioactive materials. After this disaster, passive catalytic hydrogen recombiners are obligatory included in the set of reactor equipment. These devices provide reduction of hydrogen concentration during accident accompanying by its liberation. Recombiners don't need energy sources or a command to turn on; after the achievement of a certain hydrogen concentration (0.5 – 1.0%), the process of its absorption by recombiners is started automatically.

Another area of possible hydrogen sensors application is coal mining. The sources of hydrogen in coal mines are methane or coal-dust explosions as well as spontaneous heating and low-temperature oxidation of coal [5]. These processes can be detected by monitoring of hydrogen concentration changes in the mine atmosphere.

Hydrogen is used as a marker compound for early fire detection [6, 7]. In one of the early works, the possibility of fire detection by SnO2 semiconductor gas sensors has been investigated in the laboratory and in a full-scale fire experiment using a wooden house [8]. Four types of gas sensors and conventional fire detectors are compared with each other. The H2 sensor was able to detect the fire a few minutes earlier than conventional fire detectors.

One more area, where hydrogen concentration measurement is needed, is silicon technology, for which gases such as silanes and nitrogen must be produced with very high purity. Hydrogen is also a contaminant in the production of gases for the lighting industry, it must be quantified during the production of krypton, xenon and neon.

Very important is detection of hydrogen leakages. Leaks may appear at gas supply tubes of in the cooling systems of turbine generators. In process plants the presence of hydrogen can indicate corrosion. Hydrogen sensors play an important role in ensuring the security of aerospace operations. Liquid hydrogen is used in bulk quantities as a fuel in space applications; hydrogen sensors are used for leak detection during shuttle launches.

In biomedical applications hydrogen serves as an indicator for the number of diseases [9]. Breath hydrogen is an important, clinically relevant parameter used as an indicator of lactose intolerance [11-13], fructose malabsorption [14-18], microbial activity [19], bacterial growth [20-22], fibromyalgia [23], diabetic gastroparesis [24-26], and neonatal necrotizing enterocolitis [27-31].

Hydrogen is an energy carrier and can contribute to overcoming the problems of dwindling fossil fuel reserves, energy supply security and global warming. Ongoing research, development and as yet small-scale deployment of hydrogen technologies seek to realize this potential. In this emerging hydrogen economy, the detection of hydrogen leaks and the measurement of hydrogen concentration are necessary during production, storage, transportation and use in both stationary and mobile applications. Sensors will therefore be used for safety monitoring of hydrogen production plants, pipelines, storage tanks, refuelling stations and automotive vehicles [1].

Hydrogen concentration in ambient can be measured by such methods as chromatography, spectrometry, specific ionization sensors. Despite a number of advantages, these methods are not suitable for, e.g., detection of hydrogen leakages

of real-time monitoring of its concentration due to the bulk dimensions of the devices used.

Hydrogen sensors are transducer devices that detect hydrogen gas molecules and produce an electrical signal with a magnitude proportional to the hydrogen gas concentration [32]. A lot of research is ongoing to continuously improve sensitivity, selectivity, response time and reliability in addition to reducing sensor size, cost and power consumption. These demands on hydrogen sensors can be summarized [11, 35–37] as follows:

Reliability (uncertainty <5–10% of signal); stability and low noise; robustness, low sensitivity to environmental parameters; fast response and recovery time (<1 s); low cross sensitivity (e.g. hydrocarbons, CO, H2S); long life time (>5 years); low power consumption (<100 mW); low cost (<100 D per system); small size; simple operation and maintenance with long service interval; simple system integration and interface.

4.2. Results of hydrogen gas sensing experiments

As it was shown in paragraph 1.3.1.3, the use of double oxides is a valid strategy for improvement of wide band gap oxides sensing characteristics. Sensors based on the materials described in paragraph 2.1.1 and 2.3.1 were characterized in a number of gas sensing experiments.

Let us list again the notations of the materials used for sensors fabrication:

cp ST-91, cp ST-73 – materials, co-precipitated from colloid solution. Contain accordingly 10 mol.% and 30 mol.% of titanium dioxide;

mm ST-91, cp ST-73 – materials, obtained by mechanical mixing of titania and tin dioxide by grinding in a mortar. Contain accordingly 10 mol.% and 30 mol.% of titanium dioxide.

Figure 4.1 summarizes sensor tests results obtained at different temperatures. As it can be seen, both mechanical mixing and co-precipitation increase signals towards 20 ppm H_2. The highest increase is observed for the co-precipitated

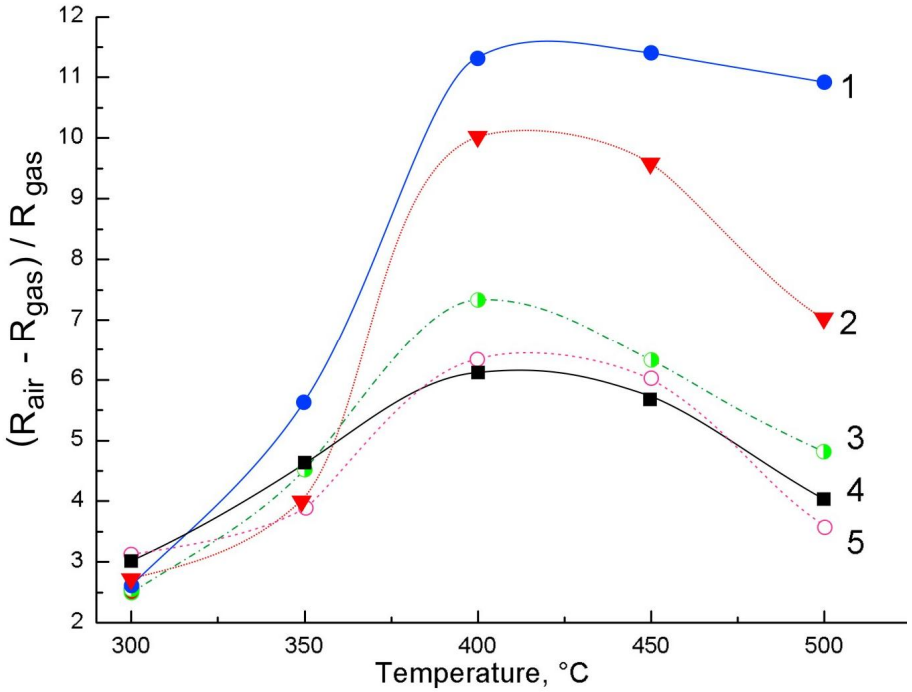

Figure 4.1. Signals towards 20 ppm H_2 in air at five different operating temperatures. Notation: 1 – cp ST-73, 2 – cp ST-91, 3 – mm ST-73, 4 – SnO2, 5 – mm ST-91

materials and for the highest content of TiO_2 at that. The same tendency is seen for the mixed oxides: addition of 30% TiO_2 enhances the signal more compared to the 10% TiO_2. The classic volcano-shaped curve of blank SnO_2 has remarkably changed upon co-precipitation. The high-temperature side of the curve becomes broader and intense. However, for mixed and co-precipitated materials the signal maximum is still observed at 400 ^oC, which is close to the blank material. This suggests that after doping the active surface species first of all are more numerous (signal is higher) and slightly different in their nature (high-temperature broadening).

Figure 4.2 gives typical sensor responses to 20 ppm H_2 in air at the temperature

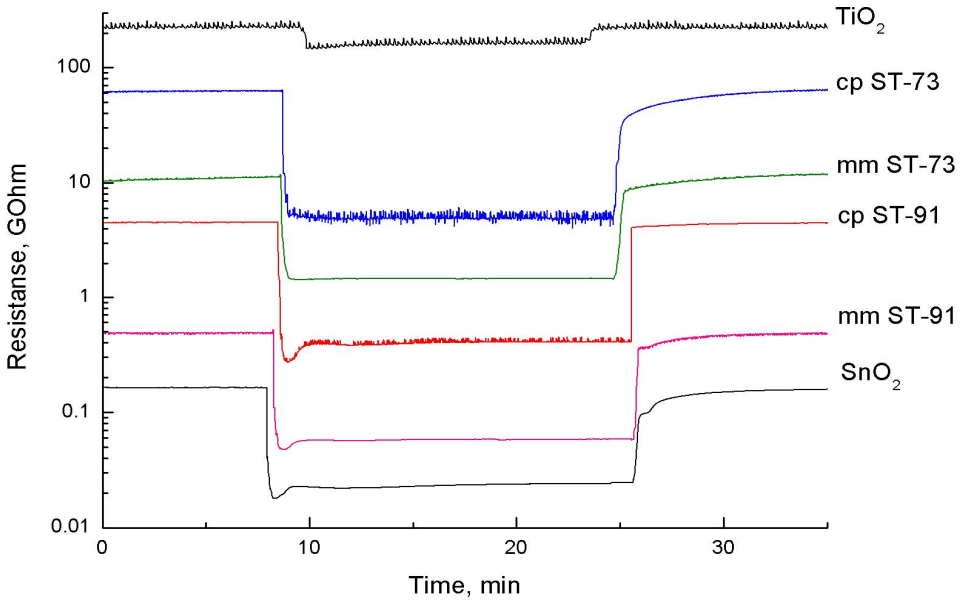

Fig.4.2. Typical responses towards 20 ppm H_2 in air

of signal maximum – 400°C. The sheet resistance of the co-precipitated materials gradually increases with the increase of TiO_2 content. Same phenomenon is observed for the mixed SnO_2 and TiO_2. However, their resistance is ca. 10 times lower compared to the co-precipitated materials, which is probably related to the percolation effect: in the case of mechanical mixtures the carriers flow predominantly trough conductive SnO_2 grains, while in the co-precipitated oxides the SnO_2 grains are doped with TiO_2 and the conductive grains of blank SnO_2 are scarce. The sensors manifest rather similar response times, suggesting similar adsorption kinetics for the materials in question. The response time (t_{90}) for all

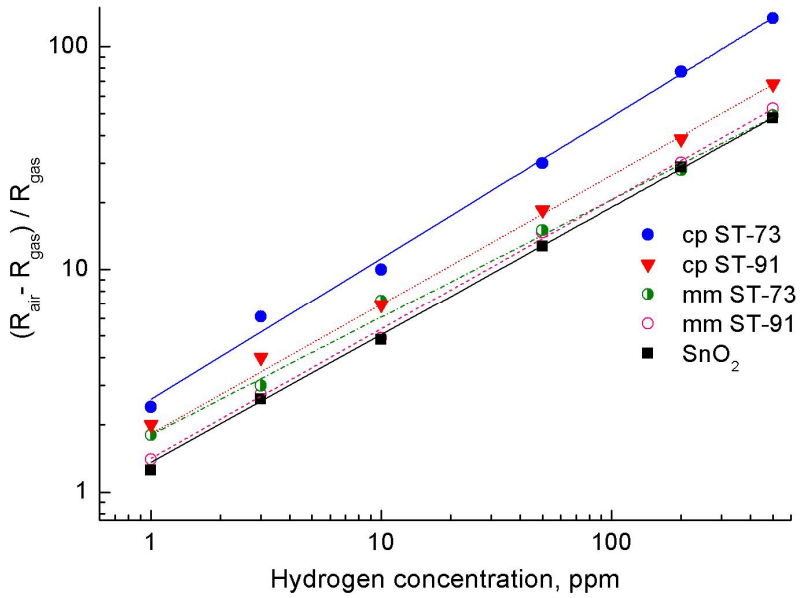

Fig. 4.3. Calibration curves for the materials in question

sensors ranges from 12 to 14 s, while recovery time (t_{90}) is between 200 and 360 s for all sensors except cp ST-91 and TiO_2. The recovery time for the latter materials was found about 30 seconds. Blank SnO_2, mm ST-91 and cp ST-91 show very similar sensitivity with concentration exponents 0.58-0.59 (Fig. 4.3). The lowest value – 0.53 – was found in the case of mm ST-73, while the highest – 0.63 - for cp ST-73.

Higher signals and sensitivity of the co-precipitated materials compared to the blank SnO_2 do not seem to be associated with the different surface chemistry of hydrogen interaction, since temperature of signal maximum for both materials is close to the blank oxide (however, evidently, new active surface species have appeared after doping, resulting in high signals at 450 and 500 ^{o}C, see figure 4.1). Comparing surface hydroxyls, we have shown that the dominant type is similar for all materials. The difference was found only in higher amount of hydroxyls on co-precipitated materials compared to the blank SnO_2 (see paragraph 3.1).

Since blank TiO_2 manifested poor structural stability upon heating, this material will not be compared with the other ones. However, it is important to mention that its sensitivity towards H_2 was found to be very low (ca. 1 for 20 ppm H_2, see Figure

7a), which suggests that SnO_2 plays the dominant role in the sensing phenomenon of the mixed materials.

Also sheet resistance of the co-precipitated materials is higher, meaning lower concentration of charge carrier. Since sensor signal *S* was defined as $(R_{air}-R_{gas})/R_{gas}$ and $R=1/q\ \mu\ n$, where *q* is the carrier charge, μ is the carrier mobility and *n* is the carrier concentration, we can write following expression, implying that charge and mobility of carriers are constant in air and in target gas:

$$S=\frac{n_{gas}}{n_{air}}-1=\frac{n_{air}+e_{gas}}{n_{air}}-1=\frac{e_{gas}}{n_{air}}$$

where n_{air} and n_{gas} are the carrier concentration in contact with air and target gas, e_{gas} is the amount of generated carriers due to interaction between the target gas and the semiconductor. As n_{air} decreases (resistance increases) and other parameters like surface area, surface chemical potential, target gas and its concentration maintain unchanged, this will increase the sensor signal. The latter of course is a hypothetical approximation, helping however estimate possible electrical nature of the increased sensor signals in the case of co-precipitated materials.

Another reason for higher signals of the co-precipitated materials can also come from surface area. These materials manifested better thermal stability compared to the blank oxide. Therefore materials are expected to be less aggregated after annealing on the substrate.

The case of mechanically mixed oxides is quite ambiguous. The TiO_2 additive increases modestly signal towards 1-50 ppm H_2. At higher H_2 concentrations this advantage disappears, leading to the same signal level as for blank SnO_2. Their poor thermal stability evidently results in lower surface area compared to the

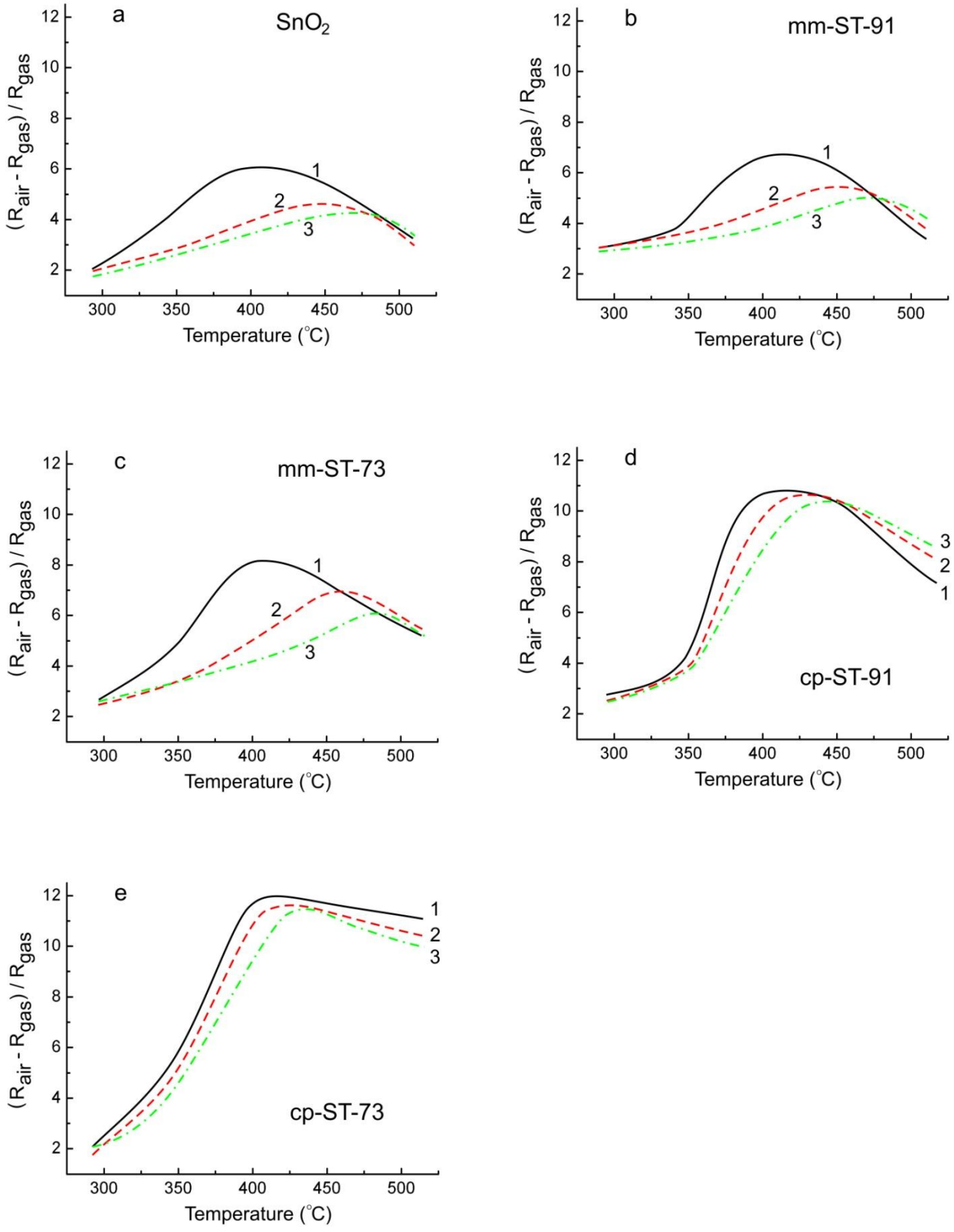

Figure 4.4. Sensor response to 20 ppm H_2 at RH = 0 (curve 1), 30% (curve 2), 80% (curve 3)

blank oxide. However, the signals are very close for both types of materials. It seems that even there is evidence of interphase interaction between blank oxides and new interphase forms upon thermal treatment (leading to remarkable crystallite growth of SnO_2), it has negligible effect on sensing properties of SnO_2.

Figure 4.4 shows sensors responses to 20 ppm of hydrogen in air with different humidity. The materials show two general types of signal changes due to water vapor appearance: sensors with bulk SnO_2 and SnO_2-TiO_2 mechanical mixtures sensing layers manifest significant decrease in sensor signal in comparison with dry synthetic air, while the signal change of co-precipitated materials is much lower. This fact confirms one more time that the sensing mechanism of SnO_2-TiO_2 mechanical mixtures probably is determined mainly by tin dioxide, while the addition of TiO_2 to SnO_2 by co-precipitation results in formation of the material with rather different sensing properties.

References Chapter 4

[1] T. Hübert, L. Boon-Brett, G. Black, U. Banach. Hydrogen sensors – A review. Sensors and Actuators B 157 (2011) 329– 352

[2] Saito T., Yamashita J., Ishiwatari Y., Oka. Y. Advances in Light Water Reactor Technologies. — New York, Dordrecht, Heidelberg, London: Springer, 2011. — 295 p.

[3] Gerhard Müller, Sebastian Beer, Sumit Paul, Andreas Helwig. Novel chemical sensor applications in commercial aircraft. Procedia Engineering Volume 25, 2011, Pages 16–22 Eurosensors XXV

[4] C. Schwandt, D.J. Frey, Hydrogen sensing in molten aluminum using a commercial electrochemical sensor, Ionics 6 (2000) 3–4.

[5] M.P. Brungs, et al., The evaluation of hydrogen detectors for use in coal mines, J. Inst. Energy 65 (1992) 66–69.

[6] Misawa T., Nanto H., Kasahara H., Iwasaki Y. Odor sensor system for early fire detection and its application to utility mobile robot. Sensors and materials 2005; 17:7 413-421.

[7] Wolfgang Krüll, Robert Tobera, Ingolf Willms, Helmut Essen, Nora von Wahl. Early Forest Fire Detection and Verification using Optical Smoke, Gas and Microwave Sensors. Procedia Engineering Volume 45, 2012, Pages 584–594. 2012 International Symposium on Safety Science and Technology

[8] Taro Amamoto, Katsuyuki Tanaka, Kei Takahata, Shunji Matsuura, Tetsuro Seiyama. A fire detection experiment in a wooden house by SnO2 semiconductor gas sensors. Sensors and Actuators B: Chemical Volume 1, Issues 1–6, January 1990, Pages 226–230

[9] C.A. Grimes, et al., A sentinel sensor network for hydrogen sensing, Sensors 3 (2003) 69–82.

[10] ,

[11] Rizkalla, S.W.; Luo, J.; Kabir, M.; Chevalier, A.; Pacher, N.; Slama, G. Chronic consumption of fresh but not heated yogurt improves breath-hydrogen status and short-chain fatty acid profiles: a controlled study in healthy men with or without lactose maldigestion. American Journal Of Clinical Nutrition 2000, 72 (6), 1474-1479.

[12] Chong, S.K.F.; Ramadan, A.B.; Livesey, E.; Wood, G. The use of a portable breath hydrogen analyser in screening for lactose intolerance in paediatric patients with chronic abdominal pain or chronic diarrhoea. Gastroenterology 2002, 122 (4), M1827 Suppl. 1 APR.

[13] Kanabar, D.; Randhawa, M.; Clayton, P. Improvement of symptoms in infant colic following reduction of lactose load with lactase. Journal of Human Nutrition and Dietetics 2001, 14, 359-363.

[14] Li, D.Y.; Barnes, Y.; Cuffari, C. Who should request a breath hydrogen test? A five year feasibility, sensitivity of clinical suspicion and cost-effectiveness analysis. Gastroenterology 2002, 122, W1144 Suppl. 1.

[15] Duro, D.; Rising, R.; Cedillo, M.; et al. Association between infantile colic and carbohydrate malabsorption from fruit juices in infancy. Pediatrics 2002, 109(5), 797-805.

[16] Moukarzel, A.A.; Lesicka, H.; Ament, M.E. Irritable bowel syndrome and nonspecific diarrhea in infancy and childhood - Relationship with juice carbohydrate malabsorption. Clinical 2002, 41, 145-150.

[17] Lebenthal-Bendor, Y.; Theuer, R.; Lebenthal, A.; Tabi, I.; Lebenthal, E. Malabsorption of modified food starch (acetylated distarch phosphate) in normal infants and in 8-24-month-old toddlers with non-specific diarrhea, as influenced by sorbitol and fructose. Acta Paediatrica 2001, 90(12), 1368-1372.

[18] Ledochowski, M.; Widner, B.; Murr, C.; Sperner-Unterweger, B.; Fuchs, D. Fructose malabsorption is associated with decreased plasma tryptophan. Scandinavian Journal Gastroenterology 2001, 4, 367-371.

[19] Backus, R.C.; Puryear, L.M.; Crouse, B.A.; Biourge, V.C.; Rogers, Q.R. Breath hydrogen concentrations of cats given commercial canned and extruded diets

indicate gastrointestinal microbial activity vary with diet type. Journal of Nutrition 2002, 6, 1763S-1766S Suppl. 2.

[20] Riordan, S.M.; McIver, C.J.; Duncombe, V.M.; Thomas, M.C.; Bolin, T.D. Evaluation of the rice breath hydrogen test for small intestinal bacterial overgrowth. American Journal of Gastroenterology 2000, 95(10), 2858-2864.

[21] Bauer, T.M.; Schwacha, H.; Steinbruckner, B.; Brinkmann, F.E.; Ditzen, A.K.; Kist, M.; Blum H.E. Diagnosis of small intestinal bacterial overgrowth in patients with cirrhosis of the liver: performance of the glucose breath hydrogen test. Journal of Hepatology 2000, 33(3), 382-386.

[22] Funayama, Y.; Sasaki, I.; Naito, H.; Fukushima, K.; Shibata, C.; Masuko, T.; Takahashi, K.; Ogawa, H.; Sato, S.; Ueno, T.; Noguchi, M.; Hiwatashi, N.; Matsuno, S. Monitoring and antibacterial treatment for postoperative bacterial overgrowth in Crohn's disease, Diseases of The Colon & Rectum 1999, 42 (8), 1072-1077.

[23] Pimentel, M.; Chow, E.J.; Lin, H.C. Comparison of peak breath hydrogen production in patients with irritable bowel syndrome, chronic fatigue syndrome and fibromyalgia. Gastroenterology 2000, 118(4), 2141 Part 1 Suppl. 2.

[24] Burge, M.R.; Tuttle, M.S.; Violett, J.L.; Stephenson, C.L.; Schade, D.S. Breath hydrogen testing identifies patients with diabetic gastroparesis. Diabetes Care 2000, 23(6), 860-861.

[25] Chiloiro, M.; Darconza, G.; Piccioli, E.; De Carne, M.; Clemente, C.; Riezzo, G. Gastric emptying and orocecal transit time in pregnancy. Journal of Gastroenterology 2001, 36(8), 538-543.

[26] Stordal, K.; Nygaard, E.A.; Bentsen, B. Organic abnormalities in recurrent abdominal pain in children. Acta Paediatrica 2001. 90(6), 638-642.

[27] Bisquera, J.A.; Cooper, T.R.; Berseth, C.L. Impact of necrotizing enterocolitis on length of stay and hospital charges in very low birth weight infants. Pediatrics 2002,109, 423-428.

[28] Engel, R.R.; Virnig, N.L. Origin of mural gas in necrotizing enterocolitis. Pediatric Research 1973, 7, 292A.

[29] Godoy, G.; Truss, C.; Philips, J.; et al. Breath hydrogen excretion in infants with necrotizing enterocolitis. Pediatric Research 1986, 20, 348A.

[30] Garstin, W.I.H.; Boston, V.E. Sequential assay of expired breath hydrogen as a means of predicting necrotizing enterocolitis in susceptible infants. Pediatric Research 1987, 22, 208-210.

[31] Cheu, H.W.; Brown, D.R.; et al. Breath hydrogen excretion as a screening test for the early diagnosis of necrotizing enterocolitis. American J. Diseases of Children 1989. 143, 156-159.

[32] A. Hulanicki, S. Glab, F. Ingman, Chemical sensors definitions and classifica- tion, Pure Appl. Chem. 63 (1991) 1247–1250.

[33] G.W. Hunter, A survey and analysis on commercially available hydrogen sensors, NASA Technical Memorandum 105878, Nov. 1992.

[34] V.A. Aroutiounian, Hydrogen detectors, Int. J. Altern. Energy Ecol. 3 (2005) 21–31.

[35] http://www.hysafe.org/download/1200/BRHS_Chap5_V1p2.pdf Accessed 15 December 2010.

[36] W.J. Buttner, et al., An overview of hydrogen safety sensors and requirements, Int. J. Hydrogen Energy (2010), doi:10.1016/j.ijhydene.2010.04.176.

[37] L. Boon-Brett, J. Bousek, G. Black, P. Moretto, P. Castello, T. Hübert, U. Banach, Identifying performance gaps in hydrogen safety sensor technology for automotive and stationary applications, Int. J. Hydrogen Energy 35 (2010) 373–384

5. Hydrogen sulfide detection with single-nanowire device

5.1. Hydrogen sulfide properties; motivation for sensors development

Hydrogen sulfide (H_2S) is a colorless gas heavier than air. It is very poisonous, corrosive, flammable, and explosive. It is widely used in chemical industry for synthesis, production of sulfur, sulfuric acid. It is thermally instable, at temperature above 400 ^oC decomposes to sulfur and hydrogen. Unlike water molecules, hydrogen atoms of H_2S don't form strong hydrogen bonds, therefore hydrogen sulfide is a gas.

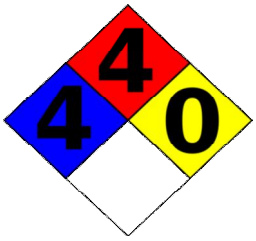

Figure 5.1. Hydrogen sulfide marking according to NFPA 704

Hydrogen sulfide mixtures with air are explosive in a range 4.3–46% of H_2S.

Hydrogen sulfide is considered as a broad-spectrum poison with more pronounced nerve action. The toxicity of H_2S is comparable with that of hydrogen cyanide or carbon monoxide. It forms a complex bond with iron in the mitochondrial cytochrome enzymes, thus preventing cellular respiration.

Since hydrogen sulfide occurs naturally in the body, the environment and the gut, enzymes exist in the body capable of detoxifying it by oxidation to sulfate. Hence, low levels of hydrogen sulfide may be tolerated indefinitely.

At some threshold level, believed to average around 300–350 ppm, the oxidative enzymes become overwhelmed. Many personal safety gas detectors, such as those used by utility, sewage and petrochemical workers, are set to alarm at as low as 5 to 10 ppm and to go into high alarm at 15 ppm.

Exposure to lower concentrations can result in eye irritation, a sore throat and cough, nausea, shortness of breath, and fluid in the lungs (pulmonary edema). Long-term, low-level exposure may result in fatigue, loss of appetite, headaches, irritability, poor memory, and dizziness. Short-term, high-level exposure can induce immediate collapse.

0.47 ppb is the odor threshold and 0.0047 ppm is hydrogen sulfide recognition threshold [1]; 10 ppm is the OSHA permissible exposure limit (PEL) [2]; 10–20 ppm is the borderline concentration for eye irritation; 20 ppm is the acceptable ceiling concentration established by OSHA [2]; 50 ppm is the acceptable maximum peak above the ceiling concentration for an 8 hour shift, with a maximum duration of 10 minutes [2]; at 100–150 ppm the olfactory nerve is paralyzed after a few inhalations, and the sense of smell disappears, often together with awareness of danger [3,4]; concentrations over 1000 ppm cause immediate collapse.

5.2. Comparison of sensors based on sol-gel materials and nanowires

Semiconductor sensor action is based as a rule on heterogeneous catalysis of chemical processes, therefore the surface to volume ratio of gas sensing materials is an important characteristic determining sensitivity. Traditionally, quasi-0-dimentional (i.e., spherical) nanoobjects were used in order to create highly dispersive materials. Their agglomeration at temperature close to the melting point leads to the formation of a material with high surface to volume ratio. In such methods as magnetron sputtering, laser ablation and pulverization, layer-by-layer nanoparticles deposition is used with their subsequent adhesion to the substrate and to the previously formed material. Sol-gel process supposes synthesis of nanopowder which consists of spherical nanoparticles, preparation of the paste from this powder and its deposition and annealing.

The development of sol-gel synthesis of highly dispersive semiconductor materials is slightly retarded recently, because the researchers have now approached to the scopes of this method and achieved the optimal dispersivity as well [5]. In this connection, the interest to the development of the devices based on nanowires, i.e., quasi-1-dimentional objects, have increased. Their surface to volume ratio is as high as in the case of nanopowders, obtained on the basis of spherical nanoparticles.

Nanowires were synthesized at 1960s, but their wide application started only in the beginning of 21st century, when the technology advancement required the creation of a wide range of nanomaterials, and new methods of these materials treatment appeared. The basic method of nanowire synthesis was developed in details in classical work of R. Wagner and W. Ellis [6]. Recently, with the use of this method SnO_2, In_2O_3, WO_3, ZnO and other oxides nanowires been obtained [6-10]. Liquid phase synthesis methods are also widely implemented [11-14].

The use of metal oxide nanowires as sensing elements of gas sensors continues in two directions. First direction supposes the use of a large quantity of nanowires. For example, nanowires can be growed on the surface of metal electrodes deposited on a dielectric substrate, wherein random electrical contact between wires located on different electrodes takes place. The contact of each pair of nanowires is not stable, but considering their large number, completely stable electrical contact is formed. Sensors based on such systems show high sensitivity [15-25]. Hierarchical structures with SnO_2 nanowires covered with additional nanoscale objects can be used for the improvement of electrical contact [16,22,23].

Second direction of nanowire sensors development is manufacturing of electrical contacts for individual nanowires [26-35]. These contacts can be made by the means of photolithography, but more often focused ion beam (FIB) is used for this purpose. This approach has a number of advantages. First, a reliable electrical contact between nanowires and electrodes is secured. Second, the possibility for manufacturing of devices with ultralow energy consumption opens up.

In the case of the use of an individual nanowire, two pairs of electrodes are deposited onto the nanowire. Outer pair is used for the applying of heating electric potential, and inner pair is used for the measurement of electrical resistance.

In spite of large number of works dedicated to the use of nanowires as conductometric gas sensors, they were not compared in details with classical semiconductor sensors manufactured by the means of sol-gel method. The present

work aimed to compare the characteristics of sensing devices based on SnO_2, prepared by different methods, at hydrogen sulfide detection.

5.3. Results and discussion

The performance of sensors based on blank SnO_2 and SnO_2 doped with various compounds was studied. The compositions of sensing layers were as follows: SnO_2 + 3%CuO, SnO_2 + 3%Cu, SnO_2 + 2%CuO + 2%Au, SnO_2 + 3%Pt, SnO_2 + 3%Pd, SnO_2 + 2%Pt + 2%Pd (all proportions given in weight %).

Sensors signals towards various concentrations of hydrogen sulfide at temperature 200 ^{o}C (figure 5.2) and sensors response towards 10 ppm of H_2S at various temperatures (figure 5.3) were measured.

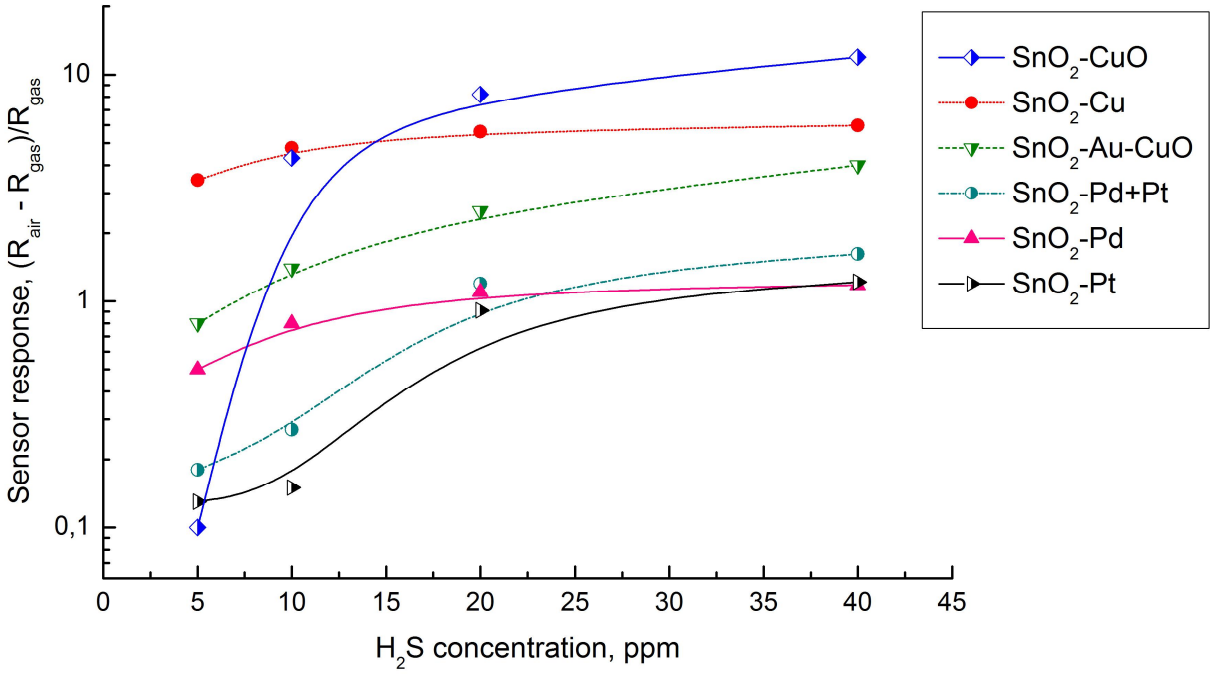

Figure 5.2. Sensors signals towards various H_2S concentrations. Temperature = 200 ^{o}C

The obtained results show significant increase of sensor response due to doping with copper and copper oxide. On the surface of this sensing layer takes place reversible phase transition with copper sulfide formation:

$$CuO + H_2S \xleftrightarrow[T^0C]{} CuS + 2H_2O \quad (1)$$

Elecrtophisical characteristics of copper sulfide are essentially different from the characteristics of copper oxide, what leads to significant increase of response.

Temperature dependence demonstrates consistent decrease of sensing signal with temperature increase, what is related with decrease of hydrogen sulfide sorption.

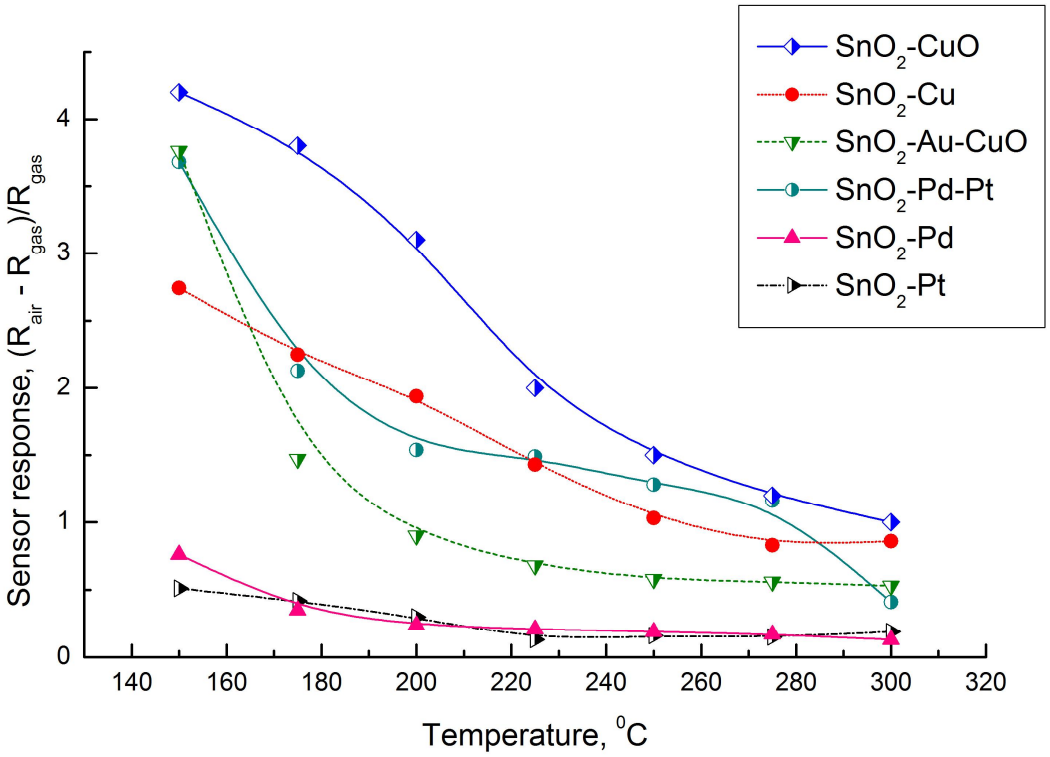

Figure 5.3. Sensor signal at various temperatures. H_2S concentration = 10 ppm.

Optimization of the sensing material dispersivity and choose of a suitable doping compound allowed to detect hydrogen sulfide at concentration as low as 1 ppm.

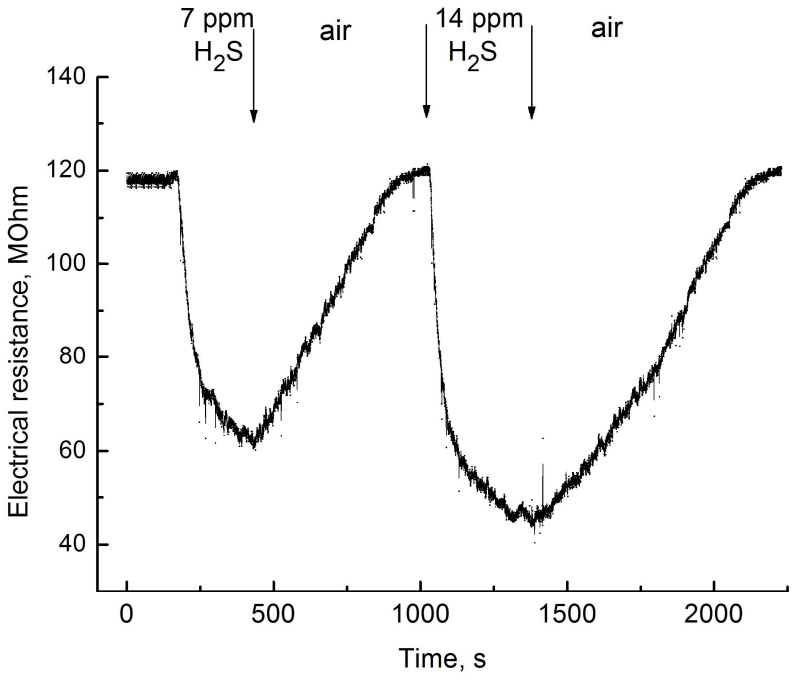

Figure 5.4. Typical signal of a single nanowire sensing device

Hydrogen sulfide various concentrations were measured with a sensing device based on a single nanowire (figure 5.4).

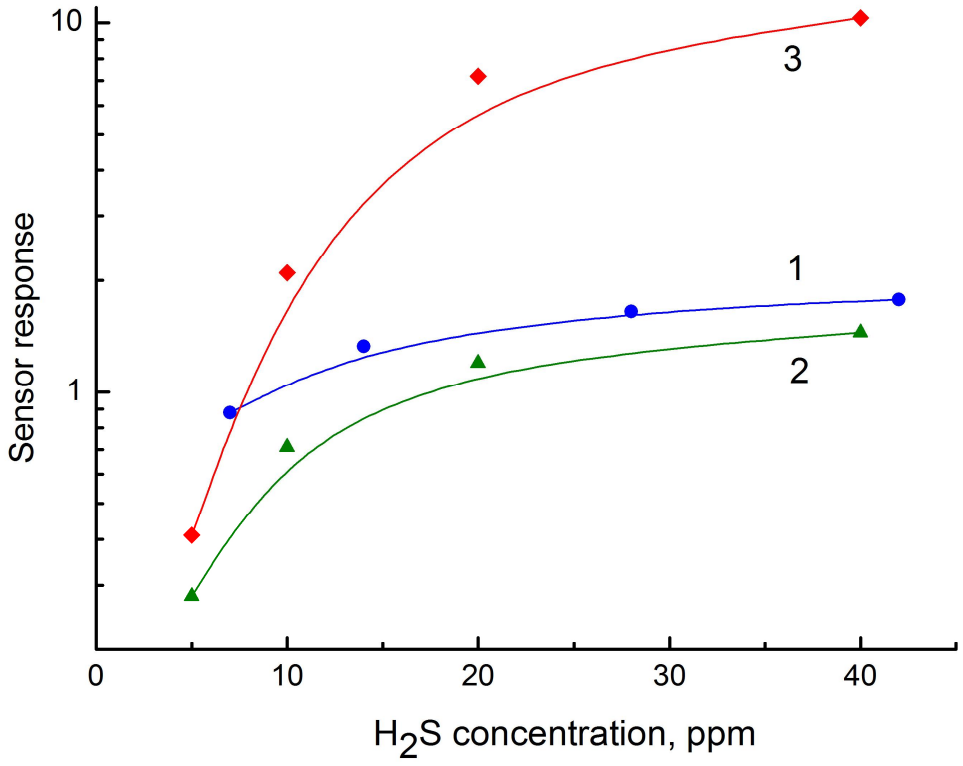

Fig. 5.5. SnO_2 nanowire (1), blank sol-gel SnO_2 (2), sol-gel SnO_2 with 3 % CuO (3)

Performance of both the single nanowire devices and sensors produced by sol-gel method were investigated at the same temperature (200°C).

Saturation determining hydrogen sulfide by the sensor based on individual nanowire is observed (figure 5.5). On the other hand, sensors fabricated by sol-gel method of undopped tin dioxide showed lower responses in comparison with the single nanowire device. It is found that sensors doped with copper oxide demonstrate higher sensitivity. Therefore, it can be concluded that a controlled doping of the nanowires with copper oxide is a valid strategy to enhance their H_2S sensing characteristics.

References Chapter 5

[1] Iowa State University Extension (May 2004). "The Science of Smell Part 1: Odor perception and physiological response". PM 1963a.

[2] Agency for Toxic Substances and Disease Registry (July 2006). "Toxicological Profile For Hydrogen Sulfide". p. 154.

[3] USEPA; Health and Environmental Effects Profile for Hydrogen Sulfide p.118-8 (1980) ECAO-CIN-026A.

[4] Zenz, C., O.B. Dickerson, E.P. Horvath. Occupational Medicine. 3rd ed. St. Louis, MO., 1994, p.886.

[5] G. Sakai, N. Matsunaga, K. Shimanoe, N. Yamazoe, Theory of gas-diffusion controlled sensitivity for thin film semiconductor gas sensor, Sens. Actuators B 80 (2001) 125–131.

[6] R. Wagner, W. Ellis, Vapor liquid solid mechanism of single crystal growth, Appl. Phys. Lett. 4 (1964) 89–90.

[7] E. I. Givargizov, Oriented growth of whiskers of AIIIBV compounds by VLS-mechanism, Kristall und Technik 10 (1975) 473–484.

[8] Z.L. Wang, Functional oxide nanobelts: material, properties and potential application in nanosystems and biotechnology, Annu. Rev. Phys. Chem. 55 (2004) 159-196.

[9] Z. Zhu, T.-L. Chen et al., Zinc oxide nanowires grown by vapor-phase transport using selected metal catalysts: A comparative study, Chem. Mater. 17 (2005) 4227-4234.

[10] S. Kar, B. N. Pal et al., One-dimensional ZnO nanostructure arrays: synthesis and characterization, J. Phys. Chem. B 110 (2006) 4605-4611.

[11] Y. Chang, H.C. Zeng, Controlled synthesys and self-assembly of single-crystalline CuO Nanorods and Nanoribbons, Crystal Growth&Design, 2 (2004) 397-402.

[12] S.K.N. Ayudhya, P. Tonto et al., Solvothermal synthesis of ZnO with various aspect ratios using organic solvents, Crystal Growth&Design, 11 (2006) 2446-2450.

[13] Y. Wang, G. Cao, Synthesis and enhanced intercalation properties of nanostructured vanadium oxides, Chem. Mater., 18 (2006) 2787-2804.

[14] Y. Tong, Y. Liu, Growth of ZnO nanostructures with different morphologies by using hydrothermal technique, J. Phys. Chem B, 110 (2006) 20263-20267.

[15] H. W. Kim, S.-W. Choi et al., Enhanced sensing performances of networked SnO2 nanowires by surface modification with atmospheric pressure Ar–O2 plasma, Sensors and Actuators B, 177 (2013), 654-658.

[16] N. D. Khoang, D. D. Trung et al., Design of SnO2/ZnO hierarchical nanostructures for enhanced ethanol gas-sensing performance, Sensors and Actuators B, 174 (2012) 594-601.

[17] S.-H. Jung, S.-W. Choi et al. Fabrication and properties of trench-structured networked SnO2 nanowire gas, Sensors and Actuators B, 171-172 (2012) 672-678.

[18] I.-S. Hwanga, S.-J. Kima et al., Large-scale fabrication of highly sensitive SnO2 nanowire network gas sensors by single step vapor phase growth, Sensors and Actuators B, 165 (2012) 97-103.

[19] E. Comini, G. Sberveglieri et al., Metal oxide nanowires as chemical sensors, MaterialsToday 13 (2010) 36–44.

[20] N.M. Shaalana, T. Yamazakia, T. Kikutaa, NO2 response enhancement and anomalous behavior of n-type SnO2 nanowires functionalized by Pd nanodots, Sensors and Actuators B, 166–167 (2012) 671– 677.

[21] C.-H. Kwak, H.-S. Woo, Jong-Heun Lee, Selective trimethylamine sensors using Cr2O3-decorated SnO2 nanowires, Sensors and Actuators B, 204 (2014) 213-238.

[22] S.-W. Choi, A.Katoch et al. Synthesis and gas sensing performance of ZnO–SnO2 nanofiber–nanowire stem-branch heterostructure, Sensors and Actuators B, 181 (2013) 787-794.

[23] D. Zappa, E. Comini et al. Preparation of copper oxide nanowire-based conductometric chemical sensors, Sensors and Actuators B, 182 (2013), 7-15.

[24] E. Comini, C. Baratto et al. Quasi-one dimensional metal oxide semiconductors: Preparation, characterization and application as chemical Sensors, Progress in

Materials Science, 54 (2009) 1–67.

[25] A. Vomiero, A. Ponzoni, E. Comini, Direct integration of metal oxide nanowires into an effective gas sensing device, Nanotechnology 21 (2010) 145502.

[26] A.Kolmakov, D.O. Klenov, Y. Lilach et al., Enhanced gas sensing by individual SnO2 nanowires and nanobelts functionalized with Pd catalyst particles, Nanoletters, 4 (2005), 667-673.

[27] V.V.Sysoev, B.D. Button et al., Toward the nanoscopic “Electronic nose”: hydrogen vs carbon monoxide discrimination with an array of individual metal oxide nano- and mesowire sensors, Nanoletters, 8 (2006), 1584-1588.

[28] F.Shao, M.W.G. Hoffmann et al. Heterostructured p-CuO (nanoparticle)/n-SnO2 devices for selective H2S detection, Sensors and Actuators B, 181 (2013) 130-135.

[29] N.D.Chinh, N.V.Toan et al. Comparative NO2 gas-sensing performance of the self-heated individual, multiple and networked SnO2 nanowire sensors fabricated by a simple process, Sensors and Actuators B, 201 (2014), 7-12.

[30] A. Kolmakov, M. Moskovits, et al. Chemical sensing and catalysis by onedimensional metal-oxide nanostructures, Annual Review of Materials Research 34 (2004) 151–180.

[31] V.V. Sysoev, E. Strelcov et al. Single-Nanobelt Electronic Nose: Engineering and Tests of the Simplest Analytical Element, ACS NANO, 8 (2010) 4487–4494.

[32] V.V. Sysoev, E. Strelcov The electrical characterization of a multi-electrode odor detection sensor array based on the single SnO2 nanowire, Thin Solid Films, 520 (2011) 898–903.

[33] F. Hernandez-Ramırez, A. Tarancon et al., Fabrication and electrical characterization of circuits based on individual tin oxide nanowires, Nanotechnology 17 (2006) 5577–5583.

[34] F. Hernandez-Ramırez, A. Tarancon et al. High response and stability in CO and humiditymeasures using a single SnO2 nanowire, Sensors and Actuators B 121 (2007) 3–17.

[35] D. Shaposhnik, R. Pavelko et al. Hydrogen sensors on the basis of SnO2–TiO2

systems. Sensors and Actuators B: Chemical. Volume 174, November 2012, Pages 527–534.

6. Ammonia detection using MOx sensor – MOx converter system

6.1. Ammonia properties and applications

Ammonia (hydrogen nitride) is a colorless gas with a characteristic pungent smell. It is approximately twice lighter than air.

Ammonia molecule has a form of trigonal pyramid with a nitrogen atom at the vertex. Three uncoupled p-electrons of nitrogen atom participate in the formation of polar bonds with 1s-electrons of hydrogen atom; fourth pair of outer electrons is unshared. It can form a dative bond with 1s-electrons of hydrogen ion, forming ammonium ion NH_4^+. Thanks to the orientation of two electrons cloud, ammonia molecule has a high polarity, what leads to a good solubility in water.

Ammonia, either directly or indirectly, is a building block for the synthesis of many pharmaceuticals and is used in many commercial cleaning products. Although in wide use, ammonia is both caustic and hazardous. The global industrial production of ammonia for 2012 was anticipated to be 198 million tones [1], a 35% increase over the estimated 2006 global output of 146.5 million tones [2].

Anhydrous ammonia is classified as toxic and dangerous for the environment. The gas is flammable (autoignition temperature is 651 °C) and can form explosive mixtures with air (16–25%). OSHA 15-minute exposure limit for gaseous ammonia is 35 ppm, and an 8-hour exposure limit is 25 ppm; at the same time normally the odor is detectable at concentrations of about 50 ppm.

The detection of ammonia in atmosphere is an important task of ecological monitoring.

6.2. Detection of ammonia with different types of gas sensors

Ammonia is being detected by a number of different types of sensors. Colorimetric sensor [3] was used for qualitative discrimination of different amines and qualitative determination of trimethylamine down to 125 ppb at nitrogen. Surface acoustic wave sensors [4] showed positive differential frequency shift (Δf) for humidified ammonia gas and negative Δf for the rest of tested gases, including dry NH_3 and water vapors. Solid electrolyte type sensor based on trivalent aluminium ion solids [5] showed good water durability and thermal stability, as well as reproducible sensor response to NH_3. Fluorescent polymeric microparticle sensors [6] was reported, the detection limit achieved for ammonia vapor was 0.73 ppm, the response being linearly dependent on concentration over the range of 1.0–250 ppm of gaseous ammonia (evaporation of liquor ammonia was used, gas concentrations were calculated). $NiCl_2$ nanocrystals diffractive optic sensor for remout-point detection of ammonia (down to 2 ppm) was presented [7]; evaporation of liquor ammonia was used as well. Piezoelectric resonance sensors coated with humic acids [8] were reported, the detection limit was ~10 mg/m^3. An optoelectronic gas sensor based on interferometric nanostructures was presented [9]; the sensor worked reliably at 70^{o}C; the effect of RH change from 4.5% to 65% to sensor response was found to be rather small at NH_3 concentration range from 8 to 125 ppm.

A zeolite based sensor was developed for selective ammonia detection in exhaust gas for automotive applications [10]. In ammonia concentration range between 0 and 1000 ppm the sensor showed no cross-sensitivity to carbon monoxide. A sensor using mixed potential principle is commercially available from Delphy [11]. It helps diesel manufacturers meet more stringent NOx emissions regulations.

Flexible, all-organic ammonia sensors based on dodecylbenzene sulfonic acid-doped polyaniline films were applied for ammonia detection in humid atmosphere at close to room temperature [12]. The sensitivity linearly related to concentration in the range between 5 ppm and 70 ppm. The response time was about 10 minutes. Relative humidity, and to a lesser extent temperature, strictly affected the sensors' response. The authors presume that integration of PANI:DBSA sensors with capacitive humidity sensors and a heater on the same substrate can help to consider the influence of humidity on the sensor's signal and minimize recovery time of the sensor.

Wafer-scale fabrication of single polypyrrole nanoribbon-based ammonia sensor was reported [13]. Fast response and recovery was observed to ammonia concentrations from 0,5 to 5 ppm at dry air and at room temperature. However, at higher concentrations there was no return of the sensor signal to the baseline. The sensing performance of the PPy nanoribbon based ammonia gas sensor is strongly influenced by the Debye length or charge interaction zone, which is affected by charges, temperature, dielectric constant, and carrier concentration of materials.

Despite great advances in the creation of low power consuming, highly sensitive and inexpensive semiconductor sensors, most of these sensors show some common shortcomings, among which the lack of selectivity, as well as sensor drift, could be considered as the most pronounced.

Modern requirements to sensors developers include the close-future creation of portable, simple, cheap, low power consuming (with the purpose to become self-standing and wireless) automatic devices that are able to be once mounted and work for a long time without operator participation [14-16].

Figaro Engineering provides two sensors for ammonia detection: TGS 826 with 833 mW power consumption and typical detection range 30-300 ppm for leak detection from refrigerators, and TGS2444 with 56 mW power consumption, typical detection range 10-100 ppm for ventilation control in agricultural and poultry industries. TGS 2444 sensor requires application of a 250 msec heating cycle which is

used in connection with a circuit voltage cycle of 250 msec (Figure 6.1). Each V_H cycle is comprised by 4.8V being applied to the heater for the first 14 ms, followed by 0V pulse for the remaining 236 ms. The V_c cycle (applied across the sensing element) consists of 0V applied for 2 msec, followed by 5.0V for 5ms and 0V for 243msec. For achieving optimal sensing characteristics, the sensor's signal should be measured after the midpoint of the 5ms V_c pulse of 5.0V. Application of a V_c pulse condition is required to prevent possible migration of heater materials into the sensing element material. A 5ms V_c pulse results in significantly less driving force for migration than a constant V_c condition, rendering the possibility of migration negligibly small. No data describing the effects of ambient humidity changes is presented for TGS 2444 product information.

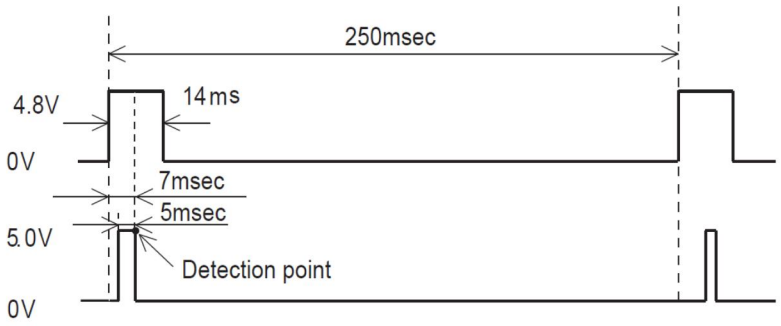

Figure 6.1. Heating cycles of TGS2444 sensor (taken from figaro.co.jp). Heating voltage (top) and voltage applied to sensing element (bottom)

A highly selective room temperature ammonia sensor using spray deposited zinc oxide thin film was reported [17]. In the gas sensing setup, conical flask was interconnected with gas sensing chamber. A calculated volume of liquor ammonia was injected into the conical flask with the help of chromatographic syringe. Ammonia vapour went to the testing chamber by means of free convection until the achievement of steady state. Highest room temperature response of 233 was achieved at 25 ppm of NH_3 with a response and recovery times of 20 and 25 s respectively.

Ammonia sensor sensitivity enhancement using graphene/polyaniline nanocomposite was reported [18]. The experimental result reveals that the

graphene/PANI sensor exhibits much higher sensitivity (ca. 5 times) than that of PANI. The detection limit of the nanocomposite sensor was 1 ppm of ammonia in dry air.

Tin oxide/graphene (GN) composite fabricated via a hydrothermal method for gas sensors working at room temperature was described [19]. The sensors exhibited gas sensing properties to NH_3 at room temperature: response magnitude was 15.9% for 50 ppm NH_3, response and recovery time was < 1 min; sensor demonstrated good reversibility and repeatability. The ambient gas used in the experiments was nitrogen.

Metal oxide-based nanosensor that is highly specific to ammonia gas in breath-simulating environments at low part-per-billion concentrations was presented [20]. The effect of humidity was evaluated. A commercially available CO_2 filter was used. Ammonia was detected at concentrations down to 50 ppb in air. When the sensor was exposed to various concentrations of NH_3 and CO_2 (using the filter to scavenge CO_2), the presence of CO_2 did not affect NH_3 sensing, for concentrations ranging between 0.5 and 10 ppm. Preliminary data also showed that up to 25% humidity in the gas stream does not have any effect on the performance of the sensor.

An ammonia monitor with excellent sensing characteristics, based on photoacoustic (PA) spectroscopy, was presented [21]. This trace-ammonia analyzer has been developed for measuring ambient ammonia concentration in the lower ppb concentration range. An optimized measurement method (dual wavelength) efficiently suppresses cross-sensitivity to other atmospheric components, most importantly to water vapor, while improving the sensitivity of the system. The developed PA system was tested with reference to a continuous-flow denuder system (AMANDA) under both laboratory and simulated field conditions, and it featured highly reliable, fully automatic operation with a detection limit of about 50 ppb of ammonia. However, the usual prices of photoacustic devices normally don’t allow to put them in the same line with inexpensive sensors like, for example, MOx chemiresistors.

6.3. Engineering approaches for the improvement of conductometric gas sensor selectivity and stability

The main disadvantage of metal oxide sensors is their low selectivity; therefore it is difficult to distinguish ammonia from other reducing gases (carbon monoxide, hydrogen, hydrogen sulphide). Another disadvantage of MOX sensors is signal drift, which may be caused by both sorption (-desorption) process and the changes of MOX semiconductor surface structure during the measurement. A possible way to solve the problem of signal drift is to expose alternatively the sensor to the gas mixture to be measured and to the reference gas, but this procedure requires relatively complex equipment, which cannot be used in portable and unmanned devices.

Another problem of ammonia sensing with semiconductor sensors is that the response to ammonia ordinarily is lower than responses to other reducing gases, what makes the problem of selectivity even more pronounced.

Selectivity can be defined as the ability of a sensor to respond to a certain gas in the presence of other gases [22].

Between the methods of semiconductor sensor selectivity increase are: 1) control of the temperature of the sensing layer; 2) change of the layer thickness, morphology, sensor architecture and the use of gas separating coatings; 3) the use of additional passive and catalytically active filters; 4) separation of analytes, i.e., gas chromatography; 5) bias voltage and gas concentration modulation; 6) monitoring sensing layer temperature in order to find out endothermic and exothermic reactions; 7) use of sensor array (e-nose); 8) temperature cycling (dynamic) mode of operation [22].

The first approach (control of the sensor operating temperature) suppose that gases possessing specific combination of adsorption/desorption parameters and reaction rates might have different temperature profiles of sensor response and therefore these gases could be selectively recognized [23]. This approach cannot

completely resolve the problem of low selectivity of metal oxide-based conducrometric gas sensors, because temperature profiles of sensor signal are too broad and there are too many gases, which have similar $S = f(T_{oper})$ dependences.

The use of gas separating coatings, passive filters and the control of the sensing layer thickness is useful in the case of determination of gases with different properties, e.g., with notably different molecule size. This approach showed high potential for the selective detection of hydrogen (small molecules) in the presence of CO (bigger molecules) [24-26]. The same principle underlies the use of passive filters [27-29]. The filter can selectively remove interferences or transform them into an inactive phase. In particular, various devices developed for CO detection successfully utilize charcoal as a filter to avoid the interfering effect of hydrocarbons and alcohols [30-32]. In the last case, an additional pump, delivering analyzing ambient to the gas sensor through the filter, must be used.

Another approach in this line is the use of catalytically active filters, like, for example, Pt [33] or Pt-SnO_2 [34] thick films over Pt-SnO_2 sensing layer. The use of such active films in direct contact with the gas-sensing semiconductor makes the effect rather complex in terms of both electroconductivity (shunting of the sensing layer by the catalytic layer) and chemistry (the influence of reaction products on the sensor signal). In order to separate the gas-sensing oxide layer and the metal filter, an intermediate porous insulating layer may be applied [35, 36]. Such solution makes the construction of the sensor rather more complex.

It's possible to improve the MOX sensor selectivity via monitoring the sensor operating temperature. When the target gas interacts with the MOX, the surface reactions, endothermic or exothermic, yield a measurable change in the surface temperature, ΔT [37]. The potential of using changes in the sensor temperature, resistance, capacitance, and inductance of the same gas-sensing material to improve the gas selectivity of the MOXs was explored [38]. The main limitation of this method is that real gas mixtures are not binary and may contain significant concentrations of interference gas species. So, sensor response will not be unique

for each concentration of target gas, but will depend on the current composition of the gas ambient.

The collection of sensors into arrays is one of the most powerful approaches to yield an analyte-selective signal [22]. An electronic nose can be performed as simple, portable, inexpensive device. The disadvantages of this approach are the inability to provide absolute calibration and inability to obtain quantitative data for aroma differences [39]. Additionally, in comparison with single sensor devices, sensor array consumes more power. A common problem of both electronic nose and single sensor devices is sensor drift (and, in addition, a system drift of a sensor array). Standardization of metal oxide sensor array using artificial neural networks was reported and a model for e-nose signal shift standardization was proposed [40].

A perspective technique for a sensor system performance improvement is coupling a sensor or a sensor array with a (micromachined) chromatographic column. Chromatographic technique allows to separate components of a gas mixture by their retention time and thus to obtain a selective gas sensing system consisting of a (non-selective) detector and a chromatographic column. The performance of such devices can be increased by the use of a micromachined chromatorgraphic column due to decreased size and power consumption, and the reduced time for analysis [41]. Micromachined GC columns have a high potential as an analytical platform for the selective detection of pollutants [42]. However, such analytical systems usually do not intend for in-situ and uninterrupted measurements.

In order to improve sensor selectivity and stability, the electrode functionalities: electrical conductivity, selective catalytic activity, and electrochemical activity, can be separated [43]. The sensor used in the mentioned work was based on described in literature mixed potential effect [44-46]. Electrodes were located on the top of solid electrolyte (yttria stabilized zirconia). Sensing electrode was covered with catalyst, provided ammonia selectivity. Low cross-sensitivity to interfering gases demonstrated with the sensor device shows that it is

possible to optimize independently the electrode and the catalyst layers in order to achieve better selectivity and stability.

An approach for sensor selectivity increase used in the present work is the application of a microreactor which selectively converts a target gas into the form more suitable for the detection with a gas sensor. The difference between μ-GC and preconcentrators, from one hand, and reactors/converters, from the other, is that preconcentrators and chromatographic columns doesn't affect the nature of the analyzed compound, while in converters chemical reactions (like derivatization) take place with a product that is more convenient for the detector that an initial analyte compound.

In one of early works on microreactors application for gas detection [47], the gas-sensing devices were embedded into micro-fluidic systems containing micro-valves and micro-pumps in addition to the gas-sensing devices. In the next work of the authors [48], an in-depth analysis of the gas-sensing properties of thin-film metal–oxide sensors embedded within tiny silicon micro-chambers was presented. thin-film metal–oxide gas sensors on micro-machined heater substrates were embedded into tiny silicon micro-chambers to form micro-reactor devices. Micro-reactor device was used to analyze samples of polluted air for their O_3 and NO_2 contents. In no-flow mode, clean-air no-flow reference value was not reached after sufficiently long enclosure times. This effect was attributed to the fact that, upon interaction with heated tin oxide surfaces, NO_2 cannot be converted into more or less undetectable follow-on products. According to the thermal desorption experiments of the Yamazoe group [59], adsorbed NO_2 is always re-desorbed in the form of NO molecules. These latter molecules, in turn, interact with the relatively cool air inside the micro-chamber forming NO_2, which again can become detected at the heated sensor surface. This different kind of surface interaction, therefore, was used to distinguish NO_2 from O_3.

In later works of the authors [49] it was shown the possibility of the fabrication of a simple micromachined reactor gas monitoring system for selective sensing of air pollutants, namely NO_2, NO, CO, CH_4 and O_3, using the approach described above and different types (thick- and thin-film) of MOx sensors.

6.4. Conversion of ammonia to NOx

In our work it was used a reactor for conversion of NH_3 to NO_2. This process is known and is used in a number of applications, including converters coupled with chemiluminescent sensors in a number of commercially available devices.

The conversion of gaseous ammonia to nitrogen oxide is also used, for example, in production of nitric acid. In this process ammonia is converted to nitric acid in two steps. It is oxidized by heating ammonia with oxygen in the presence of a catalyst such as platinum with 10% rhodium to form nitric oxide and water [50].

$$4\ NH_3\ (g) + 5\ O_2\ (g) \rightarrow 4\ NO\ (g) + 6\ H_2O\ (g)\ (\Delta H = -905.2\ kJ)$$

Second stage is carried out in the presence of water in an absorption apparatus. Nitric oxide is oxidized again to yield nitrogen dioxide (which later is converted to nitric acid):

$$2\ NO\ (g) + O_2\ (g) \rightarrow 2\ NO_2\ (g)\ (\Delta H = -114\ kJ/mol)$$

In the commercial process, the catalyst used is platinum-rhodium metal gauze that is heated to about 1173 K [51] or platinum wires heated to 1000-1200 K [52].

It was shown that lanthanide oxide systems are as active at catalytic oxidation as platinum-rhodium catalysts [52].

RuO_2 has proved to be an alternative catalyst that can replace platinum in NH_3 oxidation in Ostwald process at lower temperature [53, 54]. It was attempted to coat the porous TiO_2 nanofibers with sol-gel-derived RuO_2 [55]. Selective catalytic oxidation of ammonia to nitrogen over mesoporous CuO/RuO_2 synthesized by co-nanocasting-replication method was reported [56].

Converters of NH_3 to NO_2 are often used in commercial gas analyzers with chemiluminescence detectors. Among nitrogen containing compounds chemiluminescence sensors can detect directly only nitrogen monoxide. For NO detection, this compound interacts with ozone in a special chamber. During this reaction occurs luminescence which is detected by the sensor. In order to detect other nitrogen containing compounds, it is necessary to transform them to NO: to reduce NO_2, HNO_3 and other compounds with nitrogen in higher oxidation numbers, and to oxidize ammonia. For this purpose there are used converters, where different compounds are transformed to NO at different conversion conditions.

For example, in the converter used in commercially available from Thermo Scientific TEI 17C Ammonia Analyzer, the catalytic oxidation takes place in a steel chamber at 825°C. From the information on both the conversion conditions and sensor signal (which is proportional to NO concentration) it is possible to estimate the amount of every nitrogen-containing compound in the ambient. The same principle of detection is used in the devices made by The HORIBA Group. Minimal detectable sensitivity of HORIBA monitors is 10 ppb, and lower detectable limit 1 ppb. The whole device is a bulk instrument which consumes 400-500 W power and weighs 35-45 kilograms.

Work has been undertaken to improve the converter performance. The comparison of nanosized catalysts for ammonia oxidation was studied [57]. The nanosized $LaCoO_3$ was chosen as the catalyst for preparing the converter coupled with chemiluminescence detector. The detection limit of the obtained device was 0.014 ppm. The method offers advantages of long lifetime of the converter, fast response and high selectivity to NH_3.

6.3. Results and discussion

6.3.1. Ammonia detection with conventional SnO_2 sensors

Figure 6.2 shows SnO_2 sensors response temperature dependence at ammonia concentration 110 ppm. Curves have two extremes and look similar to sorption isotherms. Some response increase below 175 ^oC can be explained by the influence of phisisorption. Ammonia, being a polar compound, can change carrier concentration in absorbent semiconductor during phisisorption. Response increase at temperature above 200 ^oC can be explained by chemisorption. In this case, a chemical interaction with participation of ionized surface oxygen takes place:

$$2NH_3 + 3O^- \rightarrow N_2 + 3H_2O + 3\bar{e}$$

Response maximum is observed at 300 ^oC and can be related with the maximum of chemisorption.

Addition of catalytic platinum and palladium dopants leads to increase of the response in several times. Addition of silver leads to insignificant increase of the signal.

Sensor response on ammonia concentration is obtained at 300 ^oC. It appears as power dependence (Figure 6.3).

The results obtained show that doping of tin dioxide with palladium increases sensor response. For example, SnO_2 sensor signal to 3.5 ppm of ammonia was 0.41, while SnO_2-Pd sensor demonstrated signal 2,75 at the same concentration of ammonia.

Temperature dependences of blank and metal doped sensors at 110 ppm of ammonia in air were obtained. The dependences demonstrated signal maximum for noble metal doped sensors at 300 ^oC.

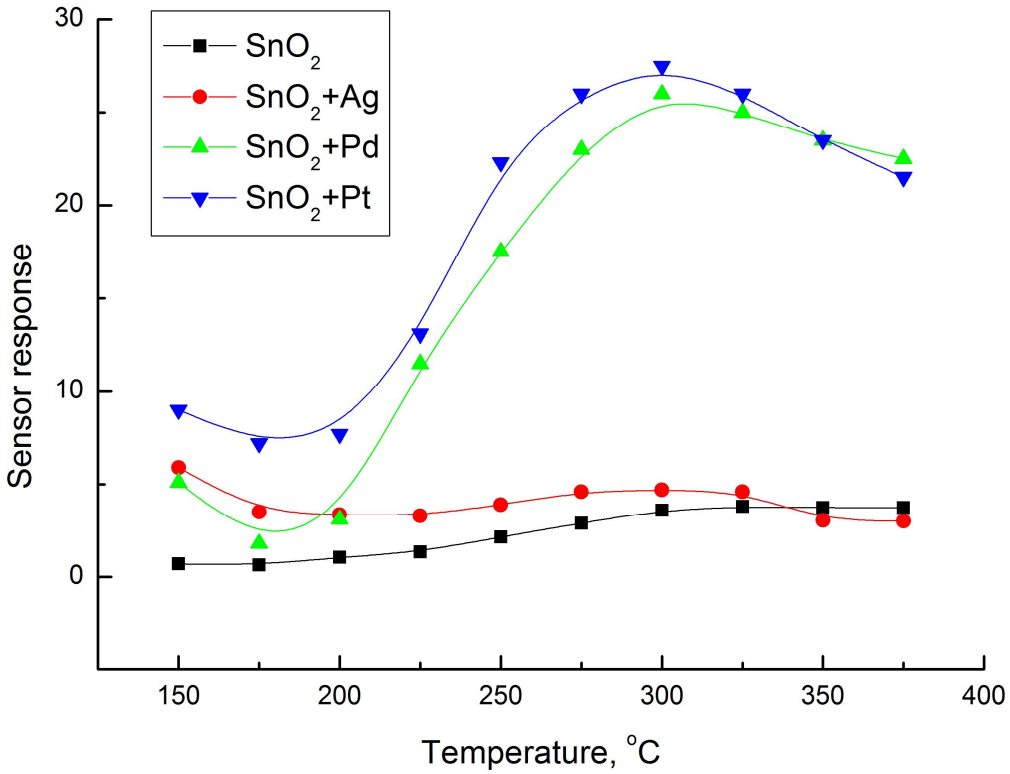

Figure 6.2. Temperature dependence of sensors' response to 110 ppm of ammonia

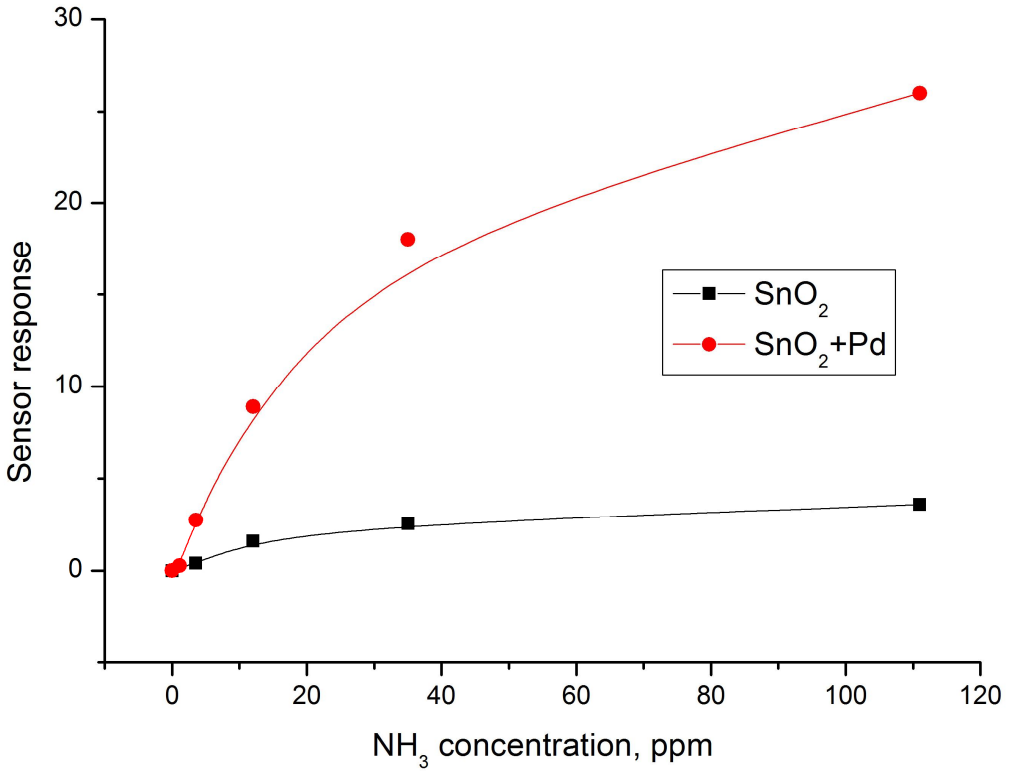

Figure 6.3. Signals of SnO_2 and SnO_2-Pd sensors to ammonia

6.3.2. Ammonia detection with SnO_2 sensor and converter

We tried to perform selective ammonia detection using microreactor including gas chamber and converter. Gas chamber with internal volume 0,67 cm^3 consists of TO-8 package and removable cover. The chamber is connected to atmosphere by a 2 mm aperture.

Converter of ammonia to nitrogen oxide consisted of alumina micro-substrate substrate with deposited platinum heater and catalyst layer (see paragraph 2.3.2.3). The catalyst consisted of tin dioxide doped with 3wt.% of palladium and 1wt.% of platinum. The heating of the converter from room temperature to working temperature (350°C) took less than 1 second. The catalytic oxidation of ammonia took place during the heating. A sensor with high sensitivity to nitrogen dioxide, based on tin oxide doped with 2wt.% of gold 2wt.% of nickel oxide was used. The sensor was operated at constant temperature.

Heating periods of the catalytic converter are shown in Figure 6.4 with arrows.

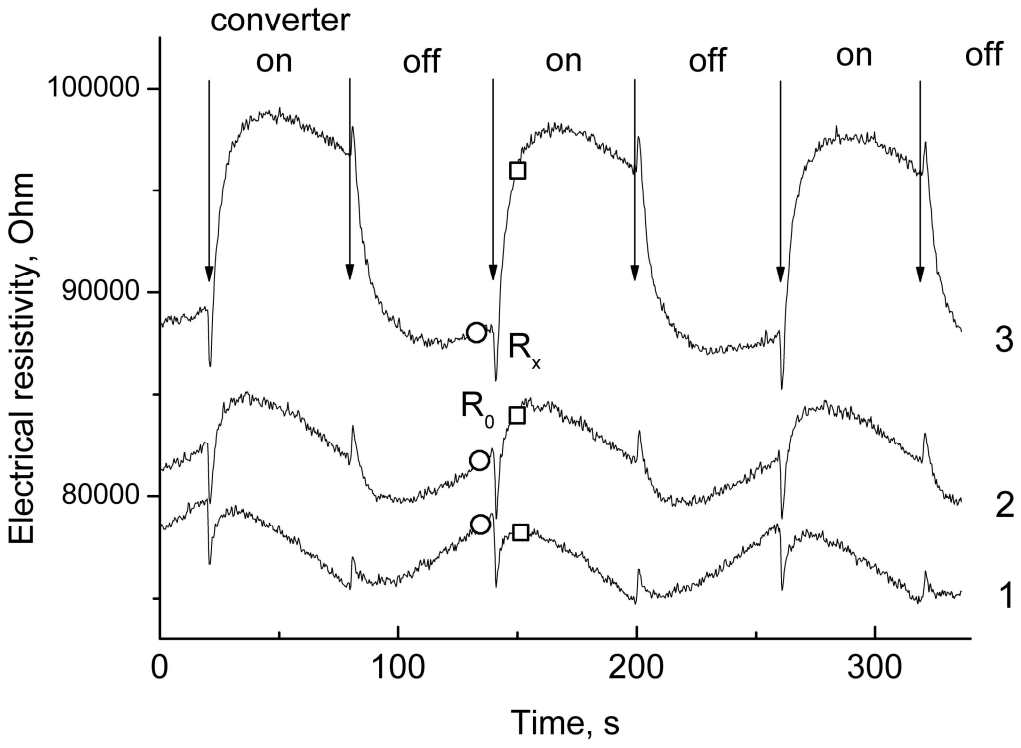

Fig. 6.4. Electrical resistivity of the sensor as a function of time in pure air (curve 1), in 4.5 ppm of ammonia in air (2), and in 9 ppm of ammonia (3)

The appearance of nitrogen dioxide in the gas chamber, as well as a decrease in ammonia concentration, resulted in an increase in sensor resistance (lines 2 and 3 in figure 6.4). After the heating is turned off, the generation of nitrogen dioxide is stopped, this leads to an increase in ammonia concentration in the chamber and to a decrease in sensor resistance. Line 1 corresponds to the sensor resistance in air, line 2 and 3 show the sensor resistance at ammonia/air mixtures with concentrations 4.5 and 9 ppm, respectively. The temperature of converter changed from 25 to 350 ^{o}C, the working temperature of sensor was constant and equal to 250 ^{o}C.

Usually, the analytical signal of the sensor is the normalized difference between the sensor resistivity in investigated atmosphere and in standard one. The use of microreactor gives an opportunity of a considerable increase in the stability of measurements, because it is possible to apply as a analytical signal *G* the normalized difference between the sensor signals, when the converter is working (R_x) and when it is turned off (R_0):

$$G = \frac{R_x - R_0}{R_0}$$

Corresponding values of R_0 and R_x of electrical resistivity are marked by circles and squares in Figure 6.4.

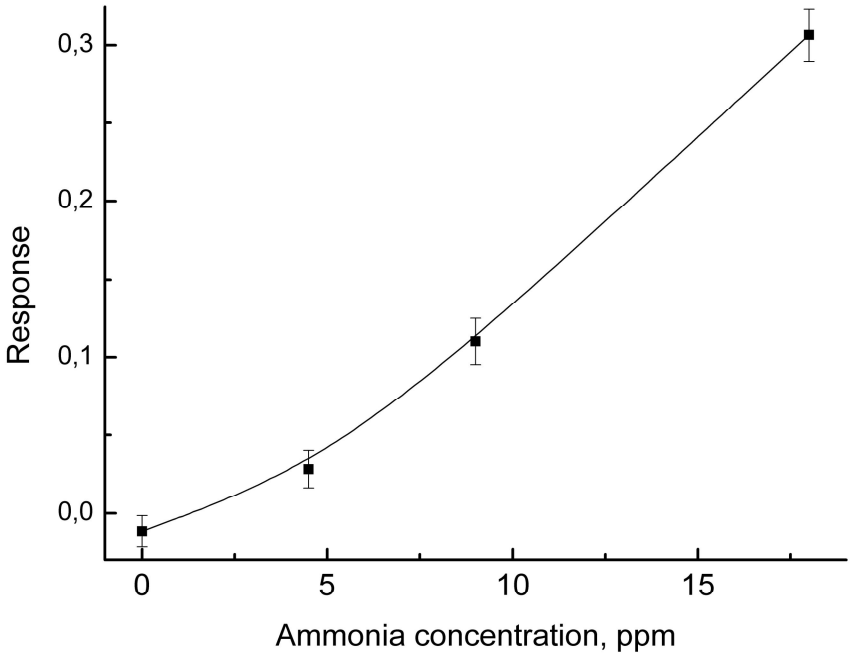

Fig. 6.5. Calibration curve of the device included sensor and microreactor

The analytical signal as a function of ammonia concentration is shown in Figure 6.5. The use of microreactor allows the determination of low ammonia concentrations in air. High stability of sensor response is related with the elimination of the influence of sensor drift, because the sensor signal is a difference between two values of resistance measured with switched on and switched off converter, respectively.

References Chapter 6

[1] Ceresana. Market Study: Ammonia.

[2] Ullmann's Encyclopedia of Industrial Chemistry. Weinheim: Wiley-VCH, 2002

[3] Zh. Tang, J. Yang, J. Yu, Bo Cui. A Colorimetric Sensor for Qualitative Discrimination and Quantitative Detection of Volatile Amines. Sensors. 2010, 10, 6463-6476.

[4] V. Bhasker Raja, A.T. Nimalb, Yashoda Parmarb, M.U. Sharmab, K. Sreenivasa, Vinay Gupta. Cross-sensitivity and selectivity studies on ZnO surface acoustic wave ammonia sensor. Sensors and Actuators B 147 (2010) 517–524.

[5] Tsukasa Nagaia, Shinji Tamuraa, Nobuhito Imanakaa. Solid electrolyte type ammonia gas sensor based on trivalent aluminum ion conducting solids. Sensors and Actuators B 147 (2010) 735–740.

[6] Y. Takagai, Y. Nojiri, T. Takase, W. L. Hinze, M. Butsugan. ‘‘Turn-on’’ fluorescent polymeric microparticle sensors for the determination of ammonia and amines in the vapor state. Analyst, 2010, 135, 1417–1425.

[7] M. Vasileiadis, L. Athanasekos, A. Meristoudi, D. Alexandropoulos, G. Mousdis, V. Karoutsos, A. Botsialas, N. A. Vainos. Diffractive optic sensor for remote-point detection of ammonia. Optics Letters / Vol. 35, No. 9 / May 1, 2010.

[8] A. A. Zvyagin, D. V. Nenakhov, S. N. Korchagina, A. V. Shaposhnik, V. V. Kotov, V. A. Yukish. Determination of Ammonia in the Air Using Piezoelectric Resonance Sensors Coated with Humic Acids. Russian Journal of Analytical Chemistry, 2010, Vol. 65, No. 4, pp. 414–417.

[9] E. Maciak, T. Pustelny. An optical ammonia (NH3) gas sensing by means of Pd/CuPc interferometricnanostructures based on white light interferometry. Sensors and Actuators B 189 (2013) 230– 239.

[10] R. Moos, R. Müller, C. Plog, A. Knezevic, H. Leye, E. Irion, T. Braun, K.-J. Marquardt, K. Binder. Selective ammonia exhaust gas sensor for automotive applications. Sensors and Actuators B. Volume 83 (2002) 181–189.

[11] Wang D.Y., Symons W.T., Farhat R.J., Valdes C.A., Briggs E.M., Polikarpus K.K., Kupe J. Ammonia Gas Sensors. Jul 11, 2006. U. S. Patent 7,074,319 B2.

[12] G. Rizzo, A. Arena, N. Donato, M. Latino, G. Saitta, A. Bonavita, G. Neri. Flexible, all-organic ammonia sensor based on dodecylbenzene sulfonic acid-doped polyaniline films. Thin Solid Films 518 (2010) 7133–7137.

[13] N. Chartuprayoon, C. M. Hangarter, Y. Rheem, H. Jung, N. V. Myung. Wafer-Scale Fabrication of Single Polypyrrole Nanoribbon-Based Ammonia Sensor. J. Phys. Chem. C 2010, 114, 11103–11108.

[14] Javier Bonal. Strategy and activities of the Microsystems and Nanosystems Unit. Common Strategic Framework for EU research and innovation funding. Eurosensors XXV. Athens, Greece, 2011.

[15] D. Briand, F. Molina-Lopez, A. V. Quintero, C. Ataman, J. Courbat, N. F. de Rooij. Why Going Towards Plastic and Flexible Sensors? Eurosensors XXV. Procedia Engineering, Volume 25, 2011, Pages 8–15.

[16] G. Müller, S. Beer, S. Paul, A. Helwig. Novel Chemical Sensor Applications in Commercial Aircraft. Eurosensors XXV. Procedia Engineering. Volume 25, 2011, Pages 16–22.

[17] G. K. Mani, J. Bosco, B. Rayappan. A highly selective room temperature ammonia sensor using spray deposited zinc oxide thin film. Sensors and Actuators B 183 (2013) 459– 466.

[18] Z. Wua, X. Chena, S. Zhub, Z. Zhoub, Y. Yaoa, W. Quana, B. Liu. Enhanced sensitivity of ammonia sensor using graphene/ polyaniline nanocomposite. Sensors and Actuators B 178 (2013) 485– 493.

[19] Q. Lin, Y. Li, M. Yang. Tin oxide/graphene composite fabricated via a hydrothermal method for gas sensors working at room temperature. Sensors and Actuators B 173 (2012) 139– 147.

[20] P. Gouma, K. Kalyanasundaram, X. Yun, M. Stanacevic, L.Wang. Nanosensor and Breath Analyzer for Ammonia Detection in Exhaled Human Breath. IEEE Sensors Journal, Vol. 10, No. 1, January 2010.

[21] H. Huszara, A. Poganya, Z. Bozoki, A. Mohacsi, L. Horvathd, G. Szabo. Ammonia monitoring at ppb level using photoacoustic spectroscopy for environmental application. Sensors and Actuators B 134 (2008) 1027–1033.

[22] G. Korotcenkov, B.K. Cho. Engineering approaches for the improvement of conductometric gas sensor parameters Part 1. Improvement of sensor sensitivity and selectivity (short survey). Sensors and Actuators B 188 (2013) 709– 728.

[23] S.R. Morrison, Selectivity in semiconductor gas sensors, Sens. Actuators 12(1987) 425–440.

[24] A. Shaposhnik, A. Vasiliev, N. Demochko, S. Ryabtsev. SnO_2/Pd sensors with polymer coatings for the selective measurement of gas concentrations. Proc. of “Eurosensors-XIX”, Barcelona, 2005. – V. 2. – P. 91-93.

[25] A. Katsuki, K. Fukui, H_2 selective gas sensor based on SnO_2, Sens. Actuators B 52 (1998) 30–37.

[26] Z. Zhan, D. Jiang, J. Xu, Investigation of a new In_2O_3-based selective H_2 gas sensor with low power consumption, Mater. Chem. Phys. 90 (2005)250–254.

[27] C.D. Feng, Y. Shimizu, M. Egashira, Effect of gas diffusion process on sensing properties of SnO_2 thin film sensors in a SiO_2/SnO_2 layer-built structure fabricated by sol-gel process, J. Electrochem. Soc. 141 (1994) 220–225.

[28] M. Sauvan, C. Pijolat, Selectivity improvement of SnO_2 films by superficial metallic films, Sens. Actuators B 58 (1999) 295–301.

[29] C. Pijolat, J.P. Viricelle, G. Tournier, P. Montmeat, Application of membranes and filtering films for gas sensors improvements, Thin Solid Films 490 (2005) 7–16.

[30] P. McGeehin, Self-diagnostic gas sensors which differentiate carbon monoxide from interference gases for residential applications, Sensor Rev. 16 (1996)37–39.

[31] M. Schweizer-Berberich, S. Strathmann, W. Gopel, R. Sharma, A. Peyre-Lavigne, Filters for tin dioxide CO gas sensors to pass the UL2034 standard, Sens. Actuators B 66 (2000) 34–36.

[32] S. Kitsukawa, H. Nakagawa, K. Fukuda, S. Asakura, S. Takahashi, T. Shigemori. The interference elimination for gas sensor by catalyst filters, Sens. ActuatorsB 65 (2000) 120–121.

[33] F. Menil, C. Lucat, A. Debich, The thick-film route to selective gas sensors, Sens. Actuators B 25 (1994) 415–420.

[34] G.G. Mandayo, E. Castano, F.J. Gracia, A. Cirera, A. Cornet, J.R. Morante, Built-inactive filter for an improved response to carbon monoxide combining thin-and thick-film technologies, Sens. Actuators B 87 (2002) 88–94.

[35] G. Sberveglieri, Classical and novel techniques for the preparation of SnO_2 thin-film gas sensors, Sens. Actuators B 6 (1992) 239–247.

[36] M. Frietsch, F. Zudock, J. Goschnick, M. Bruns, CuO catalytic membrane as selectivity trimmer for metal oxide gas sensors, Sens. Actuators B 65 (2000) 379–381.

[37] A. Heilig, N. Barsan, U. Weimar, W. Gopel, Selectivity enhancement of SnO_2 gas sensors: Simultaneous monitoring of resistances and temperatures, Sens.Actuators B 58 (1999) 302–309.

[38] T. Takada, A new method for gas identification using a single semiconductor sensor, Sens. Actuators B 52 (1998) 45–52.

[39] W.J. Harper, The strengths and weaknesses of the electronic nose, Adv. Exp.Med. Biol. 488 (2001) 59–71.

[40] L. Zhang, F. Tiana, X. Peng, L. Dang, G. Li, Sh. Liu, Ch. Kadri. Standardization of metal oxide sensor array using artificial neural networks through experimental design. Sensors and Actuators B 177 (2013) 947– 955.

[41] A. Bhushan, D. Yemane, D. Trudell, E.B. Overton, J. Goettert, Fabrication ofmicro-gas chromatograph columns for fast chromatography, Microsyst. Tech-nol. 13 (2007) 361–368.

[42] J.-B. Sanchez, A. Schmitt, F. Berger, C. Mavon, Silicon-micromachined gas chromatographic columns for the development of portable detection device, J.Sensors (2010) 409687.

[43] D. Schönauer, K. Wiesner, M. Fleischer, Ralf Moos. Selective mixed potential ammonia exhaust gas sensor. Sensors and Actuators B 140 (2009) 585–590.

[44] N. Miura, G. Lu, N. Yamazoe, High-temperature potentiometric/amperometric NOx sensors combining zirconia and mixed-metal electrode, Sens. Actuators B: Chem. 52 (1998) 169–178.

[45] U. Guth, Gas sensors, in: A.J. Bard, G. Inzelt, F. Scholz (Eds.), Electrochemical Dictionary, Springer, Berlin, Heidelberg, 2008, pp. 294–299.

[46] R. Moos, K. Sahner, G. Hagen, A. Dubbe, Zeolites for sensors for reducing gases, Rare Metal Mater. Eng. 35 (Suppl. 3) (2006) 447–451.

[47] A. Meckes, J Behrens, O. Kayser,W. Benecke, T. Becker, and G. Müller, "Microfluidic system for the integration and cyclic operation of gas sensors," Sens. Actuators A, vol. 76, pp. 482–487, 1999.

[48] T. Becker, S. Mühlberger, C. Bosch-v.Braunmühl, G. Müller, A. Meckes, and W. Benecke. Gas Mixture Analysis Using Silicon Micro-Reactor Systems. Journal of Microelectromechanical Systems, Vol. 9, No. 4, December 2000.

[49] Th. Becker, S. Ahlers, Chr. Bosch-v.Braunmühl, G. Müller, O. Kiesewetter, Comparison of tin oxide-based thick- and thin-film sensor elements deposited on micromachined and ceramic substrates, in: Proceedings of the 8th International Meeting on Chemical Sensors, Basel (Switzerland), 2000.

[50] Alan V. Jones; M. Clemmet; A. Higton; E. Golding (1999). Alan V. Jones. ed. Access to chemistry. Royal Society of Chemistry. p. 250. ISBN 0854045643.

[51] Cruz, C. N.; Pandis, S. N. Environmental Science & Technology 2000, 34, 4313-4319.

[52] G. Ertl, H. Knözinger, F. Schüth and J. Weitkamp, Handbook of Heterogeneous Catalysis, 8 Volumes, 2nd ed. Wiley-VCH, 2008.

[53] Y. Wang, K. Jacobi, W. Schöne and G. Ertl, "Catalytic Oxidation of Ammonia on RuO_2 (110) Surfaces: Mechanism and Selectivity," The Journal of Physical Chemistry B, vol. 109, no. 16, pp. 7883-7893, Apr. 2005.

[54] S. Shah and A. Revzin, “Patterning Cells on Optically Transparent Indium Tin Oxide Electrodes,” Journal of Visualized Experiments : JoVE, no. 7.

[55] H. Bisht, H. Eun, A. Mehrtens and M. A. Aegerter, “Comparison of spray pyrolyzed FTO, ATO and ITO coatings for flat and bent glass substrates,” Thin Solid Films, vol. 351, no. 1, pp. 109-114, Aug. 1999.

[56] X. Cui, J. Zhou, Z. Ye, H. Chen, L. Li, M. Ruan, J. Shi. Selective catalytic oxidation of ammonia to nitrogen over mesoporous CuO/RuO_2 synthesized by co-nanocasting-replication method. Journal of Catalysis 270 (2010) 310–317.

[57] J. Shi, R. Yan, Y. Zhu, X. Zhang. Determination of NH3 gas by combination of nanosized LaCoO3 converter with chemiluminescence detector. Talanta 6 (2003) 157/164.

[58] S. Yoon, S. Heo, S. Song and Y.-J. Kim. Conversion of NO to NO_2 in air by a micro electric NOx converter based on a corona discharge process. Analyst, 2010, 135, 1327–1332.

[59] J. Tamaki, M. Nagaishi, Y. Teroaoka, N. Miura, and N. Yamazoe, “Adsorption behavior of CO and interfering gases on SnO_2,” Surface Sci. 221, pp. 183–196, 1989.

7. Carbonyl compounds detection. Thermomodulation. Principle components

7.1. Introduction

7.1.1. Carbonyl compounds and their applications

Aldehydes and ketones are widely used in chemical industry. For example, acetone is used as a solvent in production of paints, medical products, as a precursor in the synthesis of methyl methacrylate, acetic anhydride, ketene and many other substances.

Formaldehyde world annual production exceeds 20 million tons. It is used for production of resin-bonded materials, plastics and artificial fibers.

Acetaldehyde world annual production is about 1 million tons. It is used in production of acetic acid, butadiene and polymers.

Chemistry of carbonyl compounds is very various. Nucleophilic attack by carbon atom of carbonyl group may lead to additive reactions (e.g., semiacetals formation) as well as to displacement reaction (e.g., oximes and hydrazones formation). Deprotonation of hydrogen atom neighboring carbonyl leads to the formation of rather stable carbanion, therefore aldehydes and ketones are quite strong C-H acids. Additive reactions may also proceed under the influence of electron-seeking reagents on carbonyl oxygen. Moreover, aldehydes possess high reductive activity.

Many carbonyl compounds, e.g., formaldehyde, and (probably) acetaldehyde are carcinogens [1].

Another danger related with the use of carbonyl compounds is their flammability risk and the explosive risk of their vapors.

7.1.2. “Ketone bodies” in human metabolism

Acetone, diacetic acid and β-hydroxybutyric acid in physiology and in medicine are called “ketone bodies”. The formation of these compounds (i.e., ketogenesis) is an important physiological process which is a part of energy metabolism.

Excessive increase of “ketone bodies” concentration is called ketosis. The most common reason of ketosis is a complication of I type diabetes mellitus. Ketosis might greatly worsen patient’s condition, especially in the case of ingress of significant content of diacetic acid and β-hydroxybutyric acid in blood. It causes decrease of blood pH lower than 7.35 (ketoacidosis) and quite often leads to lethal outcome.

Thus, patients suffering from diabetes mellitus often have to control not only glucose concentration in blood, but also “ketone bodies” concentration [2-4]. Currently, ketoacidosis diagnostics is based on chemical interaction of patient urine with test papers impregnated with sodium nitroprusside with following semiquantitative determination of ketones by colorimetric method. This diagnostic technique is neither precise nor comfortable for the patient, and in many cases this method cannot be applied, because ketosis and especially ketoacidosis may cause anuria.

At present, the analysis of exhaled air is applied for medical diagnostics more and more frequently. However, determination of “ketone bodies” with the help of such traditional means of gas analysis as mass-spectroscopy and chromatography [5] has significant disadvantages: high cost of both equipment and every individual analysis; necessity of qualified staff; high costs of time, as well as inapplicability for out-of-lab conditions. Chemical sensors based devices have obvious advantages by these parameters. They can be used out of lab, have low cost, small dimensions, work in automatic regime, and don’t need high-qualified personnel.

At present, number of patients suffering from diabetes mellitus in the world amounts to about 250 millions, and this number doubles every 12-15 years. Thus,

the development of non-invasive diagnostics method of different forms of diabetes is an important practical task.

Semiconductor metal oxide sensors were successfully used for the ketosis diagnostics [5], as well as electrochemical sensors [6, 7] and ion mobility detector [8].

7.1.3. Determination of aldehydes and ketones in air with semiconductor sensors

The sensors produced by sol-gel method are being fabricated in millions a year (by Figaro Engineering Inc., for example). Response patterns of a temperature-modulated Figaro gas sensor were transformed to multi-exponential functions which facilitated the extraction of their discriminative features for gas diagnosis [12].

In order to increase sensitivity and selectivity of the sensors, different dopants are added to metal oxide sensing materials. For example, carbon nanotubes being added to tin dioxide. The use of OH-modified multiwall carbon nanotubes with diameter 20-30 nm and length ~50 microns allowed to obtain SnO_2 -based gas sensing material, which was able to determine formaldehyde at low temperature (70 ^oC) with detection limit 1 ppm [13]. The addition of antimony to SnO_2 / nanotubes mixture increases the response to acetone in 1.5 – 2 times [14].

It is necessary to decrease power consumption in order to create portable MOX sensors based devices. Silicon technology based microsubstrates are being developed for this purpose. Tin dioxide based material with additives of NiO was used as a gas sensing element of microsubstrates. The response 0.5 relative unit was obtained at 1 ppm formaldehyde concentration and temperature 250-300 ^oC [15].

Along with tin dioxide itself, nanocomposite materials like SnO_2-MeO_x are often used. It was shown that doping tin dioxide with Cd^{2+} ions significantly increases the selectivity during formaldehyde determination. At the concentration of 200 ppm and at the sensor temperature of 600 ^oC the response amounted to 35 relative units [16, 17]. The addition of silver cations to SnO_2-TiO_2 obtained by sol-gel method led to increase of selectivity to several carbonyl compounds. At formaldehyde and acetone concentrations of 200 ppm and temperature 350 ^oC responses were 40-60 relative units [18].

Another metal oxide deposition method being used along with sol-gel technology is CVD deposition. SnO_2 thin layer may be obtained by magnetron sputtering with subsequent oxidation [5]. In this work, the dopants were deposited by magnetron sputtering over the formed tin dioxide layer. The response of these sensors to acetone at 300 ^oC was 1-2 relative units depending on the dopant nature. Tin dioxide layers formed by magnetron sputtering are widely studied [19, 20].

Along with traditional materials representing conglomerated metal oxide granules, the materials on the basis of nanostructures are being applied.

SnO_2 nanotubes were simply obtained by ultrasonic impregnation of cotton wool with $SnCl_2$ solution and subsequent annealing. At temperature 350 ^oC sensor response to 50 ppm of fomaldehyde amounted to 7.5, and the response to 50 ppm of acetone was 15 [21].

It is possible to use carbon nanotubes as a matrix for the synthesis of SnO_2 nanotubes. In this case, the characteristic size of the obtained crystallites may amount just to 5-7 nm [22]. At the working temperature 200 ^oC, the response to 100 ppm of acetone was 126 relative units [22].

Complex hierarchical structures were obtained by hydrothermal method and showed high sensing activity towards acetone and benzaldehyde [23].

The analysis of carbonyl compounds in gas phase is carried out not only in stationary but also at non-stationary temperature mode. The use of non-stationary conditions increase selectivity and sensitivity of semiconductor sensors. SnO_2 based sensors were used for acetone determination in exhalation of patients with diabetes [8]. The sensors were operated in thermomodulation mode with the period of 22 seconds and temperature change from 60 to 480 ^oC. In another work [12] temperature changed stepwise from 50 to 350 ^oC. This mode allowed determining acetone selectively at concentrations above 100 ppm.

In order to increase selectivity of analysis, multisensor systems (“electronic nose”) are often used. For the determination of acetone in exhalation of diabetics patients there were used sensors based on SnO_2, TiO_2 and WO_3 [8]. For the medical

diagnostics it was developed an “e-nose” with a preconcentrator, containing sensors based on SnO_2 with additives of gold, palladium, platinum and ruthenium. Selective determination of acetone and acetaldehyde was carried out with the help of this device [24].

The surface of semiconductor sensing layers was activated by light-emitting diodes [25]. The impact of red, yellow, green and blue radiation on SnO_2 sensors response was investigated during acetone determination with concentration 1-10 ppm. It is shown that photoinitiation increases the response in 2-100 times.

7.2. Detection of aldehydes and ketones with SnO_2 sensors

7.2.1. Chemisrty of carbonyl compounds interaction with SnO_2 sensing material

There is a wide variety of chemical transformations of carbonyl compounds adsorbed on the surface of tin dioxide. Proceeding from general concepts of aldehydes chemistry, the most probable one is their oxidation by oxygen anions with the formation of carboxylic acids:

$$R-CHO+O^{-}\rightarrow R-COOH+\bar{e}. \qquad (7.1)$$

Formaldehyde is capable of thermal decomposition [32, 33]:

$$HCHO\rightarrow H_2+CO \qquad (7.2)$$

Carboxylic acids (7.1) should be generated during oxidation of ketones as well, which usually proceeds in more stern conditions and is accompanied by break of the carbon chain. Thus, during the determination of acetone vapors with SnO_2 based sensors it would be expected the appearance of formic and acetic acids in the atmosphere. However, many other substances are also formed in the gas chamber: formaldehyde, ethylene, propylene, acetaldehyde, acrolein, and other components with higher retention time [30] (the analyses of gas mixtures from the gas chamber were made by the means of gas chromatography).

Formaldehyde formation seemingly happens as follows:

$$CH_3-CO-CH_3\longrightarrow CH_2O+CH_2=CH_2$$

Acetaldehyde formation might take place according to the same scheme:

$$2CH_3-CO-CH_3\longrightarrow 2CH_3CHO+CH_2=CH_2$$

The formation of heavy organic compounds or acroleine begins from the transformation of adsorbed aceton to enol form and following dissociation:

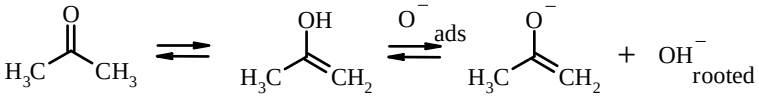

Acroleine formation is evidence of the regrouping inside of enol molecule [35]:

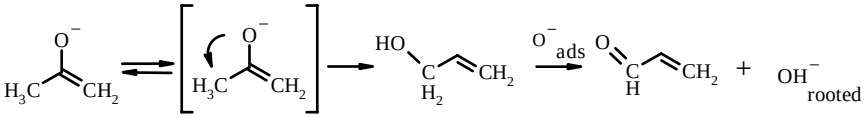

Interaction between acetone molecules may lead to aldol and croton condensation with the formation of 3-pentene-2-on:

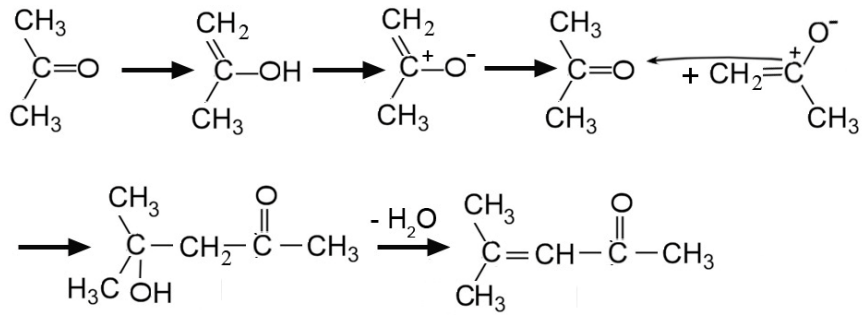

Hydroxyl group on the surface of tin dioxide may serve as a catalyst of acetone transformation to acetic acid and methane:

$$\frac{\backslash}{/}SnOH + (CH_3)_2CO \rightarrow \frac{\backslash}{/}SnO \bullet C(CH_3)_2OH \xrightarrow{H_2O} CH_4 + (CH_3COOH)_{ads} + Sn - OH$$

This reaction proceeds due to the formation of coordination complexes on the surface of tin dioxide through unshared electron pair of carbonyl oxygen with metal cation. Coordination complexes are formed because of hydrogen bonds with hydroxyl groups on the lattice surface [36].

7.2.2. Aldehydes and ketones detection in stationary temperature modes

This chapter describes the results of sensors characterization.

The sensors used for carbonyl compounds detection were based on sensing layers consisting of bulk SnO_2 and SnO_2 doped with platinum or palladium (for fabrication details, see chapter 2).

Sensor response G was defined as relative difference between electroconductivity at the testing ambient (σ_x) and at air (σ_0).

$$G = \frac{|\sigma_x - \sigma_0|}{\min(\sigma_x, \sigma_0)} = \frac{|R_x - R_0|}{\min(R_x, R_0)}$$

The sensors were operated in stationary (7.2.2) and non-stationary (7.2.3) temperature modes.

7.2.2.1. Aldehydes and ketones detection with SnO_2-based sensor

Figures 7.1 and 7.2 show the response of the sensor at different operating temperatures when measuring 100 ppm of different vapours. The degree of conversion of carbonyl compounds increases with the temperature increase [37]. However, increase of the temperature above 300-350 ^oC doesn't lead to the response increase for aldehydes determination (figure 7.1), what can be explained by the decrease of analyte adsorption. Instead, the reponse decreases for acetaldehyde and benzaldehyde, while for octanal and formaldehyde, the response reaches maximium at 300 ^oC.

Ketones are being oxidized in more stern conditions. It could be the reason of the response increase at temperature increase from 300 to 400 ^oC (figure 7.2).

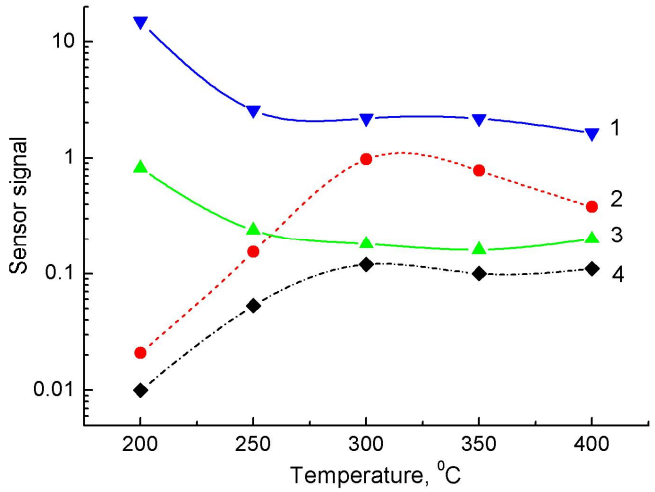

Figure 7.1. Temperature dependence of SnO_2 sensor response during detection 1) formaldehyde, 2) acetaldehyde, 3) benzaldehyde, 4) octanal. Analyte concentration – 100 ppm.

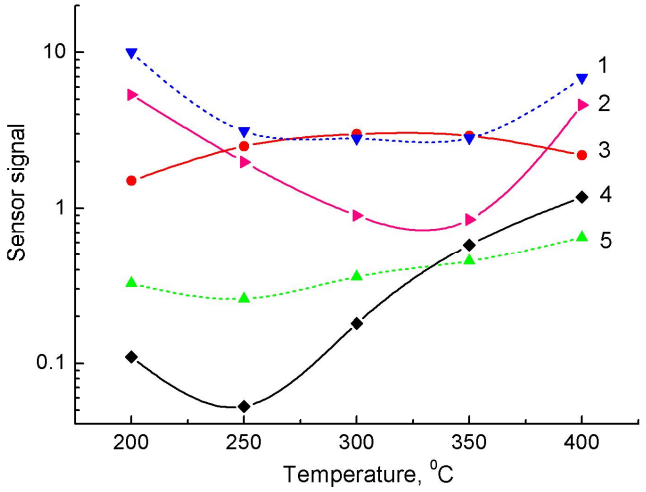

Figure 7.2. Temperature dependence of SnO_2 sensor response during detection 1) methyl-butane-2-ion, 2) acetone, 3) 5-metgylhexane-2-ione, 4) cyclopentanone, 5) cyclohexanone. Analyte concentration – 100 ppm.

Compounds 1 and 2 (figure 7.2) have higher response at low temperatures (200 °C). The reponse comes down at medium temperatures (250-350 °C) and the increases at higher temperaures (400 °C). Compund 4 shows similar behavior, but the response increses again for lower temperature (from 300 °C). Compunds 3 and 5 show weak temperature dependence. Compund 3 have maximum response at nd

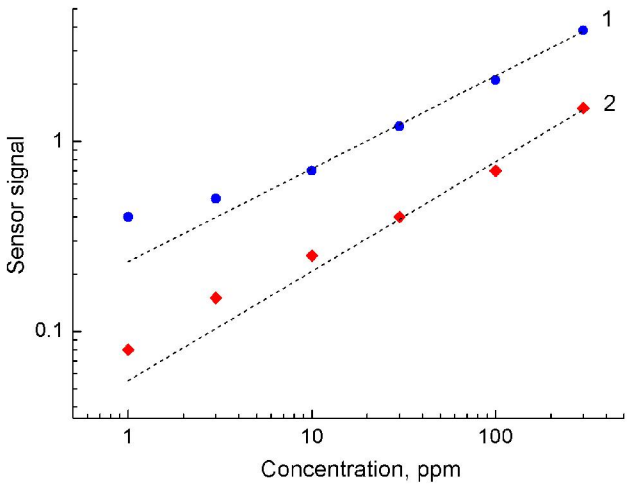

Figure 7.3. Concentration dependence of SnO_2 sensor response during detection of 1) acetaldehyde, 2) formaldehyde in air

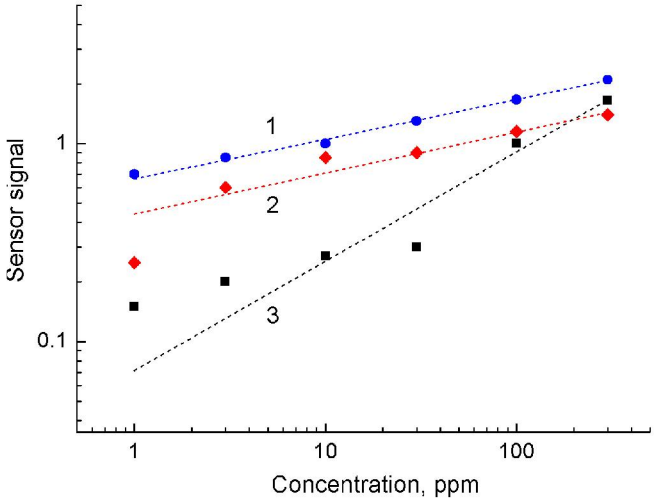

Figure 7.4. Concentration dependence of SnO_2 sensor response during detection of 1) 5-methylhexane-2-one, 2) 3-methylbutane-2-one, 3) acetone in air

300 °C, while compound 5 shows an increseng reponse for increasing operating temperature.

Response to concentration dependences (calibration curves, figures 7.3 and 7.4) are well approximated by power dependences. This can be explained by the fact that the sensor response significantly depends on adsorption value. The value of adsorption is usually described by Freundlich isotherm, which also represents a power function.

Table 1 shows coefficients *a* and *b* of calibration dependences in the form

$$G = a\varphi^b,$$

where *G* is sensor response, φ is analyte concentration (volume fraction) in air. Moreover, table 1 contains square of correlation coefficient (R^2).

]Table 7.1. Coefficients of calibration dependences during aldehydes and ketones determination with SnO_2 sensor. Temperature is 350 °C

Analyte	*a*	*b*	R^2
Formaldehyde	0.03	0.63	0.96
Acetaldehyde	0.25	0.47	0.99
Benzaldehyde	0.03	0.29	0.97
Octanal	0.02	0.17	0.97
Acetone	0.12	0.46	0.99
3-Methylbutanone	0.47	0.19	0.88
5-Methylhexanon	0.63	0.20	0.95
Cyclopentanon	0.26	0.19	0.86
Cyclohexanon	0.27	0.15	0.66

The fitting with power function is worse for lower concentrations, what can be explained by saturation effect. This behavior conforms to the fact that temperature dependences are well described by Freundlich isotherm.

Hydrogen and oxygen are adsorbed on the same adsorption centers. Oxygen, being pre-adsorbed from air, occupies adsorption sites and may prevent adsorption of analite gas at low concentration of analite. In such conditions, analite species are adsorbed on free adsorption centers.

When analite concentration increases, analite species displace pre-adsorbed oxygen species, what requires additional energy and takes place only at higher concentrations of analite.

7.2.2.2. Aldehydes and ketones detection with Pd-doped sensors

Doping tin dioxide with platinum and palladium increases resistivity of semiconductor material. It is related, first of all, with electron migration from semiconductor bulk to the metal, because Fermi level of tin dioxide is higher than the one of platinum and palladium. Secondly, the addition of catalytically active metals increases oxygen chemisorption from the air, leading to its reduction and electrons migration from the bulk of semiconductor.

Addition of palladium increased sensor response to aldehydes (see figure 7.5). Temperature increase leads to significant increase of sensor response to formaldehyde and acetaldehyde (figure 7.5, left). This can be related with thermal decomposition process, which leads to the formation of hydrogen and carbon monoxide (7.2). Thus, the concentration of reducing agents in gas ambient increases as a result of decomposition reaction. Such reaction may also run with participation of acetaldehyde [30]:

$$CH_3CHO(g) + H_2O(g) \rightarrow 3H_2(g) + 2CO(g)$$

As shown in figure 7.5, temperature increase leads not to increase, but to

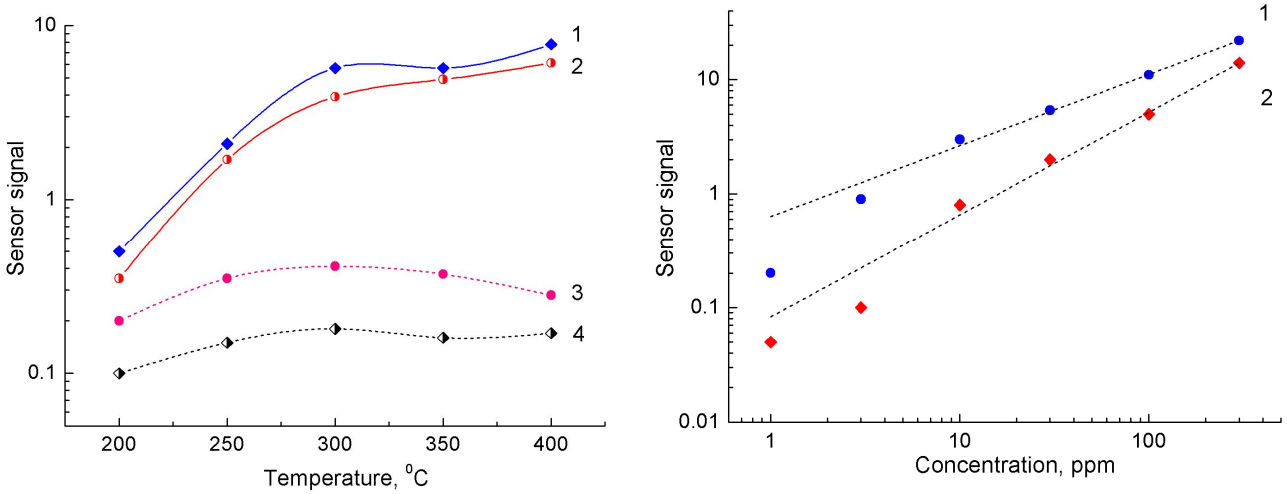

Figure 7.5. Left: temperature dependence of Pd-SnO_2 sensor during detection of 100 ppm 1) acetaldehyde, 2) formaldehyde, 3) benzaldehyde, 4) octanal in air.
Right: dependence of Pd-SnO_2 sensor response on concentration of 1) acetaldehyde, 2) formaldehyde in air at 350 °C

decrease of response to aldehydes with large enough molecular weight (benzaldehyde and octanal), what can be related with dehydration and dehydratation processes leading to carbonization of sensor surface.

As shown in figure 7.6, a monotone increase of SnO_2-Pd sensor response to ketones occurs with temperature growth. A notable abrupt increase of sensor signal takes place when temperature goes above 350°C at cyclohexanone detection. It may be caused by "ignition" of Pd catalyzer and increase of efficiency of cycloxexanone to phenol conversion (more than 80%). This process is accompanied by dehydration [32].

$$C_6H_{10}O \xrightarrow{\rangle 350^oC} C_6H_5OH + 2H_2$$

The signal to concentration dependence of Pd-SnO_2 sensor to acetone is closer to a linear one. It may be related with high catalytic activity of palladium to acetone at higher temperatures and the absence of pronounced saturation effect in this case.

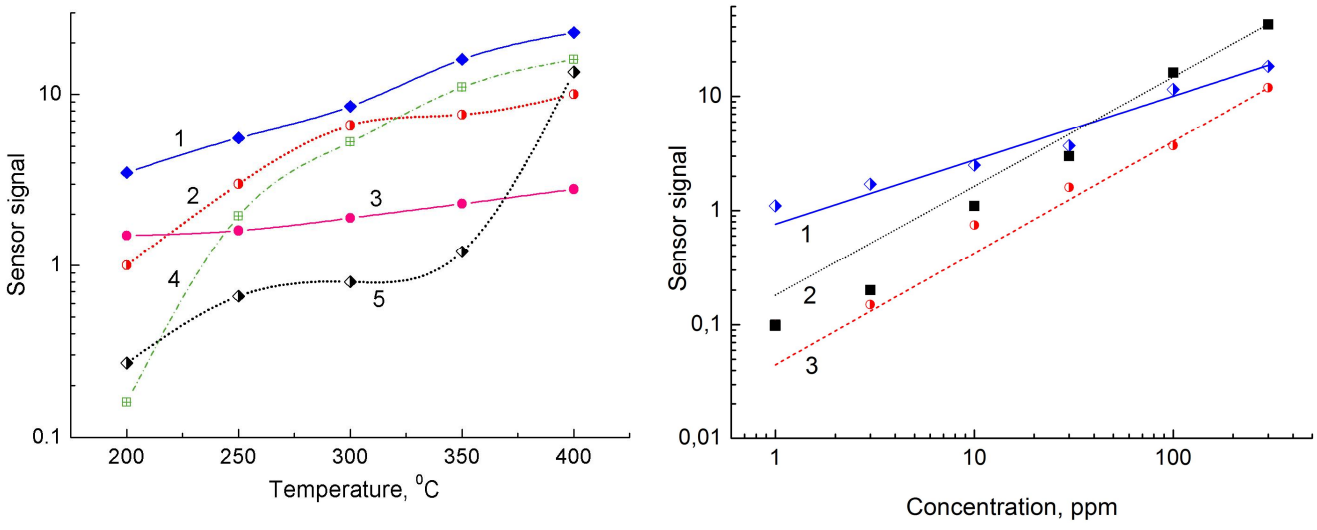

Figure 7.6. Left: temperature dependence of Pd-SnO_2 sensor during detection of 100 ppm 1) acetone, 2) 3-methylbutanone, 3) cyclopentanone, 4) 5-methylhexanone, 5) cyclohexanone in air. Right: dependence of Pd-SnO_2 sensor response on concentration of 1) 5-methylhexanone, 2) acetone, 3) cyclopentanone in air.

Table 7.2. Coefficients of calibration dependences during aldehydes and ketones determination with Pd-SnO_2 sensor. Temperature is 350 ^oC

Analyte	a	b	R^2
Formaldehyde	0.085	0.905	0.998
acetaldehyde	0.651	0.612	0.997
benzaldehyde	0.054	0.189	0.996
octanal	0.052	0.286	0.988
acetone	0.308	0.861	0.999
3-methylbutanone	0.696	0.353	0.978
5-methylhexanon	1.984	0.381	0.997
cyclopentanon	0.353	0.637	0.996
cyclohexanon	0.407	0.365	0.993

Doping SnO_2 sensing materials with palladium increases sensing layer catalityc ability and sensor signal to aldehydes.

7.2.3. Carbonyl compounds detection in nonstationary temperature conditions

7.2.3.1. Method description

The use of nonstationary temperature conditions can increase the sensitivity of analysis. Sensor impulse heating and abrupt cooling allows to combine in some points of time high catalytic activity with significant analyte adsorption, and thus to increase the response [3]. Furthermore, nonstationary conditions allow to increase the number of surface states and to increase adsorption activity.

On the other hand, nonstationary temperature conditions allow discovering individual peculiarities of the gas being detected. These peculiarities may be determined by its adsorption kinetics, kinetics of chemical interaction of analyte gas with surface oxygen, as well as desorption kinetics of analyte or the products of analyte interaction with surface oxygen. Thus, it appears the possibility not only for quantitative, but also for qualitative determination of analyte.

Temperature modes used in this work differ from each other with period duration, on-off time ratio (off-duty factor), maximal and minimal temperature

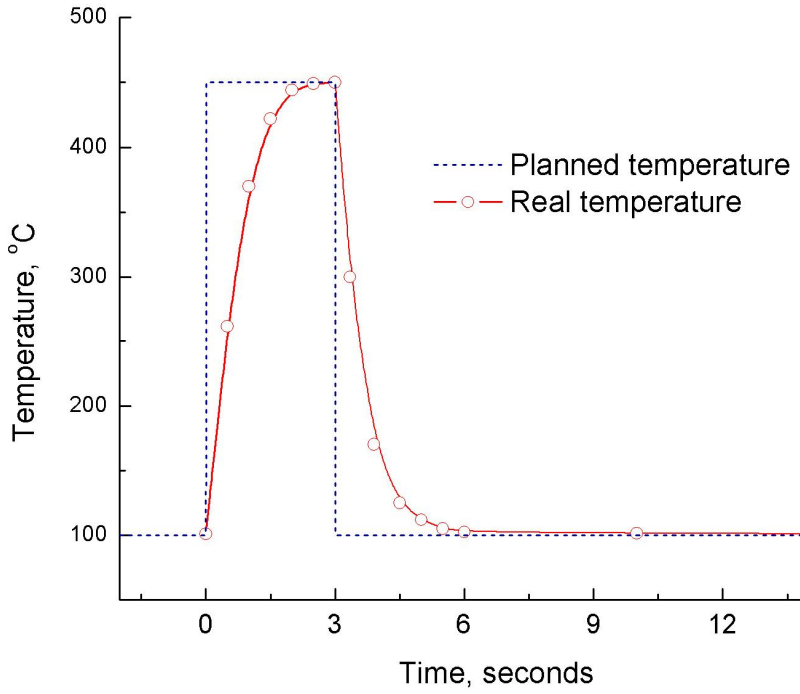

Figure 7.7. Temperature cycle of the sensor in termomodulation mode

values, and forms of temperature sweep [41]. The combination of high sensitivity and selectivity of analysis was achieved by the use of alternating heating of sensing layer up to 450 °C in 3 seconds and cooling it down to 100 °C in 12 seconds (figure 7.7).

Sensor response was determined as relative difference between sensor resistance in analyte ambient and in air on the 14th second of each cycle, i.e. at the minimal temperature of sensing layer.

Destruction with hydrogen formation is typical for formaldehyde and acetaldehyde at moderate temperatures:

$$CH_3CHO(g) + H_2O(g) \rightarrow 3H_2(g) + 2CO(g)$$

Acetaldehyde catalytic decomposition at higher temperatures may lead to methane and CO formation [30]:

$$CH_3CHO \rightarrow CH_4 + CO$$

Acetone was also subjected to thermal decomposition, but among with hydrogen and CO, carbon formation takes place, which later is oxidized to CO or CO_2 [50]:

$$CH_3COCH_3(g) \rightarrow 3H_2(g) + CO(g) + 2C(s)$$

$$C(s) + O^- \rightarrow CO(g) + \bar{e}$$

Thus, for effective work of the sensor it is necessary to set temperature modes which allow avoiding carbonization of sensing layer surface.

7.2.3.2. Application of a single semiconductor sensor working in non-stationary temperature mode for selective acetone detection

As was mentioned above, a relevant task of medical diagnostics is detection of acetone and some other “ketone bodies” in air exhaled by persons suffering from diabetes.

Analysis of exhaled air can give information about acetone and other “ketone bodies” content in organism and thereby realize express noninvasive ketosis diagnostics. However, up to now this problem is not solved due to insufficient detection limits of acetone and other “ketone bodies” with chemical sensors. Even better commercial sensors usually have detection limit about 1 – 10 ppm. For example, sensor TGS 822 made by Figaro Engineering Inc., is intended for the concentrations above 50 ppm. However, the earlier studies showed that acetone concentration in patients’ exhalation is about 0.5 – 15 ppm [2]. Thus, it is necessary to decrease detection limit of chemical sensors for effective ketosis diagnostics.

Synthesis of new materials, like metal oxide structures with developed surface and catalytical dopants, described above, allowed increasing sensitivity during acetone detection. As commented, switch to non-stationary temperature modes also leads to sensitivity increase. This approach also allows singling out individual peculiarities of detecting gas. These peculiarities may be determined by kinetics of gas adsorption, kinetics of its chemical interaction with surface oxygen, and desorption kinetics of the gas or the products of its interaction with oxygen. Thus, it appears the possibility of not only quantitative, but also qualitative acetone determination in air.

Another important task which hasn’t found an optimal solution yet, is ethanol vapors selective determination. Semiconductor sensors are widely used for the production of breath analyzers; however these devices cannot distinguish ethanol from acetone. Thus, ketosis status may be falsely taken for alcoholic inebriation by traffic police.

Combination of qualitative and quantitative determination of gases can be realized by the use of a sensor array. The use of non-stationary temperature modes gives an opportunity for selective determination of gases and vapors by a single sensor. In this case the time electroconductivity dependence of the sensor is considered as a multidimensional data array. In the present work 25 values of electroconductivity, taken in some fixed instants of time, starting from the beginning of the cycle, were used.

Intervals between two electroconductivity measurements amounted to 0.2 second (at the beginning of a cycle) and 5 seconds (at the end of the cycle). Thus, every gas system could be characterized by a point of 25-dimentional space.

From the point of view of mathematics, n-dimensional space is not fundamentally different from 2-dimentional one, but at the results publication it appears the problem of data presentation in common view of a 2-dimentional

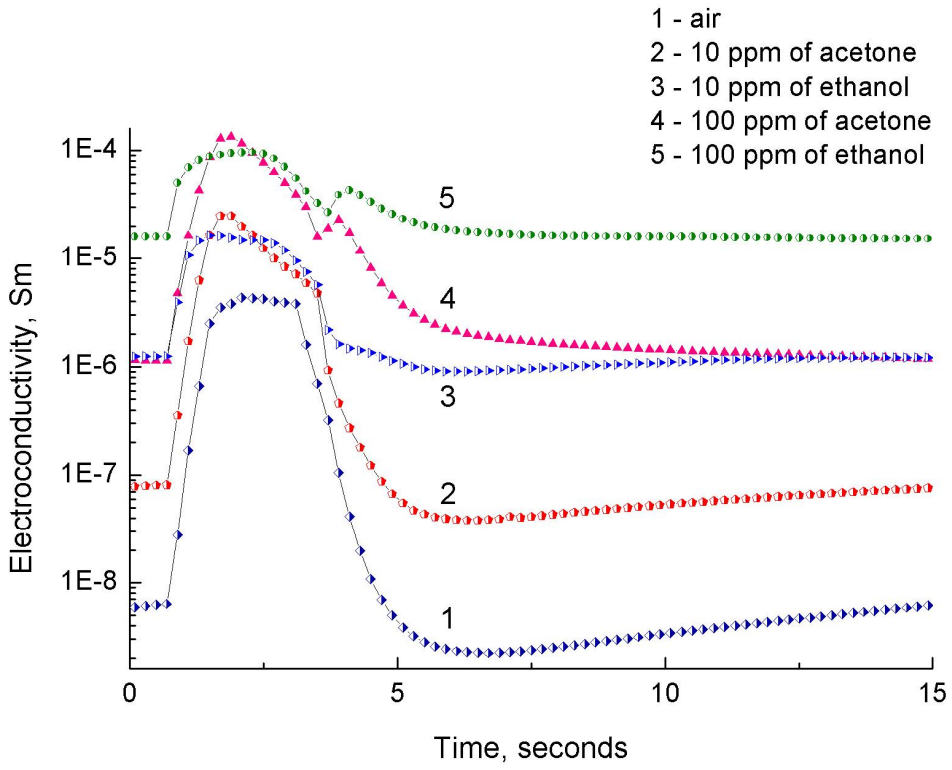

Figure 7.8. Time dependence of Pd-Pt-SnO_2 sensor electroconductivity during detection of acetone and ethanol

graph. The task of principal components analysis method, used in this work, is the

decreasing number of space dimensions for the convenience of results presentation. This is achieved by the determination of an optimal section, i.e. such a plane of n-dimensional space, where the projections of experimental points are located on the same distance from each other as in initial n-dimensional space [34].

The obtained data were processed with principal components method (figure 7.9). It is possible to single out nonoverlapping areas corresponding to ethanol and acetone of different concentrations.

Thus, it appears a principle possibility for quantitative and qualitative determination of acetone and ethanol with a single metal oxide sensor, what is important not only for ketosis diagnostics, but also for the selective detection of ethanol vapors in exhaled breath during determination of alcoholic inebriation state of drivers.

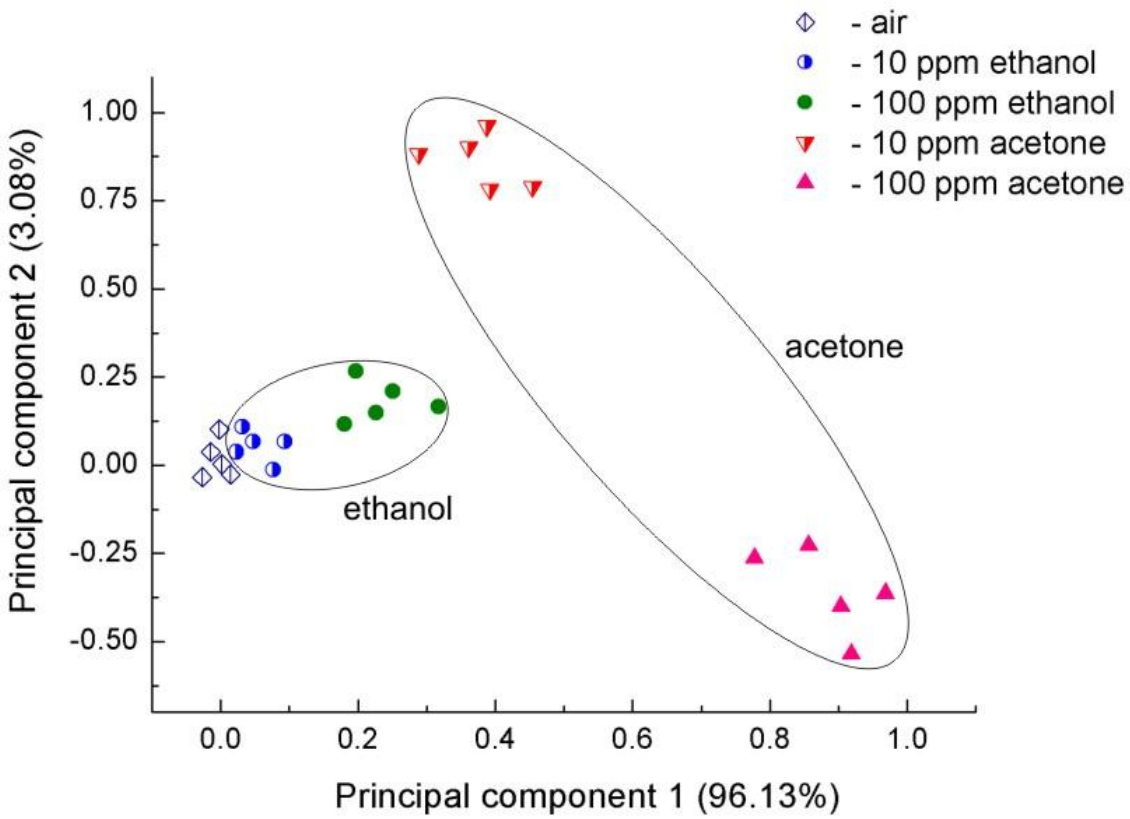

Figure 7.9. Principal components at qualitative and quantitative determination of acetone and ethanol with a single Pd-Pt-SnO_2 sensor in non-stationary temperature mode

Numerous constructions of breath analyzers are based on the use of single semiconductor sensors. A shortcoming of semiconductor sensors is quite high power consumption; therefore portable devices can include only one sensor. The present results shows that the use of impulse mode allows not only reduce power

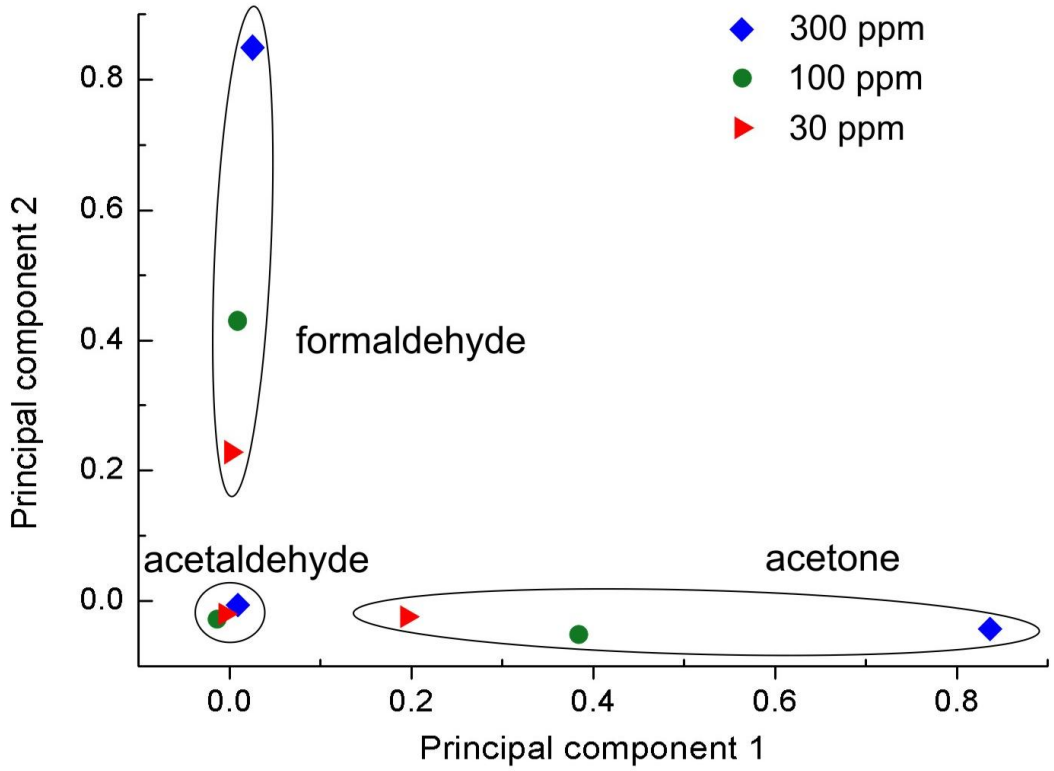

Figure 7.10. Principal components at qualitative and quantitative determination of acetone, acetaldehyde and formaldehyde with a single Pd-SnO_2 sensor in nonstationary temperature mode

consumption, but also increase sensitivity and selectivity of analysis [35].

The possibility of selective analysis with the use of a single SnO_2-Pd sensor was demonstrated with a qualitative and quantitative detection of acetone, formaldehyde and acetaldehyde. Data presented on kinetical curves were rocessed with principal components method. As shown on figure 7.10, even analytes with similar properties could be selectively determined with a single sensor.

References Chapter 7

[1] Lambert B., He S.M. DNA and chromosome damage induced by acetaldehyde in human lymphocytes in vitro. Ann N Y Acad Sci. 1988; 534:369-76

[2] Sherwin R.S., Hendler R.G., Felig P. Effect of ketone infusions on aminoacids and nitrogen metabolism in man. J. Clin. Invest. – 1975 Vol.55. P. 1382–1390.

[3] Van Itallie T.B., Yang M–U. Cardiac dysfunction in obese dieters: a potentially lethal complication of rapid massive weight loss. Amer. J. Clin. Nutr. 1984. Vol. 39. P.695–702.

[4] American Diabetes Association. From Diabetes Care, Vol. 27, Supplement 1, 2004; P. 91-93.

[5] S.V. Ryabtsev, A.V. Shaposhnik, A.N. Lukin, E.P. Domashevskaya. Application of semiconductor gas sensors for medical diagnostics. Sensors & Actuators B. – 1999. – V. 59. – P. 26-29.

[6] M. Righettoni, A. Tricoli, Sotiris E. Pratsinis. Si:WO3 Sensors for highly selective detection of acetone for easy diagnosis of diabetes by breath analysis. Anal. Chem. – 2010. - V.B 82. – P. 3581–3587.

[7] G. Neri, A. Bonavita, G. Micali, N. Donato. Design and development of a breath acetone MOS sensor for ketogenic diets control. Sensor journal. – 2010. - V.10.B.1. – P. 131-136.

[8] K.D. Benkstein, B. Raman, C.B. Montgomery, C.J. Martinez, S. Semancik. Microsensors in dynamic backgrounds: toward real-time breath monitoring. IEEE Sensor journal. – 2010. - V. 10. B.1. – P. 137-144.

[9] B.E. Landini, S.T. Bravard. Effect of exhalation variables on the current response of an enzymatic breath acetone sensing device. IEEE Sensor journal. – 2010. - V. 10. B.1. – P. 19-24.

[10] B.E. Landini, S.T. Bravard. Breath acetone concentration measured using a palm-size enzymatic sensor system. IEEE Sensor journal. – 2009. - V. 9.B.12.- P. 1802-1807.

[11] M.A. Molinaa, W. Zhaoa, S. Sankarana, M. Schivob, N.J. Kenyonb, C.E. Davisa. Design-of-experiment optimization of exhaled breath condensate analysis using a miniature differential mobility spectrometer (DMS). Analytica chimica acta. – 2008. V. 6.B.28. – P. 155–161.

[12] F. Hossein-Babaei, S.M. Hosseini-Golgoo, A. Amini. Extracting discriminative information from the Padé-Z-transformed responses of a temperature-modulated chemoresistive sensor for gas recognition. Sensors and Actuators. – 2009. – V.B.142. – P. 19–27.

[13] J. Wang, L. Liu, S.-Y. Cong, J.-Q. Qi, B.-K. Xu. An enrichment method to detect low concentration formaldehyde. Sensors and Actuators. – 2008. –V.B.134. – P. 1010–1015.

[14] J. Liu, Z. Guo, F. Meng, Y. Jia, J. Liu A Novel antimony carbon nanotube Tin oxide thin film: carbon nanotubes as growth guider and energy buffer. Application for indoor air pollutants gas sensor. Journal Physical Chemistry. – 2008. - V.B.112. – P. 6119-6125.

[15] P. Lv, Z.A. Tang, J. Yu, F.T. Zhang, G.F. Wei, Z.X. Huang, Yann Hu. Study on a micro-gas sensor with SnO2–NiO sensitive film for indoor formaldehyde detection. Sensors and Actuators. – 2008. – V.B.132. – P. 74–80.

[16] Z. Lin, G. Chen , X. Zhou, W. Zeng, H. Zhang. The gas sensitivity of nano TiO2 – SnO2 film doped with Cd(II) ion. Materials Letters. – 2009. - V.B.63. – P. 2277–2279.

[17] W. Zeng, T. Liu, Z. Wang, S. Tsukimoto, M. Saito, Y. Ikuhara. Selective Detection of Formaldehyde Gas Using a Cd-Doped TiO2-SnO2 Sensor. Sensor. – 2009. – V.B.9. – P. 9029-9038.

[18] Z. Wen, L. Tian-mo. Gas-sensing properties of SnO2 –TiO2 -based sensor for volatile organic compound gas and its sensing mechanism. Physica B: Condensed Matter, Volume 405, Issue 5, 1 March 2010, Pages 1345-1348

[19] V. V. Simakov. Gazochuvstvitelnye svoystva nanostrukturirovannyh tonkoplenochnyh sloev dioksida olova. Nanotehnika, 2010, Vol. 1, N 1, pp. 24 – 28

[20] V V Kisin V V Sysoev V A Voroshilov. *Raspoznovanie parov ammiaka i atsetona s pomoshhyu nabora odnotipnyh tonkoplenochnyh datchikov.* Pisma v ZHFT 1999, Vol. 25 (16) pp. 54 - 58

[21] S. Zhu, D. Zhang, J. Gu, J. Xu, J. Dong, J. Li. Biotemplate fabrication of SnO_2 nanotubular materials by a sonochemical method for gas sensors. J. Nanopart. Res. – 2010. – V.B. 12. – P. 1389–1400.

[22] Y. Jia, L. He, Z. Guo, F. Meng, T. Luo, M. Li, J. Liu. Preparation of Porous Tin Oxide Nanotubes Using Carbon Nanotubes as Templates and Their Gas-Sensing Propeties. J. Phys. Chem. C. – 2009. - V. 113 (22). – P. 9581-9587.

[23] Fang C. Corraloid SnO2 with hierarchical structure and their application as recoverable gas sensors for the detection of benzalehyde/acetone / Materials Chemistry and Physics. – 2010. - V. 122, Issue 1. – P. 30-34.

[24] A. Setkusa, A. Olekasa, D. Senuliene, M. Falasconib, M. Pardob, G. Sberveglieri. Analysis of the dynamic features of metal oxide sensors in response to SPME fiber gas release. Sensors and Actuators B. – 2010. - V. 146. - P. 539–544.

[25] A.M.Gulyaev, L.V. Van, O.B. Sarach, O.B. Mukhina. Light-enhanced sensitivity of SnO_{2-x} gas sensors. Semiconductors. – 2008. - V. 42, N 6. – P. 726-730.

[26] T. Kecsks; R. Nmeth; J. Rask; J. Kiss. New reaction route of HCOOH catalytic decomposition. Vacuum. 2009. -v.80. №3. - p.64-68.

[27] Walker J.F. Formaldehyde. American chemical society monograph series. - 1963. – 595c.

[28] K. G. Pierce and M. A. Barteau. Ketone coupling on reduced TiO_2 (001) surfaces: evidence of pinacol formation. J. Org. Chem. 1995. B.60, P.2405-2410.

[29] P. G. Harrison. W. Thornton. Tin oxide surfaces. Part 7. An infrared study of the chemisorption and oxidation of organic Lewis base molecules on tin (IV) oxide. J. Chem. Soc., Faraday Trans. 1976, B.12,№72, p.2484 – 2491

[30] B G Freydin A L Perkel. *O posledovatelnosti obrazovaniya nekotoryh produktov okisleniya tsiklogeksanona* Zhurnal prikladnoy himii, 1980, Vol. 53, 7, pp. 1611-1616

[31] Ryabtsev S.V., Shaposhnik A.V., Lukin A.N., Domashevskaya E.P. // Sensors and Actuators. 1999. B 59. P.26.

[32] N. Ymazoe, Y. Kurakawa, T. Seiyama. Effects of additivies on semicondactor gas sensors. Sensors and actuators B. -1983.-V.B4.-P.283-289.

[33] Matsushima S. Electronic interaction between metal additivies and tin dioxide in tin dioxide – based gas sensors / S. Matsushima, Y. Tareoka, N. Yamazoe // Japan J. Appl. Phys. – 1988.-V. 27,#3.-P.1798-1802.

[34] R. Kellner, J.-M. Mermet, M. Otto, M. Valcarcel, H. M. Widmer. Analytical Chemistry: A Modern Approach to Analytical Science. Wiley-VCH, Weinheim, 2., new revised Edition - July 2004

[35] A. V. Shaposhnik, A. A. Zvyagin, V. A. Yukish, S. V. Ryabtsev, E. P. Domashevskaya. Patent RU 2377551. Registered 27.12.2009. “Method of selective determination of acetone in air”. Priority 10.12.2007.

[36] Matsushima S. Electronic interaction between metal additivies and tin dioxide in tin dioxide – based gas sensors / S. Matsushima, Y. Tareoka, N. Yamazoe // Japan J. Appl. Phys. – 1988.-V. 27,#3.-P.1798-1802

Conclusion

Present work aimed the development of new materials and methods for gas detection.

Gases, detected by sensing devices developed in our work, are explosive (hydrogen, hydrogen sulfide), poisonous (hydrogen sulfide, ammonia) and can serve as markers for medical diagnostics (acetone).

In present work, existing methods of sol-gel synthesis were modified in order to obtain oxides with small crystallite sizes and narrow size distribution.

Optimal synthesis conditions (concentration of tin acetate, pH and temperature of precipitation) were found, what let to obtain small tin dioxide grains (1 nm) and monodisperse nanocrystals (2 nm) with high yield of the reaction. Furthermore, the conditions of sol-gel synthesis allowing simultaneous precipitation of tin and titanium oxides were developed. This approach was used for doping SnO_2 with titanium dioxide.

Obtained materials were studied with the use of SEM, TEM, FTIR, XRD methods, which demonstrated their improved characteristics, including thermal stability and dispersivity.

Among the materials used in this work to create sensing elements are single nanowires. Droplets of noble metal catalyst are usually used in VLS method of nanowire growth. In the present work, developed modification of VLS method with no use of impurities was applied. Synthesized nanowires had monocrystalline structure. Such materials have potential for creation of sensors with increased stability and optimized power consumption. Single-nanowire devices based on obtained structures were used for determination of H_2S in air. Low detection limit and good stability were achieved.

A shortcoming of semiconductor gas sensors is low selectivity. In order to increase selectivity of sensing devices, non-stationary temperature modes were used. The use of such modes allows characterization of the ambient not by only one

value of electrical resistance, but by a wide data set. Moreover, such approach enables to obtain not only quantitative, but also qualitative information about environment. Application of principal component analysis (PCA) allowed discrimination between acetone and ethanol as well as their selective, qualitative and quantitative determination by a single metal-doped SnO_2 sensor.

Another approach used for selectivity enhancement is application of a catalytic device which allows changing the composition of the ambient inside the gas chamber and thus obtaining additional information about this composition. Microreactor selectively converts a target gas into the form more suitable for the detection with a gas sensor. Selective detection of NH_3 which was converted to NO2 was achieved by a simple, low-power consuming device.

Selectivity and sensitivity of thick-layer SnO_2-based sensors to hydrogen in humid atmosphere was increased by doping tin dioxide with titania. A model conception of increased sensitivity is proposed.

Several very different approaches were shown to be able to improve greatly sensing performance of semiconductor devices without a loose of their key features.